Check for updates

ENGINEERING

All-optical sensing of dermal activity enables an AI-powered wearable ring for continuous stress monitoring

Md Farhad Hassan[1,2], Shounak Das[1,2], Dolendra Vikas Addepalli[1,2], Leikhang Xiong[1,2], Mohammad Shafiqul Islam[1,2], A. K. M. Rakib[3], Samiha Tasnim[1,2], Xiao Yu[1,2], Emily Rawson[1,2], Mohammed Arfan[1,2], Antonin Brun[4], Gale M. Lucas[5], Burçin Becerik-Gerber[4], Adam Frank[6], Yasser Khan[1,2,7]*

Copyright © 2026 The Authors, some rights reserved; exclusive licensee American Association for the Advancement of Science. No claim to original U.S. Government Works. Distributed under a Creative Commons Attribution NonCommercial License 4.0 (CC BY-NC).

Electrodermal activity (EDA), a primary stress-sensing signal in today's wearables, requires skin-electrode contact that drifts and degrades over time, limiting long-term use. Here, we present an artificial intelligence (AI)–powered ring for all-optical sensing of dermal activity (ODA), using light rather than electrodes to track sweat gland activation, thereby enhancing durability and comfort. An optimized dual-wavelength design (960 and 1250 nanometers) captures perspiration dynamics while concurrently recording photoplethysmography. The ODA ring integrates temperature and motion sensors for multimodal monitoring with on-device inference. In correlation studies, ODA and EDA signals showed 86% agreement. In classification tasks, the ODA ring achieved 92.3% binary accuracy versus 77.95% for EDA. In multiclass tasks, ODA outperforms EDA by 100 to 74.58% (short term) and 89.72 to 43.20% (long term). On-device one-dimensional convolutional neural network inference enabled 87.53% autonomous accuracy. This electrode-free modality establishes a scalable, all-optical platform for rings, watches, and patches for accurate, robust, and long-term stress monitoring.

INTRODUCTION

Stress has profound effects on mental and physical health, contributing to chronic conditions such as cardiovascular disease, depression, and anxiety (*1*). With 264 million people worldwide affected by stress-related disorders (*2*), there is a pressing need for continuous, real-time monitoring solutions. Unmanaged stress impairs cognitive function and decision-making, particularly in high-stakes fields such as athletics, military, emergency response, and aviation, where it compromises safety, efficiency, and well-being (*3*). In workplace settings, where stress directly affects mental health and productivity, proactive monitoring enables timely interventions, mitigates long-term health risks, and informs tailored management strategies (*4*). Hence, discreet, real-time monitoring tools are essential for proactively addressing stress and enhancing overall resilience (*5*). The physiological response to stress involves a complex interplay of the nervous and endocrine systems, enabling the body to adapt to environmental and emotional stimuli. Stress activates the hypothalamic-pituitary-adrenal (HPA) and sympathetic adrenal medullary (SAM) axes, triggering the release of adrenaline, noradrenaline, and cortisol (*6*). This hormonal surge induces cardiovascular changes, elevates heart rate, and disrupts metabolic regulation. Simultaneously, sympathetic activation stimulates eccrine sweat glands, leading to sweat secretion particularly on the palms, fingers, soles, and face manifesting as sympathetic sweating, which can be quantified through electrodermal activity (EDA) (*7*). In addition, stress alters sweat electrolyte composition and metabolites like glucose and lactate, offering biochemical markers for real-time stress assessment. These physiological and biochemical signatures underpin advanced sensing technologies for objective stress monitoring (*8*, *9*).

Existing stress monitoring methods fall into three main categories: self-reporting (*10*–*12*), biofluid analysis (*13*–*15*), and physiological sensing (*16*–*18*). Table S1 presents a summary of these methods. Self-reporting remains a common approach but is inherently subjective, relying heavily on individuals' perceptions and recall of stress episodes. This limits its ability to capture acute stress events or provide continuous, objective measurements (*19*). Biofluid analysis, which measures stress biomarkers such as cortisol in sweat, saliva, or blood, offers a direct approach but is invasive, labor-intensive, and impractical for continuous monitoring due to the need for frequent sampling and the low concentration of key biomarkers (*20*, *21*). In addition, sweat-based analysis often requires physical exertion to induce sweat, potentially altering stress levels and confounding results (*22*). Optical bioanalytical techniques such as surface plasmon resonance (SPR) and surface-enhanced Raman scattering (SERS) can improve sensitivity for biochemical marker detection but rely on engineered plasmonic substrates and dedicated optical or spectral readout (*23*, *24*). These requirements limit their straightforward integration into compact wearable platforms for continuous real-time monitoring. In contrast, physiological sensing presents a noninvasive alternative, particularly with multimodal approaches integrating EDA, photoplethysmography (PPG), and electrocardiography (ECG) showing promise in mapping stress responses (*25*–*28*). Among these, EDA is a widely recognized physiological marker for stress, directly reflecting sympathetic nervous system activity through changes in skin conductivity due to eccrine sweat gland activity (*29*, *30*).

[1]Ming Hsieh Department of Electrical and Computer Engineering, University of Southern California, Los Angeles, CA 90089, USA. [2]The Institute for Technology and Medical Systems (ITEMS), Keck School of Medicine, University of Southern California, Los Angeles, CA 90033, USA. [3]Department of Electrical & Computer Engineering, University of Maryland, College Park, MD 20742, USA. [4]Sonny Astani Department of Civil and Environmental Engineering, University of Southern California, Los Angeles, CA 90089, USA. [5]Institute for Creative Technologies, University of Southern California, Los Angeles, CA 90094, USA. [6]Department of Psychiatry and Behavioral Sciences, Keck School of Medicine, University of Southern California, Los Angeles, CA 90033, USA. [7]Alfred E. Mann Department of Biomedical Engineering, University of Southern California, Los Angeles, CA 90089, USA.
*Corresponding author. Email: yasser.khan@usc.edu

Downloaded from https://www.science.org on November 13, 2026

EDA can be measured via exosomatic methods, which apply external electrical stimulation, or endosomatic methods, which passively measure natural skin potential (*31*). Although exosomatic techniques are widely used, they often rely on dc, which causes electrode polarization and degrades signal quality over time. ac methods mitigate polarization but introduce increased complexity and sampling limitations (*32*, *33*). Commercial EDA systems use electrodes to apply a small current to the skin. Although dry electrode and ac-based systems may reduce some long-term interface limitations, gel-based EDA systems can experience drying during extended wear, causing impedance variation and signal drift (*34*). In addition, motion artifacts and skin irritation remain persistent challenges, necessitating frequent recalibration and limiting their practicality for long-term use. Beyond these technical limitations, existing physiological monitoring wearables are often large and highly visible, unintentionally drawing attention to an individual, potentially influencing stress levels, and discouraging widespread adoption due to stigma concerns. These challenges underscore the need for a next-generation stress-monitoring solution that is noninvasive, discreet, and ergonomically designed for continuous, long-term use.

In this work, we introduce the optical sensing of dermal activity (ODA) ring sensor, a noninvasive, contactless wearable designed for continuous stress monitoring by capturing eccrine sweat gland responses triggered by physiological stressors (movie S1). As shown in Fig. 1A, the ODA ring uses optical sensing to measure sweat-induced skin absorption, eliminating the need for direct skin contact. It integrates 960-nm stress-sensing and 1250-nm baseline-sensing light-emitting diodes (LEDs) with dual photodiodes to compute differential light reflectance, forming the ODA response. Beyond sweat sensing, its optical architecture inherently enables PPG, allowing concurrent extraction of cardiovascular metrics including pulse amplitude (PA), heart rate (HR), and their variabilities (PAV and HRV). This dual-modality enhances physiological assessment without requiring multiple sensors. By contrast, conventional gel-based EDA sensors rely on continuous skin-electrode contact, which can degrade over time due to contact instability and gel drying, resulting in baseline drift and signal degradation, while providing no intrinsic PPG information. By removing gel-based electrodes, the ODA sensor enables stable, long-term, contactless sensing, offering a robust and scalable alternative to traditional EDA sensors for extended monitoring (Fig. 1B). The device also integrates a temperature sensor and accelerometer for multimodal tracking, improving stress classification by accounting for motion and thermoregulatory responses. Figure 1C highlights its compact, ergonomic design, integrating LEDs, photodiodes, a microcontroller unit (MCU), power management unit (PMU), and analog front end (AFE) on a flexible four-layer printed circuit board (PCB). A system-level block diagram (Fig. 1D) details its onboard architecture, including regulated power delivery and sensor control via I2C and SPI interfaces. Figure 1E illustrates the modular assembly, final device, and worn configuration. To enable intelligent decision-making under strict resource constraints, multimodal sensor data are first used offline to identify an optimal neural network architecture that balances classification accuracy and model size, after which the trained lightweight convolutional neural network (CNN)–fully connected neural network (FCNN) model is deployed directly on the ring MCU for real-time inference (Fig. 1F). In operation, the ODA ring performs edge computation locally, transmitting only the inferred mental state to a smartphone application via Bluetooth Low Energy (BLE), thereby reducing communication energy, minimizing latency, and enhancing privacy by avoiding raw data transmission to external servers (Fig. 1G). Comparative analysis (table S2) highlights its superiority over other physiological stress sensing approaches in terms of continuous monitoring, multimodal capability, edge computing, and accuracy. Direct benchmarking against the commercial gel-based EDA sensor used in this study (table S3) showed greater long-term stability and higher classification accuracy for the multimodal ODA ring model under the evaluated conditions, with accuracies of 92.30% versus 77.95% in the short term and 79.55% versus 57.35% after 12 hours. The integration of temperature and accelerometer data further reduces misclassification from motion artifacts and thermal sweating, substantially improving four-class classification accuracy (stress, relax, motion, and thermal sweating) in both short-term (100% versus 74.58%) and long-term (89.72% versus 43.2%) scenarios. By uniting optical innovation, multimodal sensing, and edge artificial intelligence (AI) in a compact ring form, the ODA sensor provides a promising approach for unobtrusive, continuous stress monitoring.

RESULTS AND DISCUSSION

Analytical modeling of ODA

The interaction of light with biological tissue is fundamentally dictated by absorption and scattering mechanisms, leading to an exponential attenuation of light intensity as it propagates through the medium. In a heterogeneous structure such as the human finger, multiple biological components—including tissue, hemoglobin, oxyhemoglobin, and interstitial body fluids—act as absorbers, collectively influencing the intensity of the reflected light. This interaction follows the principles described by the modified Beer-Lambert law, which accounts for the cumulative attenuation effects induced by multiple absorbers within the optical path (*35*)

$$I_\lambda^t = I_0 \exp\left[-\sum_{i=1}^{j} \varepsilon_{\lambda i} C_i l_{\lambda i} - G_\lambda\right] \quad (1)$$

where I_λ^t represents the detected light intensity, I_0 is the incident intensity, $\varepsilon_{\lambda i}$, C_i, and $l_{\lambda i}$ denote the extinction coefficient, concentration, and effective optical pathlength of the ith absorber, respectively, and G_λ accounts for scattering-induced attenuation.

To specifically model the optical response associated with sympathetic sweat gland activation, the equation is simplified by separating the stress-responsive contribution from the surrounding tissue attenuation

$$I_\lambda^t(t) = I_\lambda^0 \exp\left[-K_\lambda(t) - \mu_\lambda l_{\lambda,SS} C_{SS}(t)\right] \quad (2)$$

where $K_\lambda(t)$ groups the wavelength-dependent contributions from melanin, hemoglobin, baseline tissue water, interstitial fluids, scattering, and other background tissue constituents. $C_{SS}(t)$ represents the effective stress-responsive sweat gland–associated tissue-water contribution, whereas μ_λ and $l_{\lambda,SS}$ are its wavelength-dependent absorption coefficient and effective optical pathlength, respectively.

The ODA sensor uses a dual-wavelength system: One wavelength, λ_1, is used for sensing dermal changes, whereas the second wavelength, λ_2, serves as a reference. Their detected intensities are denoted as $I_{sense}(t) = I_{\lambda_1}^t(t)$ and $I_{base}(t) = I_{\lambda_2}^t(t)$, respectively.

Because the initial separation between these signals depends on wearer-specific tissue optical properties and the sensor-skin configuration, a resting interval is used to determine the initial

Downloaded from https://www.science.org on November 13, 2026

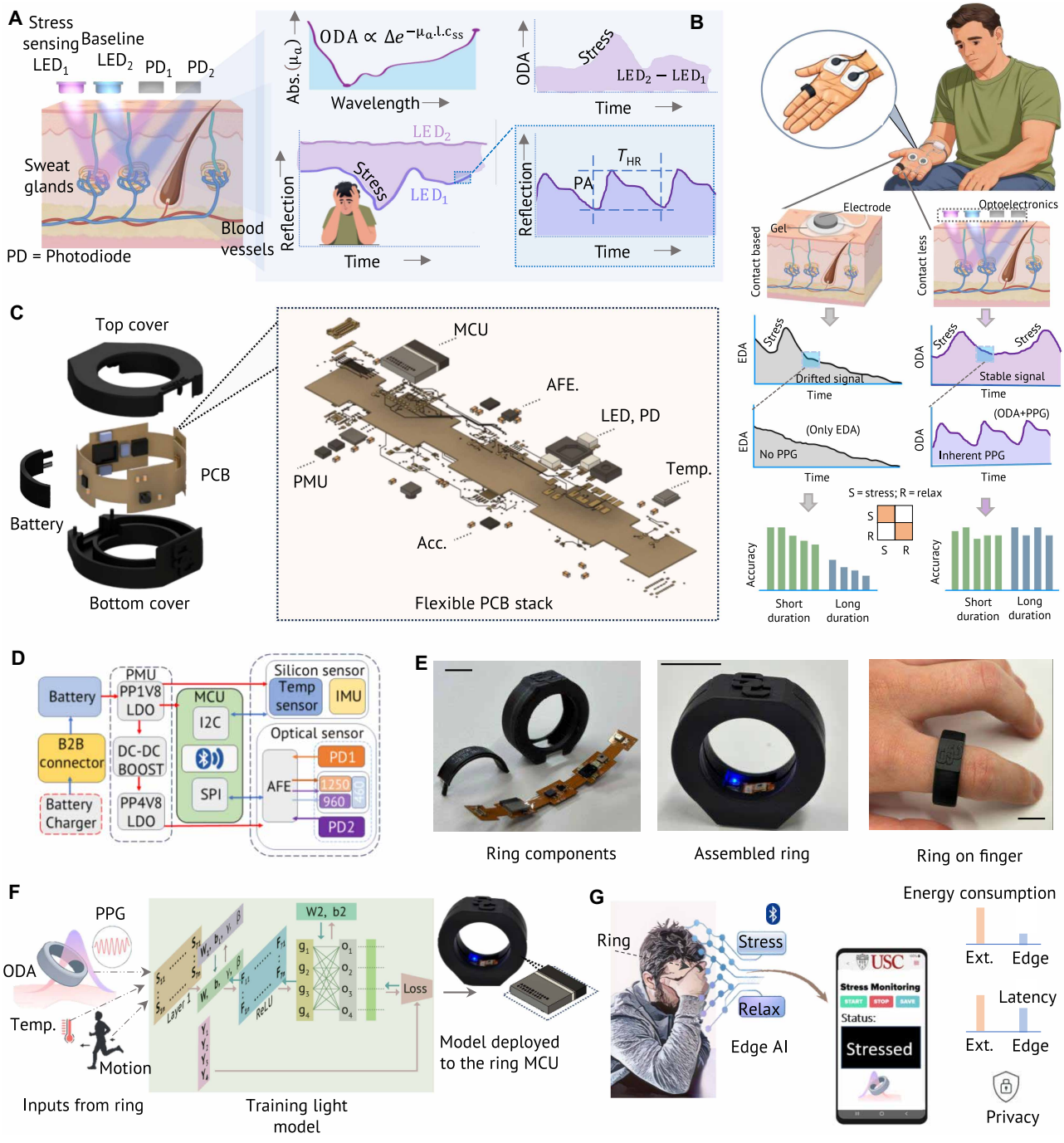


Fig. 1. Overview of the edge AI–powered ODA ring for stress monitoring. (**A**) The ODA ring exploits wavelength-dependent sweat absorption using stress-sensitive (LED_1) and baseline-aware (LED_2) LEDs, with differential reflectance forming the ODA signal. Reflected light also contains PPG information. (**B**) EDA requires continuous skin-electrode contact, often with conductive gel, leading to signal degradation and baseline drift over time and offering no intrinsic PPG. In contrast, ODA uses contactless optoelectronic reflectance, enabling stable long-term sensing with inherent PPG and improved accuracy. (**C**) Component breakdown showing the top and bottom covers, arc-shaped battery, and a flexible four-layer PCB integrating the MCU, PMU, AFE, LEDs, photodiodes (PDs), temperature sensor, and accelerometer. (**D**) System block diagram illustrating the power regulation and sensor communication via I2C and SPI, with the AFE controlling LED-PD sequencing. (**E**) Photographs of components, assembled ring, and on-body wear, highlighting the compact, ergonomic form factor (scale bars, 1 cm). (**F**) Edge AI pipeline: Sensor data are used offline to select an accuracy, model size, and optimal network and then deployed on the ring MCU for real-time inference. (**G**) On-device edge computation processes data locally and transmits only inferred mental states via BLE, reducing energy, latency, and external data exposure.

Downloaded from https://www.science.org on November 13, 2026

absolute separation, Δ_0. The baseline-corrected ODA response is then defined as

$$\mathrm{ODA}(t) = |\,\Delta_0 - |\,I_{\mathrm{base}}(t) - I_{\mathrm{sense}}(t)\,|\,| \quad (3)$$

This formulation establishes the resting response near zero and quantifies the magnitude of subsequent changes in the dual-wavelength separation. The ODA sensitivity for distinguishing stress from relaxation is defined as

$$\begin{aligned}\mathrm{ODA}_{\mathrm{sensitivity}} &= \mathrm{ODA}^{\mathrm{stress}} - \mathrm{ODA}^{\mathrm{relax}} \\ &= |\,I_{\lambda_2}^{\mathrm{relax}} - I_{\lambda_1}^{\mathrm{relax}}\,| - |\,I_{\lambda_2}^{\mathrm{stress}} - I_{\lambda_1}^{\mathrm{stress}}\,|\end{aligned} \quad (4)$$

The complete expressions for $K_\lambda(t)$, the wearer-specific baseline calculation, and the relaxed and stressed optical responses are provided in the Supplementary Materials.

This model suggests that appropriate wavelength selection and wearer-specific baseline referencing enhance ODA sensitivity and consistency for optical monitoring of dermal activity.

Simulated optimization of ODA sensing

To validate the analytical model and evaluate the feasibility of optical sensing, Monte Carlo simulations were conducted to model light propagation through a multilayer tissue structure (Fig. 2A and fig. S1). This simulation leveraged the photon "hop-drop-spin-check" approach, a widely used algorithm for simulating light transport in biological tissues. The tissue model was designed to replicate the optical complexities of human skin, incorporating layers of the epidermis (60 μm), dermis (840 μm), and a central blood vessel (100 μm) within the dermis. The source and detector were positioned in a reflective configuration, with the detector placed at $x > 50$ μm from the source.

Key optical properties, including absorption coefficient for water and blood, were sourced from the literature, whereas reduced scattering coefficient was derived using Rayleigh and Mie scattering models (*36*–*39*). Photon trajectories were simulated stochastically to capture absorption and scattering events, with reflectance quantified as the detected-to-emitted photon ratio, providing insight into light-tissue interactions. The inset of Fig. 2A illustrates energy deposition from a 960-nm light source within the modeled tissue structure. Further details of the simulation process are provided in the Supplementary Materials.

According to Eq. 4, the emitted light intensity directly influences the ODA response. To validate this, incident light intensity at 660 and 960 nm were systematically varied for tissue models with 5 and 60% water concentrations. Figure 2B demonstrates that for both wavelengths, normalized reflectance exhibits a linear increase with emitted light intensity, confirming a direct correlation between emitted light and the reflected signal. Furthermore, Fig. 2C illustrates the difference in reflectance between 5 and 60% water concentrations at 660 and 960 nm, revealing that, as intensity increases, the disparity in reflected signals becomes more pronounced, reinforcing the sensitivity of the ODA ring sensor. In addition, fig. S2 provides insights into energy deposition dynamics, showing how light absorption varies with intensity for different water concentrations. Expanding the reflectance analysis across the 460- to 1450-nm spectrum at 60% water concentration (fig. S3), the results align with theoretical predictions, demonstrating a progressive decline in reflectance at longer wavelengths due to increased absorption coefficients. To further refine ODA sensor performance, simulations were conducted across a broad water concentration range (5 to 90%), with particular emphasis on the physiologically relevant 60 to 80% range. Figure 2D presents the simulated reflectance intensity for different water concentrations, capturing the relationship between water concentration and optical response. Notably, Fig. 2E underscores the sensitivity of 960 nm within the 60 to 80% water concentration range, establishing it as an optimal wavelength for ODA sensing. Conversely, the minimal reflectance variation at 1250 and 1450 nm validates their suitability as baseline correction references.

Experimental optimization of ODA sensing

The analytical model was further validated experimentally using the setup illustrated in Fig. 2F. An artificial sweat solution (absorption spectrum in fig. S4) was introduced into an absorbing medium via a controlled pump to simulate varying water concentrations. Reflected light from LEDs at six different wavelengths was captured using two photodiodes sensitive to the visible (VIS) and near-infrared (NIR) ranges. The inset in Fig. 2F shows the circuit block diagram used in this experiment, with timing sequences and applied voltages detailed in figs. S5 and S6.

In the first set of experiments, the intensity of incident light for 660- and 960-nm wavelengths was increased by adjusting the supply current to the LEDs at water concentrations of 5 and 60%. The resulting reflectance response, presented in Fig. 2 (G and H), exhibited a linear relationship consistent with both the analytical and simulated predictions. Reflectance measurements were then conducted for LEDs at wavelengths of 460, 570, 660, 960, 1250, and 1450 nm, using a constant water concentration of 60% and a fixed LED current of 20 mA (fig. S7), further corroborating the model's validity. In the final experiment, reflectance from all LEDs was measured across water concentrations ranging from 5 to 90% (Fig. 2I). Consistent with simulation results, the 960-nm wavelength demonstrated the highest sensitivity to changes in water concentration within the physiological range of 60 to 80%, whereas 1250 and 1450 nm exhibited minimal sensitivity. Given the superior signal quality of the 1250-nm wavelength over 1450 nm at equivalent supply currents, the final sensor design used 960 nm for ODA sensing and 1250 nm for baseline correction.

Physiological and anatomical effects on ODA

Monte Carlo simulations further evaluated the ODA response across light, brown, and dark skin pigmentation, blood oxygen saturation levels of 90 to 100%, and epidermal thicknesses of 40 to 80 μm. Although these variations shifted the absolute reflectance and initial dual-wavelength baseline, the relative optical response to the same change in tissue water content remained comparable across the modeled conditions (figs. S8 to S10).

The corresponding time-series responses in Fig. 2 (K to M) further demonstrate that wearer-specific baseline correction aligns the initial ODA signals near a common baseline while preserving the event-associated response. These results support consistent ODA response across the evaluated pigmentation, oxygen saturation, and epidermal thickness ranges.

Using the optimized LED wavelengths, the ODA ring sensor was developed (fig. S11A), consisting of a flexible four-layer PCB. The PCB integrates a 460-nm status LED, a 960-nm LED, a 1250-nm LED for sensing, photodiodes for ODA measurements, and sensors for temperature and motion, enabling multimodal physiological monitoring. A system-level block diagram (fig. S11B) illustrates the PMU, comprising a lithium-polymer (LiPo) arc battery, low dropout (LDO)

Downloaded from https://www.science.org on November 13, 2026

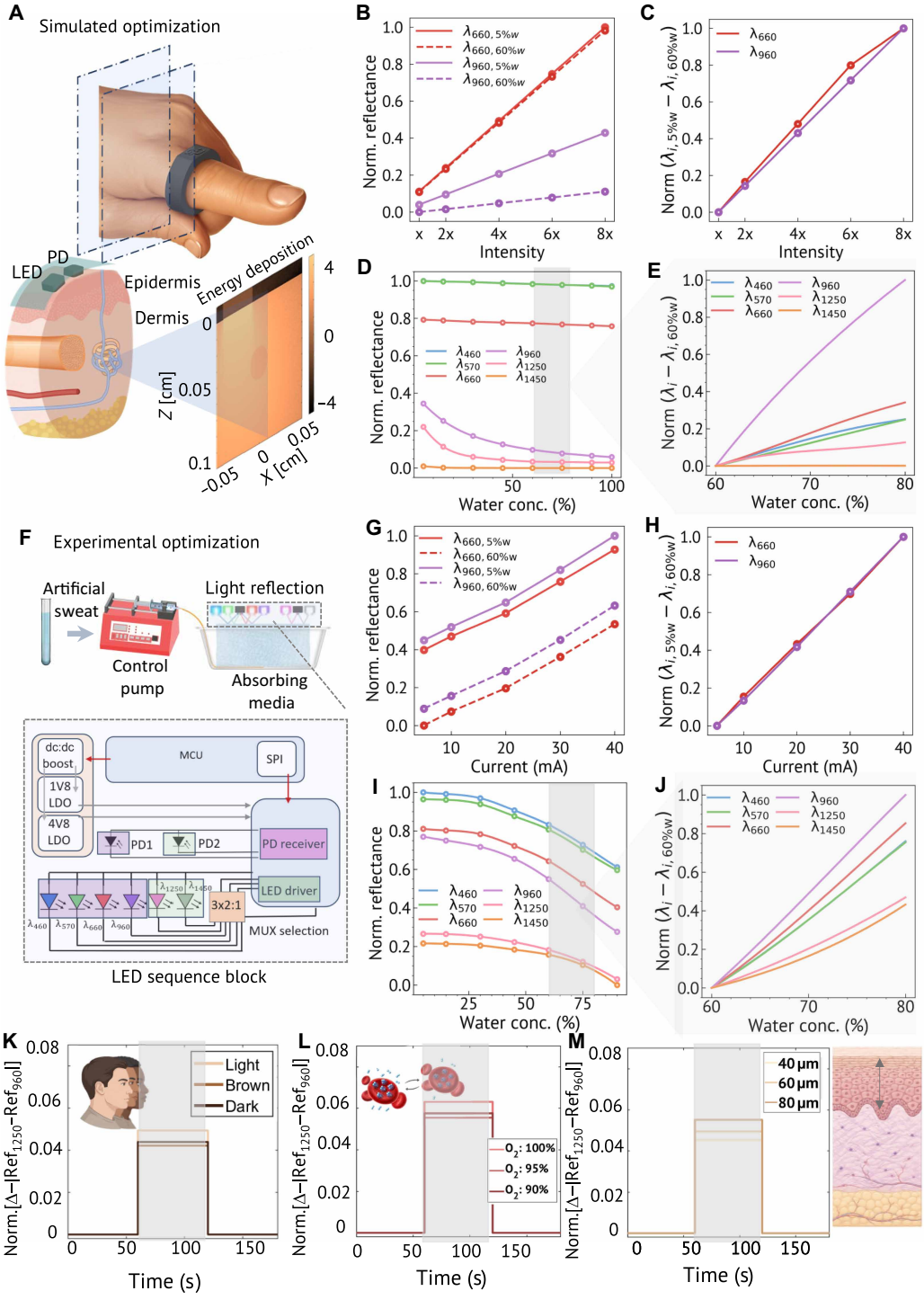


Fig. 2. Simulation and experimental optimization of ODA sensor design. (**A**) Monte Carlo simulation of light propagation in a layered finger cross section, showing the energy deposition of 960-nm light at 60% skin water concentration. (**B**) Normalized reflectance versus incident light intensity at 660 and 960 nm for 5 and 60% water concentrations, demonstrating a linear increase in reflectance. (**C**) Difference in reflected signal between 5 and 60% water concentrations, increasing with intensity for both wavelengths. (**D**) Reflectance versus water concentration simulated across six wavelengths. (**E**) Relative reflectance change between 60 and 80% water, emphasizing 960-nm responsiveness and 1250-nm stability. (**F**) Experimental setup for sensor validation using artificial sweat with a multiplexed LED-photodiode circuit. (**G**) Normalized reflectance versus LED current, confirming linearity at 660 and 960 nm for 5 and 60% artificial sweat concentrations. (**H**) Difference in reflected LED signal between 5 and 60% artificial sweat concentrations, increasing with intensity for both wavelengths. (**I**) Normalized reflectance versus artificial sweat concentration across the six wavelengths. (**J**) Relative reflectance change across water concentrations, validating 960 nm for sensing and 1250 nm for baseline correction. (**K**) Baseline-corrected ODA responses across light, brown, and dark skin pigmentation. (**L**) Baseline-corrected ODA responses at SpO_2 levels of 100, 95, and 90%. (**M**) Baseline-corrected ODA responses for epidermal thicknesses of 40, 60, and 80 µm.

Downloaded from https://www.science.org on November 13, 2026

regulators, and a dc-dc boost converter, ensuring stable voltage supply. The optical sensor module is controlled by an nRF52832 microcontroller via I2C, with the MAX86140 AFE managing sequential activation of the LEDs and photodiodes, whereas the HS3003 and BMI270 are used for temperature and motion sensing, respectively. The sensor operates in two modes: In Mode-1, raw sensor data are transmitted for external processing, whereas in Mode-2, leveraging edge computing, a pretrained machine learning (ML) model processes the data onboard and transmits only the classification result.

Stress response of the ODA ring sensor

To assess the sensor's ability in detecting stress responses, a controlled experiment was conducted (Fig. 3A), where participants wore the ODA ring in Mode-1 alongside a commercial EDA sensor. The protocol consisted of three 90-s phases: initial relaxation, stress induction through ice-cold water immersion, and a subsequent recovery phase. The ice-water immersion triggered activation of the sympathetic nervous system, resulting in an increased eccrine sweat gland response (*3*). Figure 3B illustrates the concurrent use of ODA and EDA sensors. Although the ODA ring offers a fully noninvasive, contactless optical approach, EDA sensing relies on direct skin contact through electrodes. To ensure adequate skin-electrode coupling and signal quality, conductive gel is required. However, as shown in the figure, this gel dries out over extended use, leading to signal degradation and reduced long-term reliability.

Figure 3C illustrates the reflected signals from the 960- and 1250-nm LEDs during the protocol. The 960-nm signal exhibited a noticeable decline during the stress phase due to increased sweat absorption, whereas the 1250-nm signal remained largely unchanged, serving as a stable baseline. The differential response between the two wavelengths (Fig. 3D) effectively captures the stress transition. The optical signal also contained clear PPG pulsations, enabling extraction of PA, PAV, HR, and HRV (fig. S12). Concurrent EDA processing and comparison with ODA are presented in fig. S13. Across four participants, ODA and EDA showed similar temporal responses during relaxation, stress, and recovery, with correlations ranging from 72 to 94% and an average of ~86% (fig. S14). The ODA response was further evaluated in participants with light, brown, and dark skin pigmentation using concurrent ODA, EDA, and salivary biomarker measurements (Fig. 3E and fig. S15). Participant matched ODA and EDA correlations were $r = 0.851$, $r = 0.933$, and $r = 0.858$, respectively. Salivary α-amylase increased immediately following the cold pressor test, whereas cortisol increased at the later sampling point. These results support the simulations in the "Physiological and Anatomical Effects on ODA" section, showing that wearer-specific baseline correction preserves the relative ODA response across pigmentation levels despite differences in the initial optical baseline.

Cardiovascular features obtained from the ring PPG signal were compared with simultaneously recorded ECG measurements. ECG- and PPG-derived heart rate showed correlations of $r = 0.950$, $r = 0.951$, and $r = 0.929$ across three participants (Fig. 3F), whereas their SDNN values showed correlations of $r = 0.820$, $r = 0.958$, and $r = 0.921$ (Fig. 3G and fig. S16). Thus, the optical channel provides cardiovascular information that closely follows ECG without requiring an additional electrode-based sensing system. Environmental stability was evaluated under changes in ambient illumination, room temperature, and relative humidity. Ambient light cancellation suppressed illumination interference, whereas the ODA response remained stable as temperature increased from ~28° to 38°C and relative humidity increased from ~50 to 80% (Fig. 3H and fig. S17). Comparable ODA responses were also maintained after the flexible PCBs were assembled in four ring sizes for 14 days and following repeated 6 hours daily wear (fig. S18). Last, stable positioning, finger flexion, wrist rotation, and typing were evaluated to examine motion related artifacts (Fig. 3I and fig. S19). Wrist rotation produced the greatest accelerometer motion, whereas finger flexion and typing generated larger ODA artifacts because of greater relative movement between the ring and skin. A threshold-based quadrant analysis identified stable and artifact affected windows, whereas an accelerometer-based model classified stable and motion conditions with 97.22% accuracy.

Together, these experiments validate ODA against EDA, salivary biomarkers, and ECG-derived metrics while demonstrating stable operation across pigmentation, environmental variation, mechanical stress, daily wear, and common hand movements.

Short-period stress classification

Building on the strong correlation between ODA and EDA signals demonstrated in the previous section, the classification performance of the ODA ring sensor was evaluated for its ability to identify distinct physiological states. Specifically, the sensor's capacity to distinguish between stress and relaxation events and its ability to differentiate stress responses from anomalies caused by motion or thermal sweating were tested. These results were benchmarked against the commercial EDA sensor to validate the ODA ring sensor's effectiveness. A controlled protocol involving six participants included alternating 90-s relaxation and stress phases (induced by cold-water immersion), followed by 180-s walking and stationary biking sessions to simulate motion artifacts and thermal sweating. Data from the ODA ring sensor and a commercial EDA sensor were recorded continuously. Figure 4A illustrates the captured ODA and EDA signals, along with derived physiological parameters such as PA, PAV, HR, HRV, body temperature, and motion data. The collected time-series data underwent normalization, segmented into overlapping 10-s windows with a 5-s stride, enhancing temporal resolution and mitigating noise. Derivative features, including average, minimum, maximum, and SD, were extracted, and forward feature selection was applied to optimize dimensionality. The preprocessed dataset was input into an FCNN implemented in PyTorch, featuring three hidden layers and a softmax output, as shown in Fig. 4B. This architecture facilitated robust classification into four categories: stressed, relaxed, motion, and thermal sweating. Two classification scenarios were considered: binary classification and four-class classification. The ODA signal used for classification was filtered to suppress the pulsatile PPG component. PA, PAV, HR, and HRV were extracted separately from the raw optical signal and included only in models containing derived physiological features. This separation allowed the independent contribution of ODA to be evaluated relative to the PPG-derived features. Five models were systematically compared: Model 1 used EDA data; Model 2 relied on ODA data; Model 3 used only the derived physiological features PA, PAV, HR, and HRV; Model 4 combined ODA with the derived features; and Model 5 additionally integrated body temperature and accelerometer data for multimodal analysis. In binary classification (Fig. 4C, fig. S22, and table S4), Models 1 and 2 achieved comparable accuracies of 77.95 and 79.45%, respectively. Model 3, using only the derived physiological features, achieved 63.89% accuracy. Combining ODA with these features increased the accuracy to 88.80% for Model 4, although

Downloaded from https://www.science.org on November 13, 2026

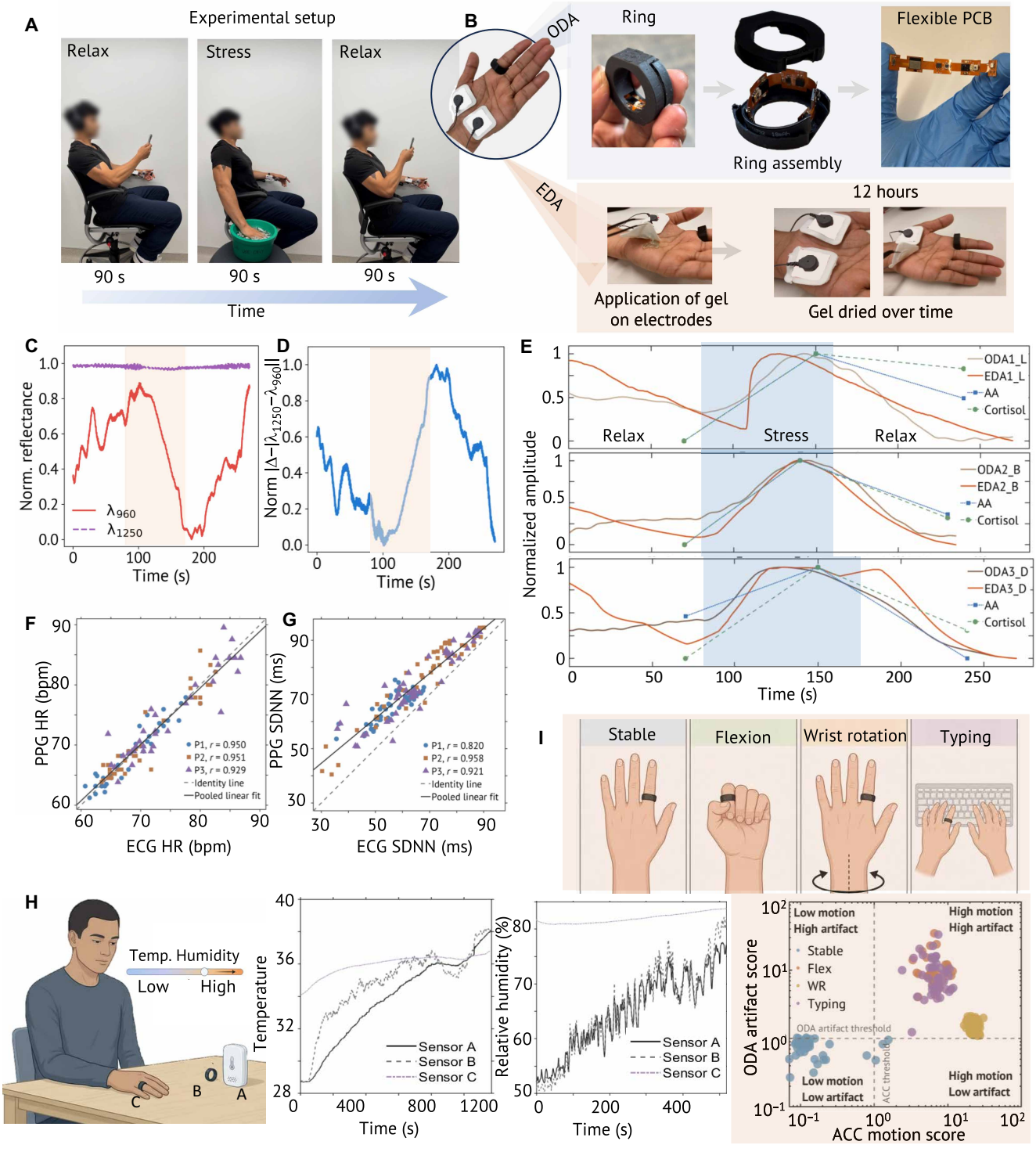


Fig. 3. Stress sensing with the ODA ring. (**A**) Experimental setup showing three 90-s phases—relaxation, stress induced through ice-water immersion, and recovery—used to evaluate sympathetic sweat gland activation. (**B**) Concurrent ODA and EDA sensor placement. Top: Flexible ODA ring and assembled device. Bottom: Gel-based EDA electrodes, for which gel degradation can limit long-term stability. (**C**) Reflected signals from the 960- and 1250-nm LEDs, with the 960-nm signal decreasing during stress whereas the 1250-nm signal provides a comparatively stable reference. (**D**) Dual-wavelength differential response during the relaxation, stress, and recovery phases. (**E**) Normalized ODA, EDA, α-amylase (AA), and cortisol responses from participants with light, brown, and dark skin pigmentation. (**F**) Correlation between ECG- and PPG-derived heart rate across three participants. (**G**) Correlation between ECG- and PPG-derived SDNN across three participants. (**H**) Environmental evaluation setup and temperature and relative humidity measurements from a commercial reference sensor, a ring placed on the table, and a worn ring. (**I**) Controlled stable, finger flexion, wrist rotation, and typing conditions, together with the window level relationship between accelerometer motion and ODA artifact scores.

Downloaded from https://www.science.org on November 13, 2026

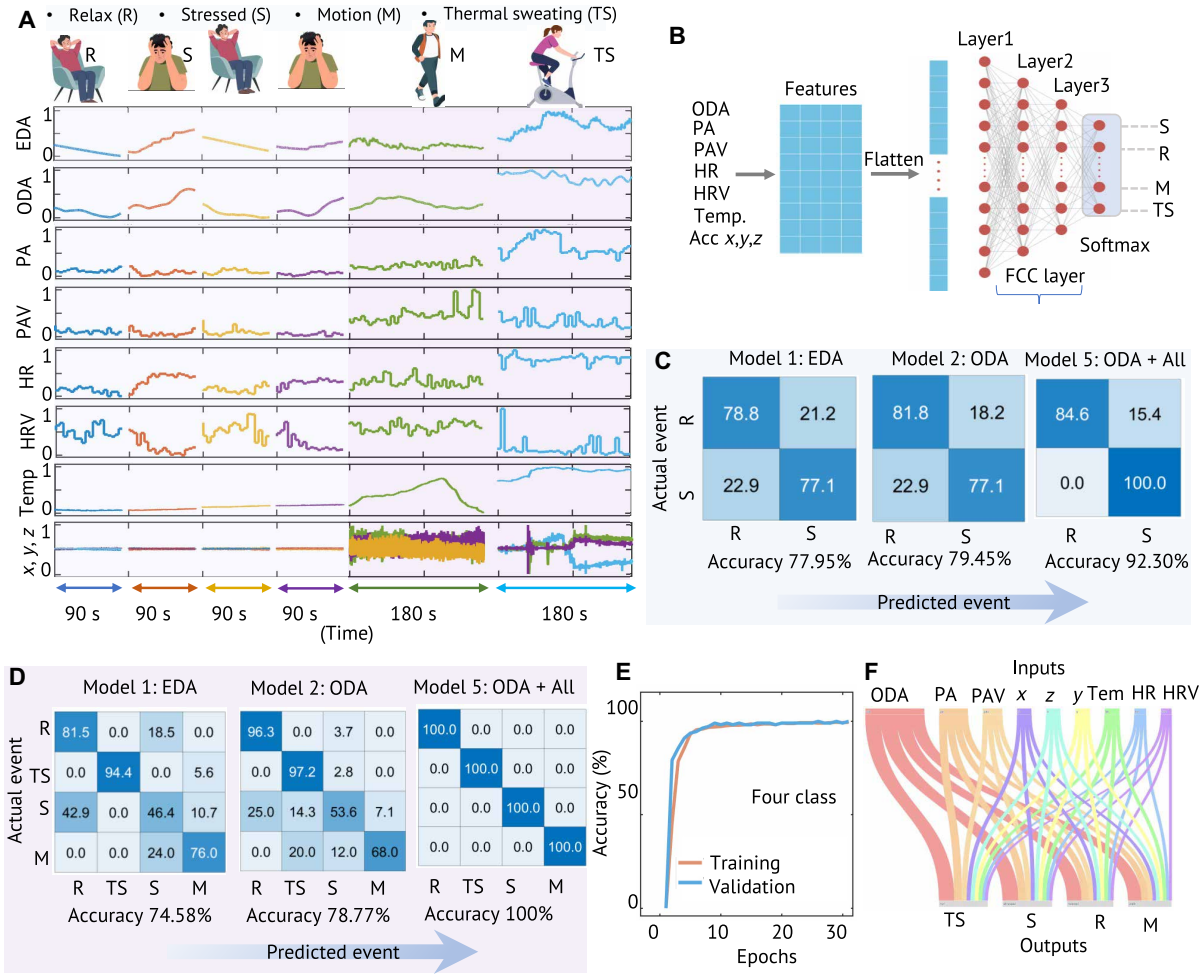


Fig. 4. Short-period stress classification using the ODA ring sensor. (**A**) Concurrent time series recorded using the EDA sensor and ODA ring during relaxation, stress, motion, and thermal sweating, including ODA, PA, PAV, HR, HRV, temperature, and three-axis acceleration. (**B**) FCNN architecture used for classification using normalized and feature-augmented sensor inputs. (**C**) Selected binary classification results for Model 1 (EDA only), Model 2 (ODA only), and Model 5 (ODA with derived physiological features, temperature, and acceleration), achieving accuracies of 77.95, 79.45, and 92.30%, respectively. (**D**) Selected four-class classification results for Model 1, Model 2, and Model 5, achieving accuracies of 74.58, 78.77, and 100%, respectively. (**E**) Training and validation accuracy of Model 5 for four-class classification. (**F**) Sankey diagram illustrating the contributions of ODA, PA, PAV, HR, HRV, temperature, and acceleration to the four classification outputs.

Model 5 reached the highest accuracy of 92.30% by incorporating temperature and accelerometer data. The lower accuracy of the derived only model compared with the ODA only model indicates that ODA contains dermal information distinct from the PPG-derived cardiovascular features. In four-class classification (Fig. 4D, fig. S23, and table S5), Models 1 and 2 exhibited similar but limited performance, with accuracies of 74.58 and 78.77%, respectively. Combining ODA with the derived physiological features, Model 4 demonstrated marked improvement with 97.15% accuracy, whereas Model 5 achieved perfect classification at 100%, with no misclassifications. Figure 4E shows rapid convergence and strong generalization in four-class classification, with a minimal training and validation accuracy gap, highlighting model robustness and reliable state differentiation. The Sankey diagram in Fig. 4F underscores the contributions of ODA, derived features, temperature, and accelerometer data, highlighting the value of multimodal integration for accurate and reliable classification.

Long-period stress classification

One of the main limitations of gel-based EDA sensors is the progressive degradation of signal quality over time due to gel drying, which lowers the signal-to-noise ratio (SNR) and impairs stress detection accuracy. To assess the long-term robustness of the ODA ring sensor, a 12-hour experiment was conducted with two participants, following the same protocol as the short-period setup. Each participant wore both the ODA ring and a gel-based EDA sensor continuously throughout the 12-hour period. Data were collected across three sessions spaced six hours apart. The first two sessions were used for training and validation, whereas the third session, conducted 12 hours after the start, served as the test set. This approach aimed to assess the sensor's stability and the generalization of classification models over extended periods. Figure 5A presents the long-term data collected from subject 01 using the gel-based EDA sensor and ODA ring sensor configured in Mode-1. As shown in Fig. 5B and figs. S24 and S25, five models were compared for

Downloaded from https://www.science.org on November 13, 2026

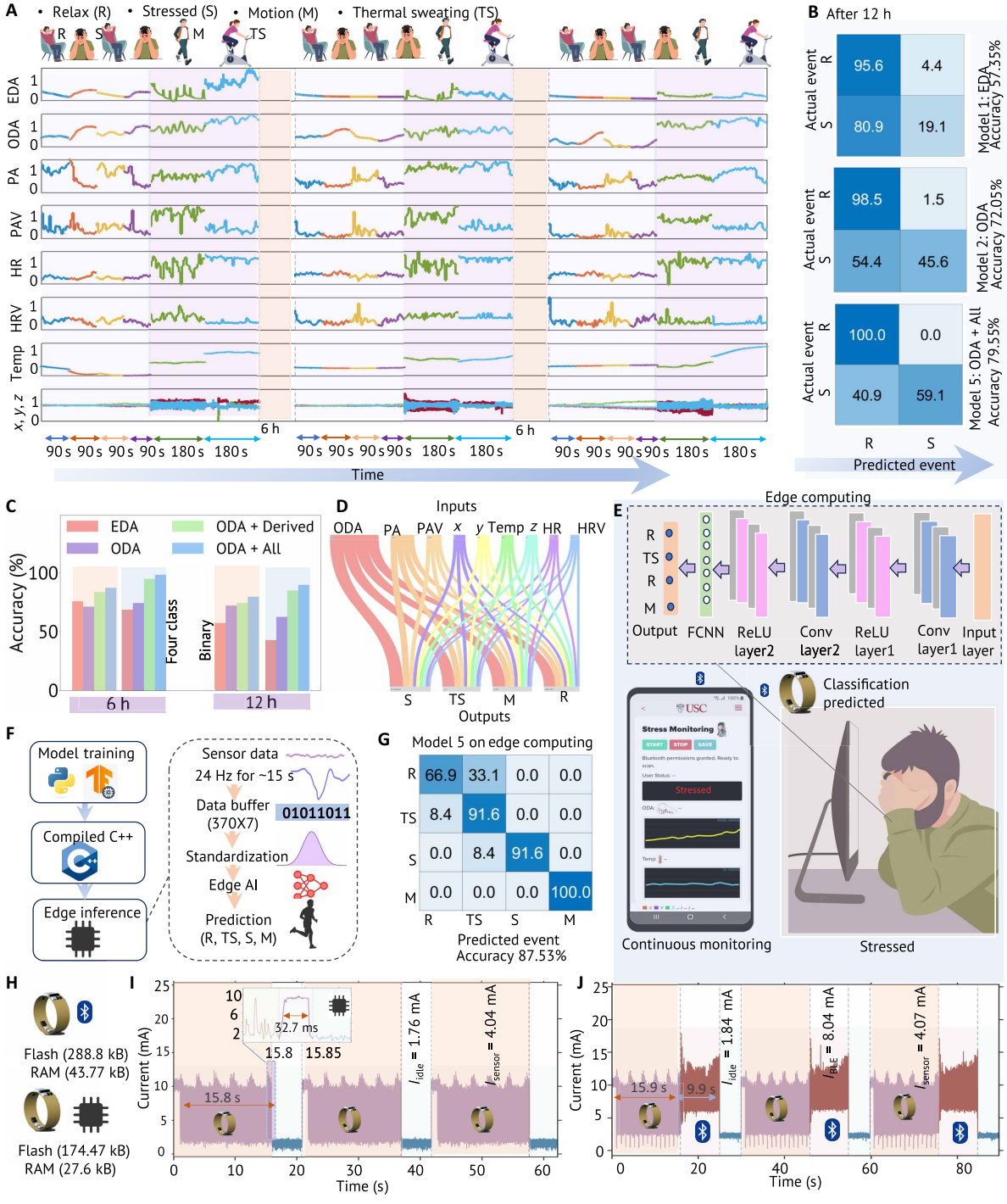


Fig. 5. Long-period stress classification and edge AI decision-making. (**A**) Long-term multimodal data collected from three sessions spaced 6 hours apart, capturing physiological signals including ODA, PA, PAV, HR, HRV, temperature, and motion (acceleration in *x*, *y*, and *z*) alongside traditional gel-based EDA signals across four conditions: relaxation (R), stress (S), motion (M), and thermal sweating (TS). h, hours. (**B**) Binary classification after 12 hours shows a marked decline in performance for gel-based EDA (Model-1), whereas Model-5 (ODA with all features) maintains an accuracy of 79.55%. (**C**) Accuracy comparison for the binary and four-class models, highlighting the advantage of integrating ODA and derived features. (**D**) Sankey diagram showing the contribution of each sensing modality to four-class classification. (**E**) Edge AI implementation of the 1D-CNN-FCNN architecture on the ODA ring for real-time decision-making with reduced computational and data transmission requirements. (**F**) On-device edge-AI pipeline, in which the trained model is compiled and deployed to the controller, which buffers 15 s of sensor data, standardizes the inputs, and performs real-time stress classification. (**G**) Confusion matrix from Model-5 on-device inference, showing an accuracy of 87.53%. (**H**) Comparison of program flash and RAM requirements for sensing with external processing and sensing with on-device edge inference. (**I**) Measured current profile for sensing and on-device edge inference, showing the common sensing period followed by 32.7 ms of inference. (**J**) Measured current profile for sensing and external processing, showing the common sensing period followed by 9.9 s of raw data transmission through BLE.

Downloaded from https://www.science.org on November 13, 2026

binary classification. Model 1 exhibited substantial performance degradation over time, with accuracy decreasing from 75.75% within 6 hours to 57.35% after 12 hours. Model 2 maintained accuracies of 71.20 and 72.05%, respectively. Model 3, using only PA, PAV, HR, and HRV, achieved 68.06% within 6 hours and 58.03% after 12 hours. Combining ODA with these derived features increased the corresponding accuracies to 83.60 and 74.30% for Model 4. Model 5 achieved the highest validation accuracy of 87.15% and a test accuracy of 79.55% after incorporating temperature and accelerometer data. As shown in figs. S26 and S27, Model 1 four-class accuracy decreased from 68.68% within 6 hours to 43.20% after 12 hours. Model 2 achieved 74.28 and 62.70%, whereas the derived-only Model 3 achieved 63.89 and 61.11%, respectively. Model 4, combining ODA with the derived physiological features, achieved 94.72% within 6 hours and 84.97% after 12 hours. Model 5 provided the highest performance, achieving 98.20 and 89.72%, respectively.

Figure 5C summarizes the average binary and four-class classification accuracies across all cohorts and conditions at 6-hour and 12-hour durations. The results show that combining ODA with derived, temperature, and motion features consistently improves classification performance, outperforming EDA-based models at all time points. The lower performance of the derived-only Model 3 relative to the models containing ODA further indicates that the ODA response provides dermal information that is distinct from the PPG-derived cardiovascular features. As shown in Fig. 5D, ODA features predominantly support classification of relaxed and stressed states, whereas temperature and motion-related inputs contribute more to thermal sweating and motion detection. These results demonstrate the stability of the ODA ring over the 12-hour evaluation. However, the reduction in EDA-based classification accuracy is specific to the commercial gel-based sensor used in this study and should not be generalized to dry electrode or ac-based EDA systems.

Edge AI–driven decision

Although Mode-1 validated the efficacy of the ODA ring sensor in stress detection, it exposed several limitations. The reliance on external devices for raw data transmission, preprocessing, and classification introduced latency, increased power consumption due to continuous wireless transmission, and raised concerns about data privacy as sensitive physiological data were transmitted externally.

To overcome these challenges, Mode-2 was developed, enabling real-time decision-making on the ring through deployment of a pretrained ML model on the microcontroller. Using long-term data from two participants, the edge implementation processed raw signals from the 960- and 1250-nm LEDs, temperature, and three axis accelerometer sensors. The baseline-corrected ODA signal was also included, resulting in a seven-channel sensor input. As illustrated in Fig. 5 (E and F), ~15 s of sensor data sampled at 24 Hz (370 × 7 samples) were buffered, standardized, and fed into a one-dimensional (1D) CNN–FCNN architecture. The CNN layers performed local temporal feature extraction, followed by a fully connected layer for classification into four physiological states. Figure 5G shows the confusion matrix from on device inference, which achieved a classification accuracy of 87.53%. The system requirements and operating tradeoffs between sensing with on device inference and sensing with Bluetooth transmission were further quantified in Fig. 5 (H to J) and table S10. The quantized INT8 model occupied 27.65 kB. Simultaneous sensing and inference implementation required 174.47 kB of program flash and 27.63 kB of static RAM, compared with 288.84 kB of flash and 43.77 kB of static RAM for the concurrent sensing and Bluetooth implementation. The greater memory requirement of the Bluetooth implementation arose primarily from the BLE protocol stack and associated communication middleware. Both approaches maintained comparable classification accuracy, with 87.53% for on device inference and 87.75% for the externally processed model. Both implementations required ~15.8 s for sensor data collection because the sensing operation was common to both approaches. After sensing, on device inference required 32.67 ms at an average current of 8.50 mA, whereas transmission of the 10.36-kB raw data window through Bluetooth required 9.90 s at 8.04 mA (Fig. 5, I and J). This represents an ~300-fold reduction in latency after sensing. The energy required for one inference was 0.916 mJ, compared with 262.7 mJ for raw data transmission, corresponding to an ~287-fold reduction for the respective inference and communication steps. For the complete operating cycle, sensing and inference consumed 0.241 J, compared with 0.507 J for sensing and Bluetooth transmission. Using a battery (21 mA·hour), the estimated endurance increased from ~492 to 1037 cycles, corresponding to 4.21 and 6.00 hours of continuous operation, respectively. The computation time and energy consumption of the external processing device were not included in this comparison.

These measurements demonstrate that on device inference maintains comparable classification accuracy while substantially reducing wearable side memory use, latency, communication energy, and dependence on external processing. The reduced requirement for continuous raw data transmission can also limit wireless exposure of physiological data. Together, these results support edge AI as an efficient and scalable approach for real-time stress monitoring within the compact ODA ring platform.

Future directions and current limitations

The ODA ring was evaluated during a time pressured arithmetic task to examine its response to cognitive stress. Two participants completed 6 min of rest, 6 min of arithmetic, and 4 min of recovery while ODA, EDA, and perceived stress were recorded (fig. S20). ODA and EDA exhibited similar responses, with Pearson correlations of $r = 0.800$ and $r = 0.654$, whereas stress scores increased after the arithmetic task and decreased during recovery. Although this evaluation involved only two participants, the observed agreement supports further investigation across larger groups and broader cognitive and psychosocial stress conditions. Surface sweat accumulation was also evaluated using Monte Carlo simulation (fig. S21). A 150-μm surface water layer increased the ODA response beyond the modeled subsurface tissue water change. Because the surface layer developed after baseline acquisition, its effect was not removed by wearer-specific baseline correction. Surface sweat accumulation therefore remains a limitation of the design. Future devices will explore passive wicking materials, microfluidic sweat transport, improved mechanical interfaces, and multimodal analysis to reduce interference from accumulated surface sweat.

Discussion

The ODA ring sensor presents a transformative approach to stress monitoring by leveraging all-optical sensing principles to monitor sweat gland activity with high precision. Unlike conventional EDA sensor, which rely on direct skin contact and is susceptible to signal degradation, the ODA ring offers a noninvasive, contactless alternative that ensures consistent and reliable measurements over extended periods. Through a combination of analytical modeling, Monte

Downloaded from https://www.science.org on November 13, 2026

Carlo simulations, and experimental validation using the cold pressor test, which is a standardized physiological stressor known to activate sympathetic pathways, we demonstrated the sensor's ability to capture stress-induced perspiration dynamics with high sensitivity. The integration of 960- and 1250-nm LEDs was optimized to enhance signal differentiation, enabling real-time monitoring of physiological stress responses while maintaining a stable optical baseline. Beyond its ability to detect sympathetic sweat gland activity, the ODA ring's optical modality inherently captures PPG signals, allowing for simultaneous extraction of cardiovascular parameters such as PA, PAV, HR, and HRV. When combined with embedded temperature and motion sensors, this multimodal dataset enhances stress classification accuracy. Our experimental results show that the ODA ring strongly correlates with EDA-based measurements, achieving an average correlation of 86%. In short-term binary classification (stress versus relaxation), the ODA ring demonstrated superior accuracy (92.3%) compared to a commercial EDA sensor (77.95%). Over long-term assessments, where EDA performance degraded to 57.35%, the ODA ring maintained an accuracy of 79.55%, highlighting its stability and robustness. In addition, in four-class classification, the ODA ring outperformed EDA sensor, achieving 100% accuracy in short-term studies and 89.72% over extended periods. To further enhance usability, we introduced edge AI–driven processing in Mode-2, where a pretrained 1D-CNN-FCNN model deployed on the ring's microcontroller enabled real-time decision-making. This markedly reduced latency, minimized energy consumption, and addressed privacy concerns associated with continuous wireless data transmission, making the ODA ring a scalable solution for continuous stress monitoring. By seamlessly integrating optical, multimodal physiological data, and edge AI, the ODA ring redefines real-time stress monitoring with high accuracy, reliability, and scalability. Its compact, contactless design enables continuous and intelligent physiological tracking, positioning it as a compelling next-generation solution for personal wellness, workplace stress management, and clinical applications—especially as demand for ring-based health wearables continues to grow. Furthermore, the optical sensing demonstrated here is scalable and applicable to noninvasive wearables in ring, watch, and patch form factors.

MATERIALS AND METHODS

Artificial sweat preparation

A low-concentrated artificial sweat was prepared by sequential dilution of stock solutions of NaCl, KCl, $CaCl_2$, and $MgCl_2$. A 1 M NaCl stock was first prepared by dissolving 584.4 mg NaCl in 10 ml of deionized (DI) water and subsequently diluted to 100 mM and then 40 mM. Similarly, a 1 M KCl solution was prepared by dissolving 745.5 mg of KCl in 10 ml of DI water, followed by serial dilution to 100 and 12 mM. For calcium chloride, 1109.8 mg of $CaCl_2$ was dissolved in 10 ml of DI water to create a 1 M solution, which was diluted stepwise to 100, 10, and 0.8 mM. A 100 mM $MgCl_2$ solution was obtained by dissolving 95.2 mg of $MgCl_2$ in 10 ml of DI water and diluted progressively to 10 mM, 1 mM, and last 0.08 mM. The final artificial sweat solution was formulated by mixing 10 ml of each diluted solution, yielding a 40-ml composition of 10 mM NaCl, 3 mM KCl, 0.2 mM $CaCl_2$, and 0.02 mM $MgCl_2$.

Fabrication of the ODA ring cover

The ODA ring covers (top and bottom) were fabricated using stereolithography (SLA) 3D printing to achieve precise dimensional accuracy and mechanical stability. The design, created in Autodesk Fusion 360, features an inner diameter of 20 mm, an outer width of 28.5 mm, and a height of 10 mm (top: 5 mm; bottom: 5 mm) ensuring seamless integration with the sensor system (fig. S28A). Printing was performed on a Formlabs Form 3B+ SLA printer using BioMed Black (BMBL-01) medical-grade resin, with a 405-nm laser curing process at a 25-μm layer resolution to ensure high-definition structural features. To optimize print quality and facilitate postprocessing, slicing parameters were set using the Formlabs PreForm software, with support density adjusted to 50 and touchpoint size reduced to 0.5 mm (fig. S28B). After printing, the fabricated structures underwent a standardized postprocessing protocol: Uncured resin was removed via a 20-min immersion in 99% isopropanol (IPA), followed by ultraviolet (UV) curing at 60°C under 405-nm light for 30 min to enhance mechanical strength. Supports were carefully detached, and the surfaces were lightly sanded and polished to ensure a smooth finish. The final fabricated ring covers (fig. S28D) exhibited high structural fidelity, minimal surface roughness, and durability, making them well suited for integration with the ODA sensor system.

Ring assembly

The assembly of the ODA ring sensor involved integrating a four-layer flexible PCB, fabricated on a 0.2-mm thick polyimide substrate, with overall assembled dimensions of 65 mm by 9 mm by approximately 2.0mm. The top layer of the PCB was dedicated to power management and wireless communication, housing a dc-dc converter (XCL101A501) responsible for efficient voltage regulation, along with two LDO regulators (S-1721A1833 and S-1200B48) to provide stable voltage outputs. On the bottom layer, key sensing components were strategically placed to optimize performance. The MAX86140 optical sensor was incorporated to enable sweat-based ODA, whereas the HS3003 and BMI270 are used for temperature and motion sensing, respectively. In addition, an nRF52 MCU (ANNA-B112) was positioned on this layer, facilitating BLE communication for real-time data transmission. A board-to-board (B2B) connector (BM46B-12DS) was used for deploying the ML model to the controller. Power to the ODA ring was supplied by a compact and flexible arc lithium-polymer (LiPo) battery (ROC: 11.8 mm, length: 28 mm, width: 6.5 mm, and thickness: 1.8 mm), which was connected in series and securely soldered onto dedicated PCB pads using thin copper wires to minimize mechanical stress and electrical resistance. A push button was integrated into the power circuitry, allowing users to manually turn the device on and off, effectively conserving battery life when not in operation.

Study protocol

The study protocol was approved by the University of Southern California Institutional Review Board (IRB HS-25-00154), and all participants provided written informed consent before participation. The experimental protocol consisted of short-term and long-term data collection phases. In the short-term phase, participants wore the ODA ring sensor alongside gel-based electrodes for EDA monitoring. The protocol included a 180-s relaxation phase with calming music, followed by a 90- to 180-s cold pressor test where participants immersed their hand in ice-cold water to induce a stress response. To assess sensor performance under movement and thermoregulatory sweating conditions, data from an additional 180-s walking session and 180-s stationary biking session (after 15 min of biking) were collected. In the long-term phase, the same protocol

Downloaded from https://www.science.org on November 13, 2026

was repeated at three time points over a 12-hour period, with 6-hour intervals between sessions. Participants continuously wore both the ODA ring sensor and EDA electrodes throughout this duration. The study included adults aged 18 years or older who were in good health and capable of completing all protocol activities. Exclusion criteria encompassed individuals with conditions preventing cold-water immersion (e.g., Raynaud's disease), skin sensitivities that could interfere with sensor placement, or cardiovascular, respiratory, or neurological conditions that posed risks. Participants were allowed to withdraw at any point, and their data were excluded from analysis.

Supplementary Materials

The PDF file includes:

Tables S1 to S11
Text S1 to S11
Figs. S1 to S28
Legend for movie S1
References

Other Supplementary Material for this manuscript includes the following:

Movie S1

REFERENCES

1. M. Chesnut, S. Harati, P. Paredes, Y. Khan, A. Foudeh, J. Kim, Z. Bao, L. M. Williams, Stress markers for mental states and biotypes of depression and anxiety: A scoping review and preliminary illustrative analysis. *Chronic Stress* **5**, 24705470211000338 (2021).
2. M. Elgendi, C. Menon, Assessing anxiety disorders using wearable devices: Challenges and future directions. *Brain Sci.* **9**, 50 (2019).
3. C. Xu, Y. Song, J. R. Sempionatto, S. A. Solomon, Y. Yu, H. Y. Y. Nyein, R. Y. Tay, J. Li, W. Heng, J. Min, A. Lao, T. K. Hsiai, J. A. Sumner, W. Gao, A physicochemical-sensing electronic skin for stress response monitoring. *Nat. Electron.* **7**, 168–179 (2024).
4. A. Mishra, M. Agrawal, A. Ali, P. Garg, Uninterrupted real-time cerebral stress level monitoring using wearable biosensors: A review. *Biotechnol. Appl. Biochem.* **70**, 1895–1914 (2023).
5. S. Yoon, J. K. Sim, Y.-H. Cho, A flexible and wearable human stress monitoring patch. *Sci. Rep.* **6**, 23468 (2016).
6. H. D. Critchley, Electrodermal responses: What happens in the brain. *Neuroscientist* **8**, 132–142 (2002).
7. W. Boucsein, *Electrodermal Activity* (Springer, 2012).
8. J. Axelrod, T. D. Reisine, Stress hormones: Their interaction and regulation. *Science* **224**, 452–459 (1984).
9. C. H. Johnson, J. Ivanisevic, G. Siuzdak, Metabolomics: Beyond biomarkers and towards mechanisms. *Nat. Rev. Mol. Cell Biol.* **17**, 451–459 (2016).
10. S. Cohen, T. Kamarck, R. Mermelstein, A global measure of perceived stress. *J. Health Soc. Behav.* **24**, 385–396 (1983).
11. C. D. Spielberger, C. Drew Edwards, R. E. Lushene, J. Montuori, D. Platzek, *STAIC Preliminary Manual for the State-Trait Anxiety Inventory for Children* (Consulting Psychologists Press, 1973).
12. G. J. Fogarty, P. Bramston, R. A. Cummins, Validation of the lifestress inventory for people with a mild intellectual disability. *Res. Dev. Disabil.* **18**, 435–456 (1997).
13. N. K. Singh, S. Chung, A.-Y. Chang, J. Wang, D. A. Hall, A non-invasive wearable stress patch for real-time cortisol monitoring using a pseudoknot-assisted aptamer. *Biosens. Bioelectron.* **227**, 115097 (2023).
14. B. Wang, C. Zhao, Z. Wang, K.-A. Yang, X. Cheng, W. Liu, W. Yu, S. Lin, Y. Zhao, K. M. Cheung, H. Lin, H. Hojaiji, P. S. Weiss, M. N. Stojanović, A. J. Tomiyama, A. M. Andrews, S. Emaminejad, Wearable aptamer-field-effect transistor sensing system for noninvasive cortisol monitoring. *Sci. Adv.* **8**, eabk0967 (2022).
15. S. Sheibani, L. Capua, S. Kamaei, S. S. A. Akbari, J. Zhang, H. Guerin, A. M. Ionescu, Extended gate field-effect-transistor for sensing cortisol stress hormone. *Commun. Mater.* **2**, 10 (2021).
16. A. Nechyporenko, M. Frohme, Y. Strelchuk, V. Omelchenko, V. Gargin, L. Ishchenko, V. Alekseeva, Galvanic skin response and photoplethysmography for stress recognition using machine learning and wearable sensors. *Appl. Sci.* **14**, 11997 (2024).
17. E. T. Attar, V. Balasubramanian, E. Subasi, M. Kaya, Stress analysis based on simultaneous heart rate variability and eeg monitoring. *IEEE J. Transl. Eng. Health Med.* **9**, 1–7 (2021).
18. S. Heo, S. Kwon, J. Lee, Stress detection with single ppg sensor by orchestrating multiple denoising and peak-detecting methods. *IEEE Access* **9**, 47777–47785 (2021).
19. M. Horowitz, N. Wilner, W. Alvarez, Impact of event scale: A measure of subjective stress. *Psychosom. Med.* **41**, 209–218 (1979).
20. S. Xu, J. Kim, J. R. Walter, R. Ghaffari, J. A. Rogers, Translational gaps and opportunities for medical wearables in digital health. *Sci. Transl. Med.* **14**, eabn6036 (2022).
21. S. Pradhan, B. D. Nicholson, S. Albin, R. L. Heise, V. K. Yadavalli, Single-use biomimetic sensors for rapid and sensitive cortisol detection in blood. *Biosens. Bioelectron. X* **12**, 100280 (2022).
22. F. Gao, C. Liu, L. Zhang, T. Liu, Z. Wang, Z. Song, H. Cai, Z. Fang, J. Chen, J. Wang, M. Han, J. Wang, K. Lin, R. Wang, M. Li, Q. Mei, X. Ma, S. Liang, G. Gou, N. Xue, Wearable and flexible electrochemical sensors for sweat analysis: A review. *Microsyst. Nanoeng.* **9**, 1 (2023).
23. Y. Liu, Q. Liu, S. Chen, F. Cheng, H. Wang, W. Peng, Surface plasmon resonance biosensor based on smart phone platforms. *Sci. Rep.* **5**, 12864 (2015).
24. Y. Wang, C. Zhao, J. Wang, X. Luo, L. Xie, S. Zhan, J. Kim, X. Wang, X. Liu, Y. Ying, Wearable plasmonic-metasurface sensor for noninvasive and universal molecular fingerprint detection on biointerfaces. *Sci. Adv.* **7**, eabe4553 (2021).
25. Y. Khan, M. L. Mauriello, P. Nowruzi, A. Motani, G. Hon, N. H. Vitale, J. Li, J. Kim, A. Foudeh, D. Duvio, E. Shols, M. Chesnut, J. A. Landay, J. T. Liphardt, L. M. Williams, K. D. Sudheimer, B. Murmann, Z. Bao, P. E. Paredes, "On stress: Combining human factors and biosignals to inform the placement and design of a skin-like stress sensor," in *Proceedings of the 2024 CHI Conference on Human Factors in Computing Systems* (Association for Computing Machinery, 2024), pp. 1–13.
26. E. Lazarou, T. P. Exarchos, Predicting stress levels using physiological data: Real-time stress prediction models utilizing wearable devices. *AIMS Neurosci.* **11**, 76–102 (2024).
27. X. Peng, D. Li, J. Quan, C. Wu, H. Li, E. Liu, H. Lianting, S. Huang, L. Kong, X. Chen, H. Yang, L. Hu, S. Wang, H. Ma, Q. Geng, A multimodal physiological and psychological dataset for human with mental stress induced myocardial ischemia. *Sci. Data* **11**, 704 (2024).
28. S. Hosseini, R. Gottumukkala, S. Katragadda, R. T. Bhupatiraju, Z. Ashkar, C. W. Borst, K. Cochran, A multimodal sensor dataset for continuous stress detection of nurses in a hospital. *Sci. Data* **9**, 255 (2022).
29. S. A. H. Aqajari, E. K. Naeini, M. A. Mehrabadi, S. Labbaf, A. M. Rahmani, N. Dutt, GSR analysis for stress: Development and validation of an open source tool for noisy naturalistic GSR data. arXiv:2005.01834 [cs.HC] (2020).
30. Y. S. Can, N. Chalabianloo, D. Ekiz, J. Fernandez-Alvarez, G. Riva, C. Ersoy, Personal stress-level clustering and decision-level smoothing to enhance the performance of ambulatory stress detection with smartwatches. *IEEE Access* **8**, 38146–38163 (2020).
31. R. Vahey, R. Becerra, Galvanic skin response in mood disorders: A critical review. *Int. J. Psychol. Psychol. Ther.* **15**, 275–304 (2015).
32. S. Greene, H. Thapliyal, A. Caban-Holt, A survey of affective computing for stress detection: Evaluating technologies in stress detection for better health. *IEEE Consum. Electron. Mag.* **5**, 44–56 (2016).
33. H. J. Han, S. Labbaf, J. L. Borelli, N. Dutt, A. M. Rahmani, Objective stress monitoring based on wearable sensors in everyday settings. *J. Med. Eng. Technol.* **44**, 177–189 (2020).
34. J. A. Miranda Calero, A. Páez-Montoro, C. López-Ongil, S. Paton, Self-adjustable galvanic skin response sensor for physiological monitoring. *IEEE Sensors J.* **23**, 3005–3019 (2023).
35. E. Mejía-Mejía, J. Allen, K. Budidha, C. El-Hajj, P. A. Kyriacou, P. H. Charlton, "Photoplethysmography signal processing and synthesis," in *Photoplethysmography: Technology, Signal Analysis and Applications*, P. A. Kyriacou, J. Allen, Eds. (Elsevier, 2022), chap. 4, pp. 69–146.
36. X. Wang, B. W. Pogue, S. Jiang, H. Dehghani, X. Song, S. Srinivasan, B. A. Brooksby, K. D. Paulsen, C. Kogel, S. P. Poplack, W. A. Wells, Image reconstruction of effective mie scattering parameters of breast tissue in vivo with near-infrared tomography. *J. Biomed. Opt.* **11**, 041106 (2006).
37. S. L. Jacques, Optical properties of biological tissues: A review. *Phys. Med. Biol.* **58**, R37–R61 (2013).
38. H. Suzaki, N. Kobayashi, T. Nagaoka, K. Iwasaki, M. Umezu, S. Takeda, T. Togawa, "Noninvasive measurement of total hemoglobin and hemoglobin derivatives using multiwavelength pulse spectrophotometry—In vitro study with a mock circulatory system," in *2006 International Conference of the IEEE Engineering in Medicine and Biology Society* (IEEE, 2006), pp. 799–802.
39. N. Bosschaart, G. J. Edelman, M. C. G. Aalders, T. G. van Leeuwen, D. J. Faber, A literature review and novel theoretical approach on the optical properties of whole blood. *Lasers Med. Sci.* **29**, 453–479 (2014).
40. Y. Hasanpoor, K. Motaman, B. Tarvirdizadeh, K. Alipour, M. Ghamari, "Stress detection using ppg signal and combined deep CNN-MLP network," in *2022 29th National and 7th International Iranian Conference on Biomedical Engineering (ICBME)* (IEEE, 2022), pp. 223–228.
41. S. L. Jacques, D. J. McAuliffe, The melanosome: Threshold temperature for explosive vaporization and internal absorption coefficient during pulsed laser irradiation. *Photochem. Photobiol.* **53**, 769–775 (1991).
42. G. M. Hale, M. R. Querry, Optical constants of water in the 200-nm to 200-µm wavelength region. *Appl. Optics* **12**, 555–563 (1973).
43. L. G. Henyey, J. L. Greenstein, Diffuse radiation in the galaxy. *Astrophys. J.* **93**, 70–83 (1941).
44. V. G. Kanellis, A review of melanin sensor devices. *Biophys. Rev.* **11**, 843–849 (2019).

Downloaded from https://www.science.org on November 13, 2026

Acknowledgments
Funding: This work was supported by the National Science Foundation (award no. 2533498 to Y.K.) and the Google Research Scholar Award (to Y.K.). **Author contributions:** Conceptualization: Y.K. and M.F.H. Methodology: M.F.H., Y.K., D.V.A., and M.A. Investigation: A.K.M.R., M.F.H., L.X., M.S.I., S.T., and E.R. Formal analysis: M.F.H., S.D., and Y.K. Software: M.F.H. and X.Y. Resources: A.B., G.M.L., B.B.-G., and A.F. Writing—original draft: M.F.H., S.D., and Y.K. Writing—review and editing: M.F.H., S.D., D.V.A., L.X., M.S.I., A.K.M.R., S.T., X.Y., E.R., M.A., A.B., G.M.L., B.B.-G., A.F., and Y.K. **Competing interests:** M.F.H. and Y.K. are inventors on a US provisional patent application titled "Optodermal Wearable Device for Contactless Stress Monitoring" (serial no. 63/928,394), filed by the University of Southern California on 1 December 2025. The patent application is currently pending. The other authors declare that they have no competing interests. **Data, code, and materials availability:** All data and code needed to evaluate and reproduce the results in the paper are present in the paper and/or the Supplementary Materials. This study did not generate new materials.

Submitted 8 March 2026
Accepted 9 October 2026
Published 13 November 2026
10.1126/sciadv.aeh0459

Downloaded from https://www.science.org on November 13, 2026

Science Advances

All-optical sensing of dermal activity enables an AI-powered wearable ring for continuous stress monitoring

Md Farhad Hassan, Shounak Das, Dolendra Vikas Addepalli, Leikhang Xiong, Mohammad Shafiqul Islam, A. K. M. Rakib, Samiha Tasnim, Xiao Yu, Emily Rawson, Mohammed Arfan, Antonin Brun, Gale M. Lucas, Burçin Becerik-Gerber, Adam Frank, and Yasser Khan

Sci. Adv. **12** (46), eaeh0459. DOI: 10.1126/sciadv.aeh0459

View the article online
https://www.science.org/doi/10.1126/sciadv.aeh0459
Permissions
https://www.science.org/help/reprints-and-permissions

Downloaded from https://www.science.org on November 13, 2026

Use of this article is subject to the Terms of service

Science Advances (ISSN 2375-2548) is published by the American Association for the Advancement of Science. 1200 New York Avenue NW, Washington, DC 20005. The title *Science Advances* is a registered trademark of AAAS.

Copyright © 2026 The Authors, some rights reserved; exclusive licensee American Association for the Advancement of Science. No claim to original U.S. Government Works. Distributed under a Creative Commons Attribution NonCommercial License 4.0 (CC BY-NC).

Science Advances
AAAS

Supplementary Materials for

All-optical sensing of dermal activity enables an AI-powered wearable ring for continuous stress monitoring

Md Farhad Hassan *et al.*

Corresponding author: Yasser Khan, yasser.khan@usc.edu

Sci. Adv. **12**, eaeh0459 (2026)
DOI: 10.1126/sciadv.aeh0459

The PDF file includes:

Tables S1 to S11
Text S1 to S11
Figs. S1 to S28
Legend for movie S1
References

Other Supplementary Material for this manuscript includes the following:

Movie S1

Table S1. Summary of different stress sensing methods.

Methods	Ref.	Sensing approach	Sensing markers	Continuous monitoring	Location of sensor	Challenges
Self-reporting	[10]	10 to 14 item questionnaire assessing perceived stress	Psychological perception of stress	N/A	N/A	Influenced by recall bias; Captures general stress perception rather than real-time responses
	[11]	20-item 4-point likert scale measuring state anxiety	State anxiety as a response to stress	N/A	N/A	Measures anxiety over direct physiological stress markers; Requires literacy and comprehension
	[12]	Questionnaire for mild intellectual disabilities (MID): measuring impact of daily stressors	Daily stress experiences	N/A	N/A	Tailored for mild intellectual disabilities; May require assistance for completion
Biofluid analysis	[13]	Wearable microfluidic sweat sensor	Cortisol measurement	$\sim$ 1.5 hrs	Sweat patches on the back of the lower neck	Limited sensor lifespan; Signal interference challenges; Users susceptible to skin discomfort
	[14]	Smartwatch with aptamer-FET array	Cortisol measurement	$\sim$ 2 hrs	Smartwatch	Continous extraction of saliva or sweat is required.
	[15]	3D lab-on-chip sensor with graphene/aptamer-based sensor	Cortisol measurement	Duration not specified	Wearable sensor on skin (e.g., forehead, wrist, underarm)	Continuous extraction of sweat is required.
Physiological sensing	[17]	Wearable electrode based non-invasive device.	EEG, ECG features	Short-term monitoring ($\sim$15 min)	EEG: Scalp; ECG: Underarms/right abdominal cavity	Sensing devices are not suitable for daily use, gel-based electrodes dries over time
	[16]	Wearable non-invasive (optical, electrical) device	HRV, EDA features	Short-term monitoring ($\sim$15 min)	Finger, earlobe (PPG); finger, wrist (EDA)	PPG and EDA sensors require separate AFE processing; Less portable due to multiple sensors
	[18]	Wearable non-invasive optical device.	PPG features	Duration not specified	Chest, wrist	Long-term monitoring not explored; single modality might lead to misinterpretation

.

Table S2. Comparative analysis of different physiological stress sensing approaches.

Ref.	Sensing approach	Sensing markers	Continuous monitoring	Sensor location	Edge computing	Accuracy
[16]	Wearable non-invasive (optical, electrical) device	HRV, EDA features	Short-term monitoring (∼15 min)	Finger, earlobe (PPG); finger, wrist (EDA)	No	83.30%
[30]	Wrist-worn devices	HRV, EDA, PPG	Empatica: 2 days; Samsung: 4 hrs	Wrist	No	94.44%
[18]	Chest, wrist devices	PPG	Duration not specified	Chest, Wrist	No	96.50%
[40]	Wrist-worn device	PPG	Duration not specified	Wrist	No	82.00%
[29]	Chest, wrist devices	EDA	Duration not specified	Chest, Wrist	No	92.00%
This Work	ODA ring	ODA, PA, PAV, HRV, temp, acceleration	Short (15 min) long (12 hrs)	Finger	Yes	15 min: 100%, 12 hrs: 89.73%

Table S3. Comparative analysis between different features of EDA and ODA sensing

Signal type	Sensing Modalities	Sensor skin interface	Drift over time	Baseline correction	Accuracy (%) Binary			Accuracy (%) Multiclass		
					15 min	6hr	12hr	15 min	6hr	12hr
Electrical	EDA	Contact based	Yes	Required	77.95	75.75	57.35	74.58	68.68	43.20
Optical	ODA, PPG	Contactless	No	In-sensor	92.30	87.15	79.55	100	98.20	89.72

.

Table S4. Performance metrics of the ML models in the short-term binary class (stress and relax) data sets.

Model	Validation Accuracy	Weighted Precision	Weighted Recall	Weighted F1-Score	Area under ROC Curve	Loss Value
EDA	77.95%	0.78	0.775	0.779	0.78	0.56
ODA	79.45%	0.795	0.795	0.794	0.79	0.46
ODA + Derived	88.80%	0.891	0.888	0.888	0.89	0.29
ODA + Derived + Temp. + Acc.	92.30%	0.933	0.923	0.922	0.92	0.18

Table S5. Performance metrics of the ML models in the short-term four-class (stress, relax, motion, and thermal sweating) data sets.

Model	Validation Accuracy	Weighted Precision	Weighted Recall	Weighted F1-Score	Area under ROC Curve	Loss Value
EDA	74.58%	0.75	0.746	0.745	0.92	0.53
ODA	78.77%	0.795	0.788	0.777	0.93	0.58
ODA + Derived	97.15%	0.972	0.972	0.971	1.00	0.11
ODA + Derived + Temp. + Acc.	100.00%	1.00	1.00	1.00	1.00	0.02

Table S6. Validation data performance metrics of the ML models in the long-term binary class (stress and relax) data sets.

Model	Validation Accuracy	Weighted Precision	Weighted Recall	Weighted F1-Score	Area under ROC Curve	Loss Value
EDA	75.75%	0.774	0.758	0.754	0.76	0.56
ODA	71.20%	0.712	0.712	0.712	0.71	0.52
ODA + Derived	83.60%	0.877	0.836	0.832	0.80	0.31
ODA + Derived + Temp. + Acc.	87.15%	0.887	0.872	0.857	0.87	0.22

Table S7. Test data performance metrics of the ML models in the long-term binary class (stress and relax) data sets.

Model	Test Accuracy	Weighted Precision	Weighted Recall	Weighted F1-Score	Area under ROC Curve
EDA	57.35%	0.678	0.574	0.501	0.57
ODA	72.05%	0.806	0.721	0.699	0.74
ODA + Derived	74.30%	0.759	0.743	0.74	0.74
ODA + Derived + Temp. + Acc.	79.55%	0.855	0.796	0.787	0.79

Table S8. Validation data performance metrics of the ML models in the long-term four-class (stress, relax, motion, and thermal sweating) data sets.

Model	Validation Accuracy	Weighted Precision	Weighted Recall	Weighted F1-Score	Area under ROC Curve	Loss Value
EDA	68.68%	0.703	0.687	0.685	0.87	0.88
ODA	74.28%	0.830	0.747	0.764	0.92	0.65
ODA + Derived	94.72%	0.904	0.947	0.924	0.99	0.12
ODA + Derived + Temp. + Acc.	98.20%	0.965	0.965	0.964	1.00	0.05

Table S9. Test data performance metrics of the ML models in the long-term four-class (stress, relax, motion, and thermal sweating) data sets.

Model	Test Accuracy	Weighted Precision	Weighted Recall	Weighted F1-Score	Area under ROC Curve
EDA	43.20%	0.441	0.432	0.39	0.74
ODA	62.70%	0.579	0.68	0.573	0.86
ODA + Derived	84.97%	0.856	0.861	0.845	0.95
ODA + Derived + Temp. + Acc.	89.72%	0.918	0.897	0.894	0.94

Table S10. System level comparison of on device Edge inference and BLE based external processing using the same 370×7 sensor data window.

Metric	Sensing and Edge	Sensing and Ext. Processing
Flash requirement	174.47 kB (33.1%) INT8 model: 27.65 kB	288.84 kB (54.7%) No model stored on the wearable
RAM requirement	27.63 kB static RAM (43.0%) 10.36 kB input data buffer 14.30 kB inference tensor arena	43.77 kB static RAM (68.1%) 10.36 kB input data buffer BLE protocol stack and communication middleware
Classification accuracy	87.53%	87.75%
Post sensing latency	32.67 ms On device inference	9.90 s Raw data BLE transmission
Energy consumption	0.916 mJ per inference 0.241 J per complete cycle	262.7 mJ per BLE transmission 0.507 J per complete cycle
21 mAh battery endurance	Approximately 1,037 complete cycles Approximately 6.00 h continuous operation	Approximately 492 complete cycles Approximately 4.21 h continuous operation

The selected microcontroller provides 64.29 kB of available RAM and 527.62 kB of available program flash. The updated sensing and Edge implementation requires 174.47 kB of program flash, including the 27.65 kB INT8 model. Its estimated static RAM requirement is 27.63 kB, including a 10.36 kB input data buffer and a 14.30 kB inference tensor arena. The sensing and external processing implementation requires 288.84 kB of program flash and an estimated 43.77 kB of static RAM. It uses the same 10.36 kB input data buffer and includes the ArduinoBLE, Mbed, and Cordio communication resources.

Energy was calculated using a 3.3 V supply and the measured average current and duration of each operating phase. The Edge cycle consisted of 15.8 s of sensing at 4.04 mA, 32.67 ms of on device inference at 8.50 mA, and 5 s of sleep at 1.76 mA. The external processing cycle consisted of 15.9 s of sensing at 4.07 mA, 9.90 s of raw data BLE transmission at 8.04 mA, and 5 s of sleep at 1.84 mA. Battery endurance was estimated using the full nominal capacity of a 21 mAh battery. The computation time and energy consumption of the external host were not included.

S1 Analytical Modeling of ODA Sensing

The Beer–Lambert law provides a fundamental framework for describing the attenuation of light as it propagates through an absorbing medium. This principle states that the decrease in light intensity is proportional to both the incident light intensity and the concentration of the absorbing species within the medium. Mathematically, it is expressed as:

$$\frac{dI}{dx} = -kI \tag{1}$$

where I represents the light intensity at a given depth x, and k is the absorption coefficient, which depends on the optical properties of the medium. By integrating this equation over an optical pathlength d, the standard form of the Beer–Lambert law is obtained:

$$I_t = I_0 e^{-\mu d C} \tag{2}$$

where I_t is the transmitted intensity, I_0 is the incident intensity, μ is the absorption coefficient, d is the optical pathlength, and C is the concentration of the absorbing species.

However, biological tissues introduce additional complexity because of the presence of scattering structures together with multiple absorbing chromophores. The modified Beer–Lambert law (MBLL) extends the classical model by incorporating a differential pathlength factor (DPF), which accounts for the increased optical path caused by scattering. The MBLL is given as:

$$A_\lambda = \varepsilon_\lambda \cdot l_\lambda \cdot C + G_\lambda \tag{3}$$

where ε_λ is the extinction coefficient, $l_\lambda = d \cdot DPF_\lambda$ represents the effective optical pathlength, C is the concentration of the absorber, and G_λ accounts for scattering-induced baseline variations.

The DPF is a wavelength-dependent parameter that adjusts for the increased photon travel distance caused by scattering within the tissue. The introduction of G_λ accounts for systematic attenuation associated with tissue scattering and the optical measurement configuration.

The interaction of light with biological tissue is fundamentally governed by absorption and scattering mechanisms, leading to exponential attenuation of light intensity as it propagates through the medium. In a heterogeneous structure such as the human finger, multiple biological components including melanin, oxyhemoglobin, deoxyhemoglobin, tissue water, and interstitial body fluids act as absorbers and collectively influence the detected reflected intensity. This interaction follows the principles described by the MBLL, which accounts for the cumulative attenuation induced by multiple absorbers within the optical path:

$$I_\lambda^t(t) = I_\lambda^0 \exp\left[-\sum_{i=1}^{j} \varepsilon_{\lambda i} C_i(t) l_{\lambda i} - G_\lambda\right] \tag{4}$$

where $I_\lambda^t(t)$ is the detected reflected intensity at wavelength λ, I_λ^0 represents the incident intensity emitted by the source, $\varepsilon_{\lambda i}$ is the wavelength-dependent extinction coefficient of the i-th absorber, $C_i(t)$ is the concentration of the corresponding biological constituent, $l_{\lambda i}$ is its effective optical pathlength, and G_λ accounts for wavelength-dependent scattering and system attenuation.

To describe the stress-responsive optical component while accounting for the surrounding tissue, the wavelength-dependent background attenuation is defined as

$$K_\lambda(t) = \sum_{i \in \mathcal{C}_{\text{bg}}} \varepsilon_{\lambda i} C_i(t) l_{\lambda i} + G_\lambda, \tag{5}$$

where $\mathcal{C}_{\text{bg}}$ includes melanin, oxyhemoglobin, deoxyhemoglobin, baseline tissue water, interstitial fluids, and other background tissue constituents. Therefore, $K_\lambda(t)$ represents the wavelength-dependent attenuation associated with the optical properties of the surrounding tissue. Variations in tissue composition and anatomical structure, including epidermal thickness, influence the detected intensity through the corresponding concentrations and effective optical pathlengths.

The detected reflected intensity at wavelength λ can then be expressed as

$$I_\lambda^t(t) = I_\lambda^0 \exp\left[-K_\lambda(t) - \mu_\lambda l_{\lambda,\text{SS}} C_{\text{SS}}(t)\right], \tag{6}$$

where $C_{\text{SS}}(t)$ represents the effective stress-responsive change in sweat-gland-associated tissue water content, μ_λ is its wavelength-dependent absorption coefficient, and $l_{\lambda,\text{SS}}$ is the corresponding effective optical pathlength.

For the ODA sensor design, a dual-wavelength configuration is employed. The sensing wavelength, λ_1, is selected to provide a pronounced optical response to stress-associated changes in sweat-gland-related tissue water content. The reference wavelength, λ_2, is selected to exhibit a comparatively negligible response to the same change, thereby providing a reference for differential measurement. The specific sensing and reference wavelengths are identified through the simulation and experimental optimization described in the following sections.

The detected reflected intensity from the sensing wavelength during relaxed and stressed conditions can be expressed as

$$I_{\text{sense}} = \begin{cases} I_{\lambda_1}^{\text{relax}} = I_{\lambda_1}^0 \exp\left[-K_{\lambda_1}^{\text{relax}} - \mu_{\lambda_1} l_{\lambda_1,\text{SS}} C_{\text{SS-relax}}\right], \\ I_{\lambda_1}^{\text{stress}} = I_{\lambda_1}^0 \exp\left[-K_{\lambda_1}^{\text{stress}} - \mu_{\lambda_1} l_{\lambda_1,\text{SS}} C_{\text{SS-stress}}\right]. \end{cases} \tag{7}$$

where $I_{\lambda_1}^{\text{relax}}$ and $I_{\lambda_1}^{\text{stress}}$ are the detected reflected intensities from the sensing wavelength under relaxed and stressed conditions, respectively. The sensing wavelength is selected such that the difference between these two signals is sufficiently large for detecting stress-associated dermal changes.

Similarly, the detected reflected intensity from the reference wavelength is expressed as

$$I_{\text{base}} = \begin{cases} I_{\lambda_2}^{\text{relax}} = I_{\lambda_2}^{0} \exp\left[-K_{\lambda_2}^{\text{relax}} - \mu_{\lambda_2} l_{\lambda_2,\text{SS}} C_{\text{SS-relax}}\right], \\ I_{\lambda_2}^{\text{stress}} = I_{\lambda_2}^{0} \exp\left[-K_{\lambda_2}^{\text{stress}} - \mu_{\lambda_2} l_{\lambda_2,\text{SS}} C_{\text{SS-stress}}\right]. \end{cases} \tag{8}$$

where $I_{\lambda_2}^{\text{relax}}$ and $I_{\lambda_2}^{\text{stress}}$ are the detected reflected intensities from the reference wavelength under relaxed and stressed conditions, respectively. The reference wavelength is selected to exhibit a comparatively smaller variation in response to the stress-associated change.

The uncorrected dual-wavelength differential signal is defined as

$$\Delta I_{\text{raw}}(t) = I_{\text{base}}(t) - I_{\text{sense}}(t). \tag{9}$$

The initial separation between the sensing and reference wavelength signals depends on the optical properties of the tissue and the sensor–skin configuration. Therefore, an initial resting interval, $\mathcal{T}_0$, is used to establish a wearer-specific dual-wavelength reference. The mean detected intensity at each wavelength during this interval is calculated as

$$\bar{I}_{\lambda,0} = \frac{1}{N_0} \sum_{t \in \mathcal{T}_0} I_{\lambda}^{t}(t), \tag{10}$$

where N_0 is the number of samples within the baseline interval. The initial dual-wavelength separation is then calculated as

$$\Delta_0 = \left|\bar{I}_{\lambda_2,0} - \bar{I}_{\lambda_1,0}\right|. \tag{11}$$

The baseline-corrected ODA signal is defined as

$$\text{ODA}(t) = \left|\Delta_0 - \left|I_{\text{base}}(t) - I_{\text{sense}}(t)\right|\right|. \tag{12}$$

This formulation establishes the initial resting response near zero and quantifies the magnitude of subsequent deviations in the dual-wavelength separation relative to the wearer-specific resting baseline.

To quantify the effectiveness of the ODA sensor in distinguishing stress from relaxation, the ODA sensitivity is expressed as

$$\begin{aligned} \text{ODA}_{\text{sensitivity}} &= \text{ODA}^{\text{stress}} - \text{ODA}^{\text{relax}} \\ &= \left|I_{\lambda_2}^{\text{relax}} - I_{\lambda_1}^{\text{relax}}\right| - \left|I_{\lambda_2}^{\text{stress}} - I_{\lambda_1}^{\text{stress}}\right|. \end{aligned} \tag{13}$$

This model illustrates how the ODA response depends on the incident light intensity, wavelength-dependent absorption, effective optical pathlength, background tissue attenuation, and stress-associated changes in sweat-gland-related tissue water content. The sensing wavelength provides sensitivity to the physiological change of interest, while the reference wavelength enables differential measurement of the optical response. Establishing the initial dual-wavelength separation during a resting period provides a wearer-specific reference, allowing subsequent changes in the wavelength separation to be expressed as the ODA signal. Therefore, appropriate wavelength selection and baseline referencing enhance the sensitivity and consistency of the ODA sensor for optical monitoring of dermal activity.

S2 Simulation

Table S11. List of variables used for modeling the tissue and their descriptions.

Symbol	Description
μ_a	Absorption coefficient (cm^{-1})
μ_s	Scattering coefficient (cm^{-1})
f_{Ray}	Fraction of scattering at 500 nm due to Rayleigh scattering (small particles $\ll$ 500 nm diameter)
$f_{\text{mie}} = 1 - f_{\text{Ray}}$	Fraction of scattering at 500 nm due to Mie scattering (large particles $\gtrsim$ 500 nm diameter)
μ_s'	Reduced scattering coefficient (cm^{-1})
a'	Value of μ_s' at 500 nm
b_{Mie}	Mie scattering power
S_{HGb}	Oxygen saturation of mixed arterio-venous vasculature
B	Average blood volume fraction ($f_{v.\text{blood}}$)
W	Water content ($f_{v.\text{water}}$)
Bili	Bilirubin concentration (C (M))
β_C	β-carotene concentration (C (M))
F	Fat content ($f_{v.\text{fat}}$)
M	Melanosome volume fraction ($f_{v.\text{melanosome}}$) or molar concentration of melanin monomers (C (M))
λ	Wavelength of light from source
T	Fraction of light transmitted through the medium (dimensionless)
L	Path length (cm)
n''	Imaginary part of the refractive index of the medium
$f_{v.i}$	Volume fraction of the i-th chromophore
$\mu_{a.i}$	Absorption coefficient of the i-th chromophore
Δs	step in cm

To model the light-tissue interaction of a generalized tissue *in vivo*, an absorption coefficient (μ_a [cm^{-1}]) and a reduced scattering coefficient (μ_s' [cm^{-1}]) have been used. The reduced scattering coefficient describes the scattering properties of biological tissues with respect to wavelength. It takes into account the amount of light scattered as well as multiple scattering averages. The reduced scattering coefficient has been modeled using Rayleigh and Mie scattering contributions, which, depending on particle size in relation to light wavelength, represent the two main scattering mechanisms. Despite the fact that Mie scattering theory is applicable to a dielectric sphere in a uniform background medium, natural scattering phenomena have been successfully interpreted using such approximations.[36] The sphere can be of any arbitrary size. In contrast, Rayleigh scattering specifically describes the scenario of Rayleigh limit of Mie scattering where the particles are much smaller than the wavelength of the light.[37]The reduced scattering coefficient (μ_s' [cm^{-1}]) is expressed as:[37]

$$\mu_s'(\lambda) = a' \left(f_{\text{Ray}} \left(\frac{\lambda}{500\,(\text{nm})} \right)^{-4} + (1 - f_{\text{Ray}}) \left(\frac{\lambda}{500\,(\text{nm})} \right)^{-b_{\text{Mie}}} \right). \tag{14}$$

The wavelength of light has a significant impact on Rayleigh scattering. When the wavelength gets shorter, the amount of Rayleigh scattering rapidly rises as the scattering intensity is proportional to λ^{-4}. So if the wavelength is halved, the scattering will increase by $2^4 = 16$ times. The typical value for b_{Mie} is 0 to 2 for different tissue types. So, Mie scattering depends on the wavelength, but not as strongly as Rayleigh scattering due to $\lambda^{-b_{\text{Mie}}}$ dependence. The strength of Mie scattering reduces with increasing wavelength, although the decline is gradual, whereas Rayleigh scattering rapidly declines with increasing wavelength due to λ^{-4} dependence. So, at longer wavelengths (e.g., red or infrared light), the Mie scattering contribution dominates. The scattering coefficient μ_s (cm^{-1}) is the likelihood of light scattering per unit distance. It can be expressed in terms of μ_s' and anisotropy of scatter, g:[37]

$$\mu_s' = \mu_s(1 - g) \tag{15}$$

The anisotropy of scatter (g) is a dimensionless quantity that describes the average directionality of light scattering in a medium. This is expressed by $g = \langle \cos\theta \rangle$. A value of $g = 1$ means perfect forward scattering, and $g = -1$ means perfect backward scattering. Biological tissues show a forward-directed scatter (but not perfectly), with values being around 0.9.

When light is incident on the tissue, it will absorb a fraction of the incident light. This absorption is a measure of how much light energy is absorbed by the tissue per unit distance as the light travels through the tissue. It is given by the following equation:[37]

$$\mu_a = -\frac{1}{T}\frac{\partial T}{\partial L}, \tag{16}$$

The relationship between light intensity and distance is described by the Beer-Lambert law:[37]

$$I(L) = I_0 e^{-\mu_a L} \tag{17}$$

$$T = \frac{I}{I_0} = e^{-\mu_a L} \tag{18}$$

Absorption coefficient is dependent on wavelength, given by:[37]

$$\mu_a = \frac{4\pi n''}{\lambda}. \tag{19}$$

The total absorption coefficient in a tissue can be expressed as the sum of contributions from individual chromophores given by:[37]

$$\mu_a = \sum_i f_{v.i}\mu_{a.i}. \tag{20}$$

For a generic tissue, the total absorption coefficient was defined as:[37]

$$\mu_a = BS\mu_{a.\text{oxy}} + B(1-S)\mu_{a.\text{deoxy}} + W\mu_{a.\text{water}} + F\mu_{a.\text{fat}} + M\mu_{a.\text{melanosome}} + 2.3C_{\text{bili}}\varepsilon_{\text{bili}} + 2.3C_{\beta C}\varepsilon_{\beta C}. \tag{21}$$

Absorption of melanosome interior was calculated by the following equation:[41]

$$\mu_{a.\text{melanosome}} = \left(679\,\text{cm}^{-1}\right)\left(\frac{\lambda}{500\,\text{nm}}\right)^{-3.33}. \tag{22}$$

In order to model the tissue, we have created a 1000 μm $\times$ 1000 μm $\times$ 1000 μm (x, y, z dimensions) space to simulate the light-tissue interaction, as shown in Figure S1. The source and detector are located 100 μm above the skin. The 100 μm between the source and the skin has been taken as air. Then there is a 60 μm epidermis layer, and the rest of the layer is dermis. A 100 μm blood vessel is located in the middle of the dermis. The tissue has been illuminated by a source located at $(x, y) = (-250\,\mu\text{m}, -250\,\mu\text{m})$ with a 300 μm radius.

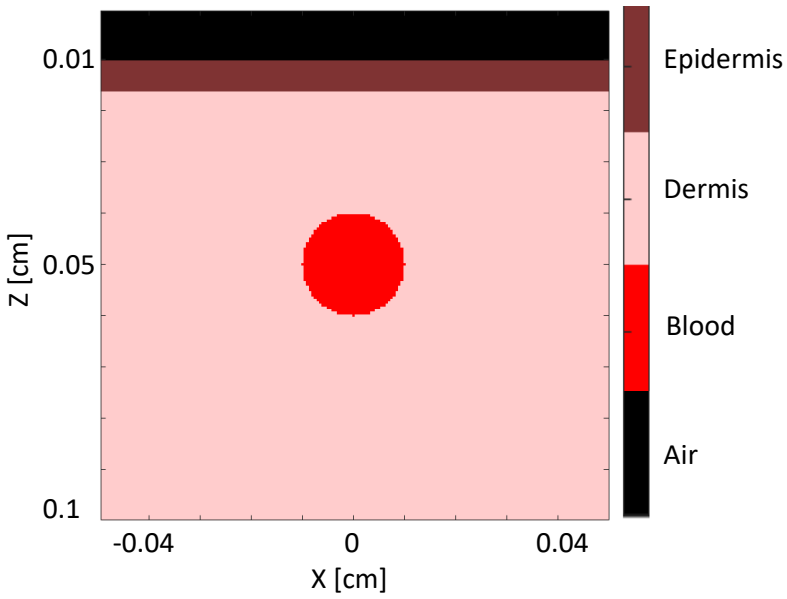


Figure S1. Tissue model for light-tissue interaction simulation. Multilayer tissue structure modeled for Monte Carlo simulation of ODA. The layers include a 60 µm epidermis, 840 µm dermis, and a central 100 µm blood vessel within the dermis. The source is placed at $x, y = (-250\,\mu\text{m}, -250\,\mu\text{m})$, with the detector at $x > 50\,\mu$m, and a 100 µm air layer separates the source from the tissue. Regions are color-coded: black (air), dark brown (epidermis), pink (dermis), and red (blood vessel), enabling detailed modeling of photon absorption and scattering.

The detector has been placed at $x > 50\,\mu$m. The data for the absorption coefficient of water vs. wavelength were taken from Hale *et al.*[42] The absorption coefficient for oxygenated and deoxygenated whole blood (150 g hemoglobin/liter) is based on Graetzer and Kollias (W.B. Gratzer, Med Res Council Labs, Holly Hill, London, and N. Kollias, Wellman Laboratories, Harvard Medical School, Boston), for 300 nm to 1000 nm. For wavelengths above 1000 nm, the data were taken from Suzaki *et al.*[38] and Bosschaart *et al.*[39]

After the tissue model has been built, a Monte Carlo simulation was performed, and the source code is based on the following website: omlc. The core algorithm follows the photon "hop–drop–spin–check" approach widely used in Monte Carlo light transport simulations.

Photons are launched from the source to the tissue medium, which has absorption, scattering, and anisotropy properties. Initially, each photon is launched with a given weight, position, and direction based on the source specification. The photon is propagated repeatedly by the algorithm until it dies. In the hop state, the photon samples a random distance to travel based on the exponential distribution determined by the scattering coefficient:

$$s = \frac{-\ln(\text{rnd})}{\mu_s}, \tag{23}$$

where rnd is a uniform random number in (0, 1]. In the Drop portion, the photon deposits some of its weight according to Beer's law:

$$\text{absorb} = W \times \left(1 - e^{-\mu_a \Delta s}\right), \tag{24}$$

The photon weight is reduced by this amount:

$$\text{absorb} = W - \text{absorb} \tag{25}$$

After each hop, the photon direction changes ("spin") according to the Henyey–Greenstein phase function given by:[43]

$$p(\theta) = \frac{1}{4\pi} \frac{1 - g^2}{\left(1 + g^2 - 2g\cos\theta\right)^{3/2}} \tag{26}$$

After this, the algorithm randomly determines whether to keep or destroy the photon during the check stage if its weight drops below a small threshold. With probability `CHANCE`, the photon's weight is boosted by 1/`CHANCE`, allowing it to continue. Otherwise, the photon is terminated. This keeps the simulation statistically impartial while preventing unnecessary computing time consumption from photons with extremely low weight, which have little effect on the outcome. The reflectance has been calculated by the following equation:

$$\text{Reflectance} = \frac{\text{Number of photons detected by the detector}}{\text{Total number of photons emitted by the source}}. \tag{27}$$

At 960 nm, the energy deposition (A) is shown in Figure S2 for two different water concentrations, 5% and 60%. The higher water concentration significantly increases absorption at this wavelength, reflecting water's strong contribution to the overall tissue optical properties in the near-infrared range.

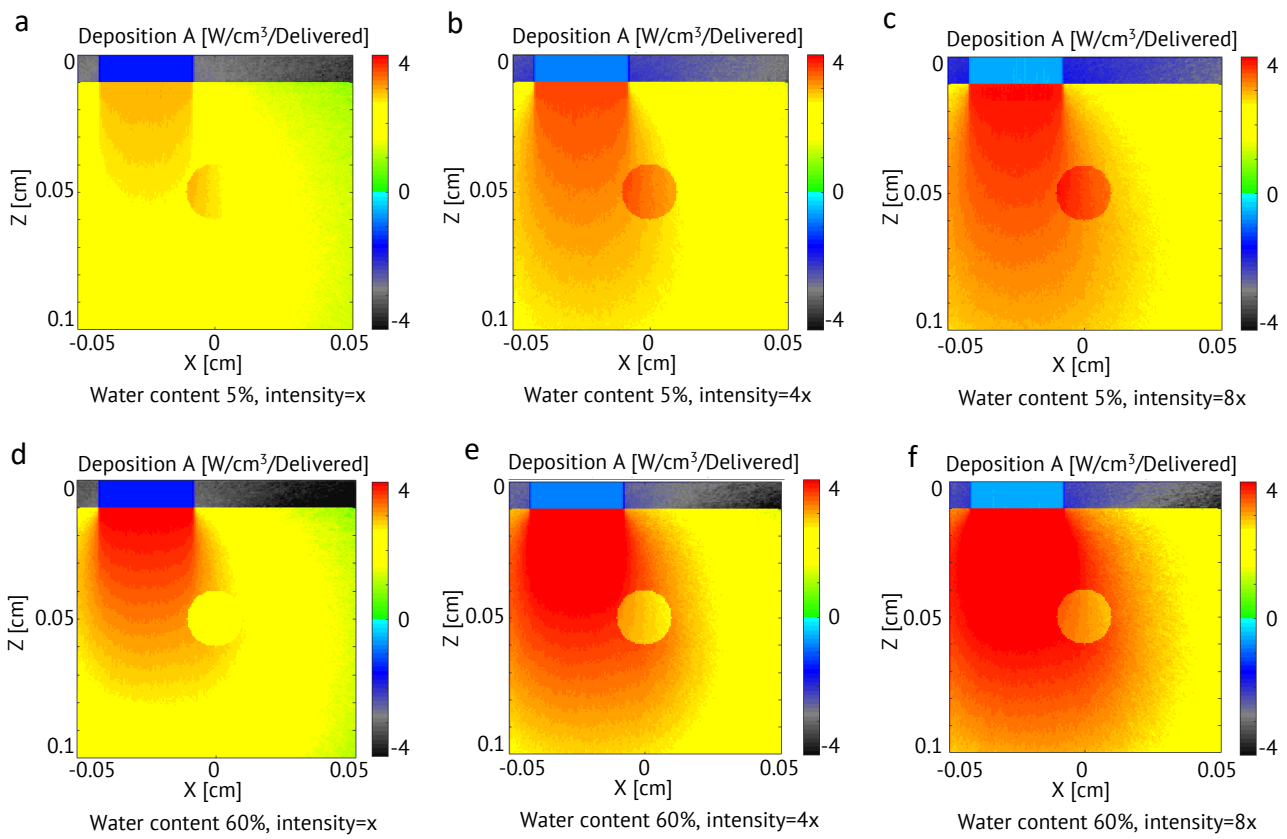


Figure S2. Energy deposition at 960 nm for varying water content and source intensities. Monte Carlo simulation results illustrating the normalized energy deposition (*A*) within the tissue at 960 nm wavelength under two water concentrations: 5% (a–c) and 60% (d–f). The source intensity is progressively increased from *x* (a, d), 4*x* (b, e), to 8*x* (c, f). Higher water concentration (60%) significantly enhances absorption, reflected by a more pronounced energy deposition within the tissue, demonstrating water's dominant optical contribution in the near-infrared range.

.

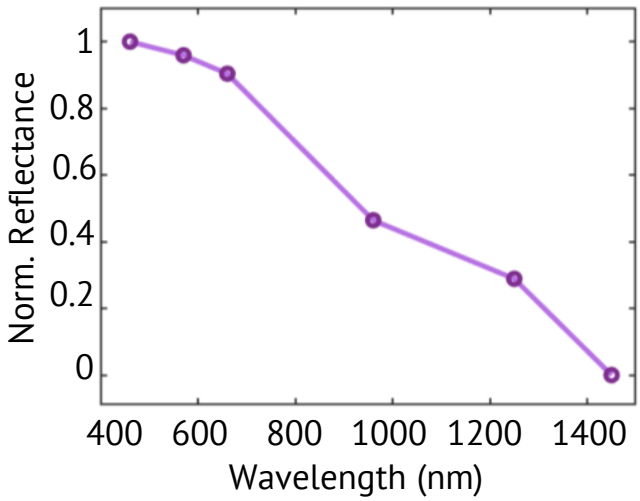


Figure S3. Wavelength dependent normalized reflectance. Simulated reflectance at 460 nm, 570 nm, 660 nm, 960 nm, 1250 nm and 1450 nm at 60% water concentration, showing a decline with increasing wavelength due to higher absorption coefficients, consistent with tissue optical properties.

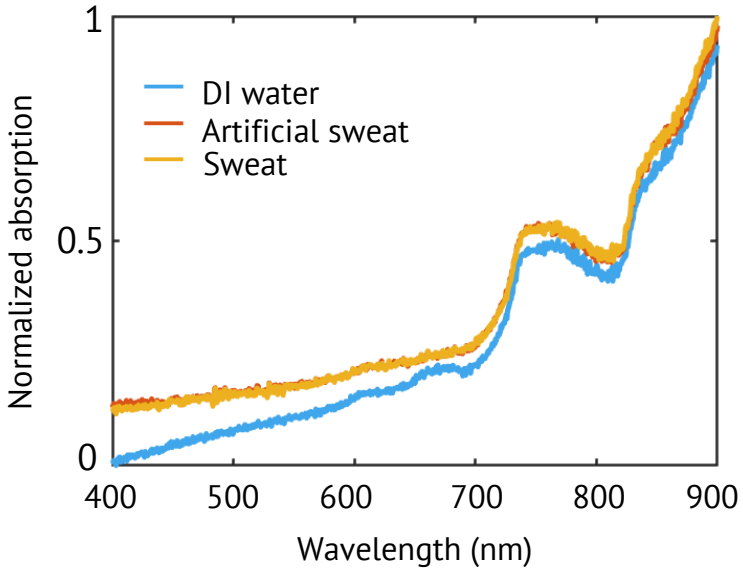


Figure S4. Normalized absorption spectra of different solutions. Absorption profiles of DI water, artificial sweat, and human sweat exhibit similar increasing trends as wavelength increased from 400 nm to 900 nm. This similarity suggests that at higher wavelengths, such as 1500 nm, artificial and human sweat are likely to follow the trend of DI water. However, due to instrumental limitations, absorption beyond 900 nm could not be evaluated in this study.

.

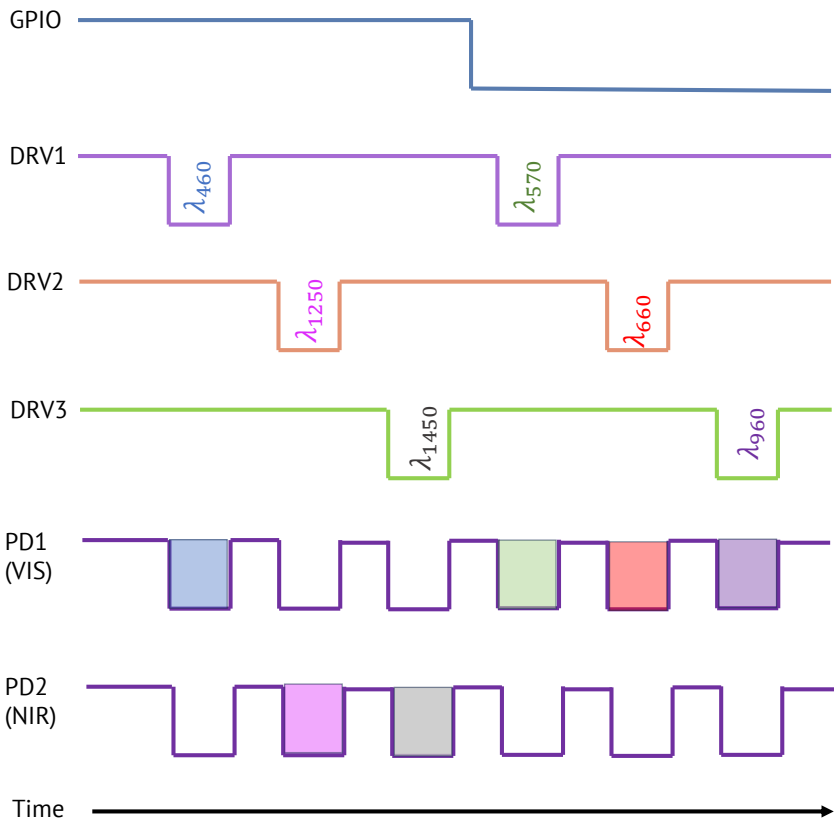


Figure S5. Timing sequence used for data collection from six LEDs. The timing sequence illustrates the GPIO pin controlling a 3x2:1 multiplexer to alternately connect three LEDs (460 nm, 1250 nm, and 1450 nm) or (570 nm, 660 nm, and 960 nm) to the LED drivers. The switching ensures all six wavelengths are sequentially addressed. Photodetectors (PD_1 and PD_2) cover visible (400 nm–1100 nm) and NIR (500 nm–1700 nm) ranges, respectively, collecting photocurrents emitted from the LEDs.

.

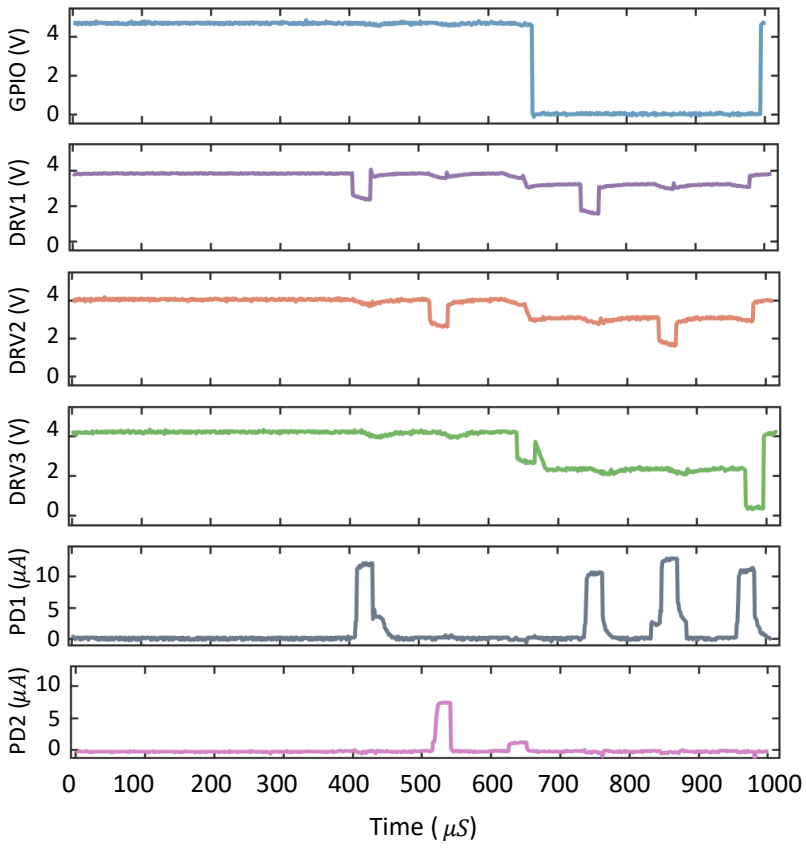


Figure S6. Voltage supplied to LEDs and photocurrent response from photodiodes during experiments. The plots show the supplied voltage to the six LEDs through their respective LED drivers (DRV_1, DRV_2, and DRV_3) controlled by the GPIO pin and the corresponding photocurrent measured from two photodiodes (PD_1 and PD_2). PD_1, sensitive to visible light, and PD_2, sensitive to NIR light, capture reflected signals from the LEDs. The timing sequence aligns with the multiplexer-controlled switching of LEDs, demonstrating synchronized operation and data acquisition.

.

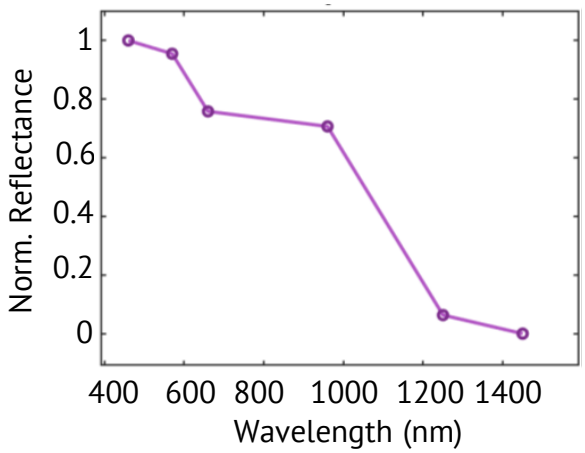


Figure S7. Normalized reflectance across six wavelengths at 60% water concentration. Reflectance measurements were conducted for LEDs emitting light at 460 nm, 570 nm, 660 nm, 960 nm, 1250 nm, and 1450 nm, using a constant water concentration of 60% and an LED current of 20 mA. The normalized reflectance demonstrates a progressive decline with increasing wavelength, consistent with analytical and simulation predictions.

S3 Influence of Skin Pigmentation on the ODA Response

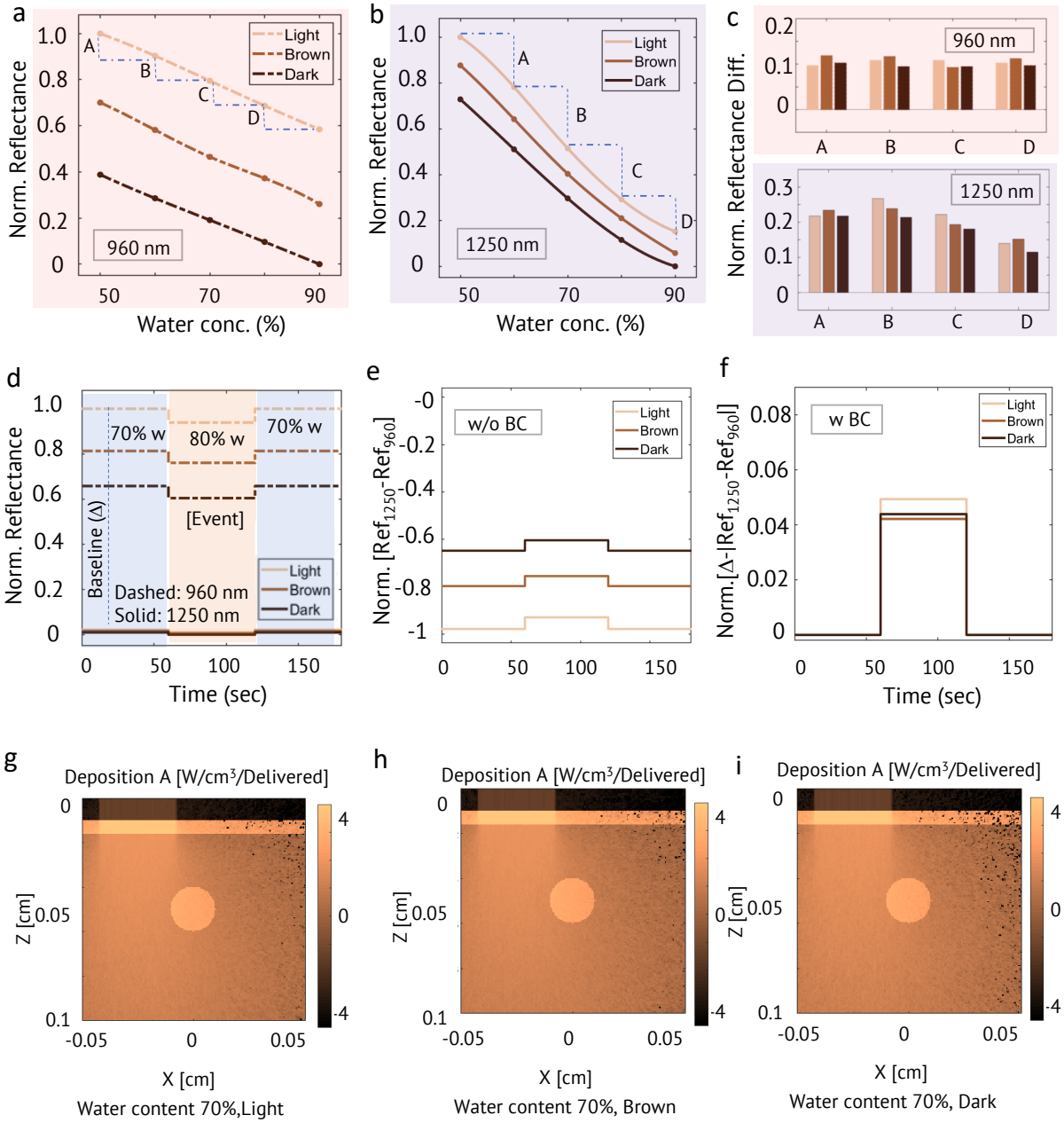


Figure S8. Influence of epidermal pigmentation on the simulated dual-wavelength ODA response. (**a**) Normalized reflectance at 960 nm as tissue water content was varied from 50% to 90% for light, brown, and dark skin conditions. (**b**) Normalized reflectance at 1250 nm as tissue water content was varied from 50% to 90% for light, brown, and dark skin conditions. (**c**) Reflectance changes across consecutive water-content intervals at 960 nm (top) and 1250 nm (bottom), where A, B, C, and D correspond to 50–60%, 60–70%, 70–80%, and 80–90% water-content intervals, respectively. (**d**) Simulated time-dependent reflectance response for a baseline–event–baseline sequence, where tissue water content was maintained at 70% from 0–60 s, increased to 80% from 60–120 s, and returned to 70% from 120–180 s. Dashed and solid lines represent the 960-nm and 1250-nm reflectance signals, respectively. (**e**) Uncorrected differential response, $Ref_{1250} - Ref_{960}$, showing pigmentation-dependent baseline offsets. (**f**) Baseline-corrected ODA response, $|\Delta_0 - |Ref_{1250} - Ref_{960}||$, where Δ_0 is the mean absolute wavelength difference during the initial baseline period. (**g–i**) Energy-deposition maps at 960 nm for light, brown, and dark skin conditions, respectively, at 70% tissue water content.

To investigate the effect of epidermal pigmentation on the ODA measurement, the Monte Carlo tissue model was evaluated using three representative pigmentation conditions. Light, brown, and dark skin were modeled using epidermal melanosome volume fractions of 2.55%, 15.5%, and 30.5%, respectively.[44] Blood oxygen saturation (SpO_2) and epidermal thickness were maintained at 95% and 60 μm, respectively, such that only the melanosome contribution to epidermal absorption was varied.

Figures S8**a** and S8**b** show the simulated normalized reflectance at 960 and 1250 nm, respectively, as tissue water content was

increased from 50% to 90%. At both wavelengths, increasing epidermal pigmentation reduced the absolute reflectance because of the higher melanin-dependent absorption. The pigmentation-dependent baseline shift was more pronounced at 960 nm than at 1250 nm. Despite these differences in absolute reflectance, the changes between consecutive water-content levels remained comparable across the light, brown, and dark skin models. These interval-dependent reflectance changes are summarized in Figure S8**c** for the 50–60% (A), 60–70% (B), 70–80% (C), and 80–90% (D) water-content intervals.

To examine the effect of pigmentation in the time domain, the tissue water content was maintained at 70% during the initial 60 s baseline period, increased to 80% from 60 to 120 s to represent an event-associated change, and returned to 70% during the final 60 s period (Figure S8**d**). Here, the sensing wavelength is defined as $\lambda_1 = 960$ nm and the reference wavelength is defined as $\lambda_2 = 1250$ nm. The detected reflected intensity at the sensing wavelength, $I_{\text{sense}}(t) = I_{\lambda_1}(t)$, exhibited a larger event-associated change, whereas the detected reflected intensity at the reference wavelength, $I_{\text{base}}(t) = I_{\lambda_2}(t)$, showed a comparatively smaller response. However, the signed uncorrected dual-wavelength differential signal,

$$\Delta I_{\text{raw}}(t) = I_{\text{base}}(t) - I_{\text{sense}}(t) = I_{\lambda_2}(t) - I_{\lambda_1}(t), \tag{28}$$

retained a substantial pigmentation-dependent baseline offset, as shown in Figure S8**e**.

To reduce this subject-dependent offset, an individualized baseline correction was applied. The mean detected intensity at each wavelength during the initial 15 s baseline interval was calculated as

$$\bar{I}_{\lambda,0} = \frac{1}{N_0} \sum_{t \in T_0} I_{\lambda}(t), \tag{29}$$

where T_0 represents the initial 15 s baseline interval and N_0 is the number of samples within this interval. The initial dual-wavelength separation was then calculated as

$$\Delta_0 = \left| \bar{I}_{\lambda_2,0} - \bar{I}_{\lambda_1,0} \right|. \tag{30}$$

The baseline-corrected ODA signal was defined as

$$\text{ODA}(t) = \left| \Delta_0 - \left| I_{\text{base}}(t) - I_{\text{sense}}(t) \right| \right| = \left| \Delta_0 - \left| I_{\lambda_2}(t) - I_{\lambda_1}(t) \right| \right|. \tag{31}$$

As shown in Figure S8**f**, this correction aligned the initial responses near zero and preserved a similar magnitude of the event-associated ODA response across the light, brown, and dark skin models. The corresponding energy-deposition maps at 960 nm further illustrate the influence of melanin-dependent epidermal absorption on light propagation within the tissue for the three modeled skin conditions (Figures S8**g–i**).

These simulations indicate that epidermal pigmentation primarily introduces a skin-tone-dependent shift in the absolute reflectance and the uncorrected dual-wavelength baseline. Despite this baseline variation, the relative ODA response to the modeled change in tissue water content remained detectable across the light, brown, and dark skin models. Individualized baseline correction aligned the responses near a common reference while preserving the event-associated ODA change, demonstrating its potential to compensate for pigmentation-dependent baseline offsets and support consistent ODA extraction across the evaluated skin-tone range.

S4 Influence of Blood Oxygen Saturation on the ODA Response

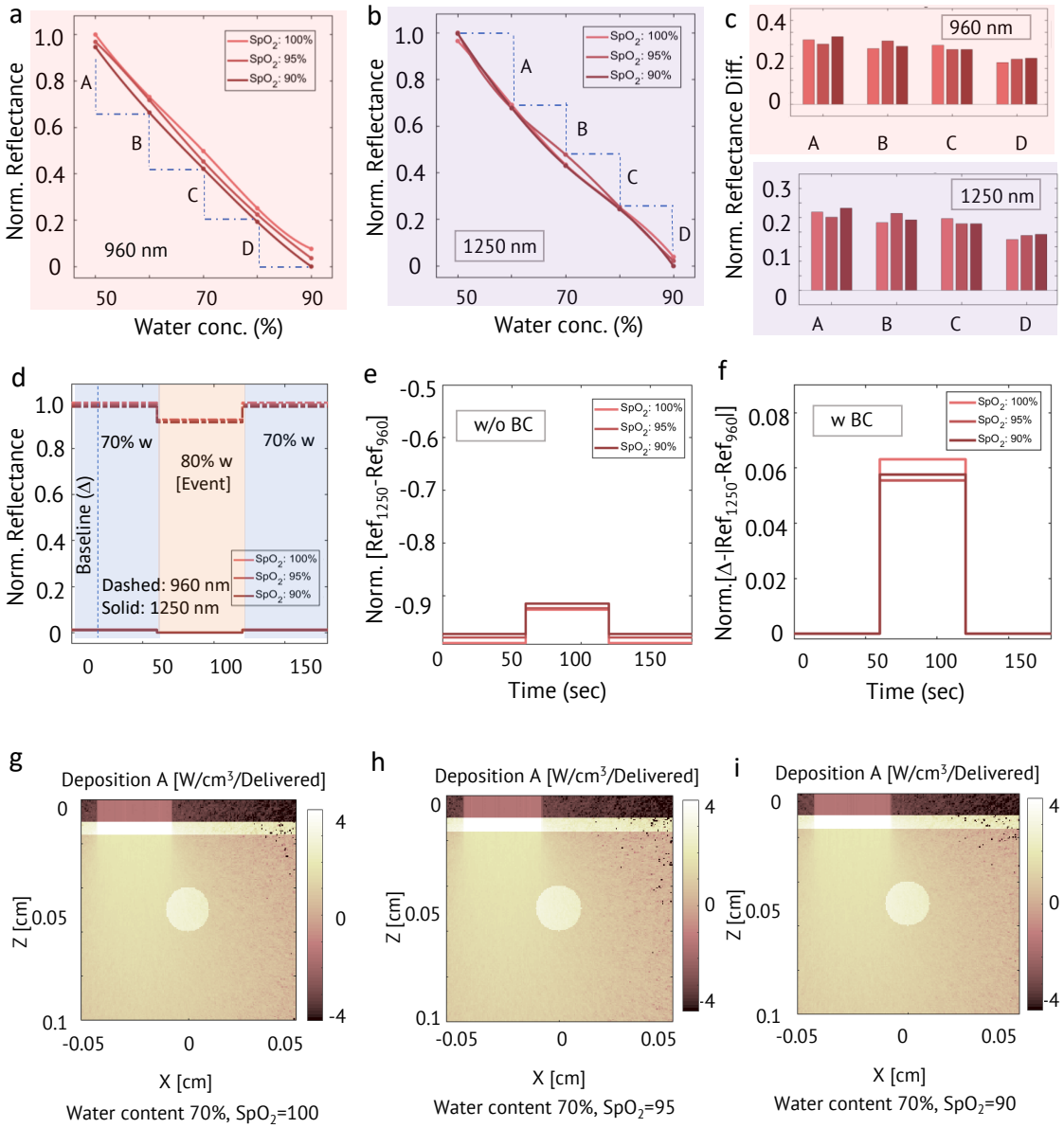


Figure S9. Influence of blood oxygen saturation on the simulated dual-wavelength ODA response. Monte Carlo simulations were performed using the brown skin model with an epidermal thickness of 60 μm at blood oxygen saturation (SpO_2) levels of 100%, 95%, and 90%. (**a**) Normalized reflectance at 960 nm as tissue water content was varied from 50% to 90% for the three modeled SpO_2 levels. (**b**) Normalized reflectance at 1250 nm as tissue water content was varied from 50% to 90%. (**c**) Reflectance changes across consecutive water-content intervals at 960 nm (top) and 1250 nm (bottom), where A, B, C, and D correspond to the 50–60%, 60–70%, 70–80%, and 80–90% intervals, respectively. (**d**) Simulated time-dependent reflectance during a baseline–event–baseline sequence, where tissue water content was maintained at 70% from 0–60 s, increased to 80% from 60–120 s, and returned to 70% from 120–180 s. Dashed and solid lines represent the 960- and 1250-nm reflectance signals, respectively. (**e**) Signed uncorrected dual-wavelength differential signal, $\Delta R_{raw}(t) = R_{1250}(t) - R_{960}(t)$, showing the small baseline offsets associated with the modeled SpO_2 levels. (**f**) Baseline-corrected ODA response obtained using the mean reflectance values from the initial 15-s resting interval. (**g–i**) Energy-deposition maps at 960 nm for SpO_2 levels of 100%, 95%, and 90%, respectively, at 70% tissue water content.

To examine the influence of blood oxygen saturation on the ODA measurement, the Monte Carlo tissue model was evaluated at SpO_2 levels of 100%, 95%, and 90%. The skin pigmentation and anatomical geometry were held constant using the brown skin model and an epidermal thickness of 60 μm, such that only the relative contributions of oxygenated and deoxygenated hemoglobin were varied.

Figures S9**a** and S9**b** show the normalized reflectance at 960 and 1250 nm, respectively, as tissue water content was increased from 50% to 90%. Across the modeled SpO_2 range, only small shifts in absolute reflectance were observed at both wavelengths. This limited variation is consistent with the comparatively similar optical absorption of oxygenated and deoxygenated hemoglobin within the selected near-infrared

wavelength range.

Despite the small differences in absolute reflectance, the changes between consecutive water-content levels remained comparable across the three SpO_2 conditions. Figure S9**c** summarizes these reflectance changes for the 50–60% (A), 60–70% (B), 70–80% (C), and 80–90% (D) water-content intervals at both wavelengths. The similarity of these interval-dependent changes indicates that the modeled variation in blood oxygen saturation had only a limited effect on the water-content-dependent optical response.

The influence of SpO_2 was further evaluated in the time domain using the same baseline–event–baseline sequence applied in the pigmentation analysis. Tissue water content was maintained at 70% during the initial 60 s baseline period, increased to 80% from 60 to 120 s, and returned to 70% during the final 60 s period (Figure S9**d**). The event-associated reflectance changes remained similar for the three modeled SpO_2 levels.

The signed uncorrected dual-wavelength differential signal was calculated according to Equation 9 and exhibited only small SpO_2-dependent baseline offsets (Figure S9**e**). The individualized baseline-correction procedure defined in Equations 10–12 was then applied using the initial 15 s resting interval. As shown in Figure S9**f**, baseline correction aligned the responses near a common reference while preserving the event-associated ODA change across the modeled oxygen-saturation conditions.

The corresponding energy-deposition maps at 960 nm are presented in Figures S9**g–i** for SpO_2 levels of 100%, 95%, and 90%, respectively. The similar spatial distributions further illustrate the limited influence of the modeled oxygen-saturation variation on light propagation under otherwise identical tissue conditions.

Overall, the simulations indicate that changes in SpO_2 between 90% and 100% introduce only modest variations in the absolute reflectance within the selected near-infrared wavelength range. The water-content-dependent response remained comparable across the evaluated conditions, while individualized baseline correction further reduced the small initial offsets and supported consistent extraction of the event-associated ODA response.

S5 Influence of Epidermal Thickness on the ODA Response

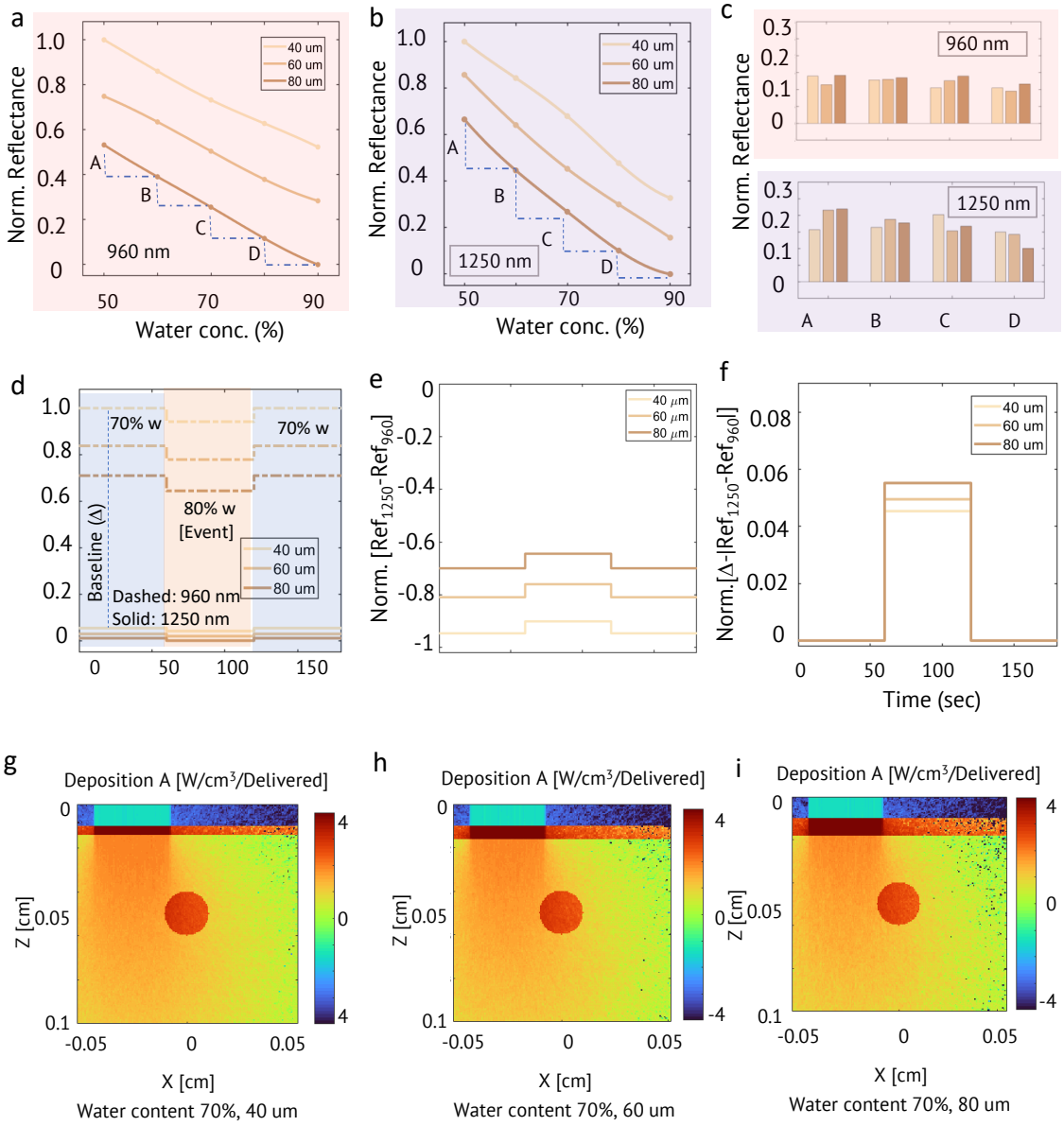


Figure S10. Influence of epidermal thickness on the simulated dual-wavelength ODA response. Monte Carlo simulations were performed using the brown skin model at a blood oxygen saturation (SpO_2) of 95%, while the epidermal thickness was varied among 40, 60, and 80 μm. (**a**) Normalized reflectance at 960 nm as tissue water content was varied from 50% to 90% for the three modeled epidermal thicknesses. (**b**) Normalized reflectance at 1250 nm as tissue water content was varied from 50% to 90%. (**c**) Reflectance changes across consecutive water-content intervals at 960 nm (top) and 1250 nm (bottom), where A, B, C, and D correspond to the 50–60%, 60–70%, 70–80%, and 80–90% intervals, respectively. (**d**) Simulated time-dependent reflectance during a baseline–event–baseline sequence, where tissue water content was maintained at 70% from 0–60 s, increased to 80% from 60–120 s, and returned to 70% from 120–180 s. Dashed and solid lines represent the 960 nm and 1250 nm reflectance signals, respectively. (**e**) Signed uncorrected dual-wavelength differential signal, $\Delta R_{raw}(t) = R_{1250}(t) - R_{960}(t)$, showing epidermal-thickness-dependent baseline offsets. (**f**) Baseline-corrected ODA response obtained using the mean reflectance values from the initial 15 s resting interval. (**g–i**) Energy-deposition maps at 960 nm for epidermal thicknesses of 40, 60, and 80 μm, respectively, at 70% tissue water content, 95% SpO_2, and brown skin pigmentation.

To examine the influence of anatomical variation on the ODA measurement, the epidermal thickness in the Monte Carlo tissue model was varied among 40, 60, and 80 μm. Skin pigmentation and blood oxygen saturation were maintained using the brown skin model and an SpO_2 value of 95%, respectively, such that the effect of epidermal thickness could be evaluated independently.

Figures S10**a** and S10**b** show the normalized reflectance at 960 nm and 1250 nm, respectively, as tissue water content was increased from 50% to 90%. Changes in epidermal thickness altered the absolute reflectance at both wavelengths because of the corresponding variation in the optical path through the epidermal layer. However, the reflectance curves exhibited similar water-content-dependent trends across

the three modeled thicknesses.

The changes between consecutive water-content levels are summarized in Figure S10**c** for the 50–60% (A), 60–70% (B), 70–80% (C), and 80–90% (D) intervals. Although the absolute reflectance baselines differed, the interval-dependent changes remained comparable across the 40 μm , 60 μm, and 80 μm epidermal models at both wavelengths.

The effect of epidermal thickness was further evaluated in the time domain using a baseline–event–baseline sequence. Tissue water content was maintained at 70% during the initial 60 s baseline period, increased to 80% from 60 s to 120 s, and returned to 70% during the final 60 s period (Figure S10**d**). Similar event-associated reflectance changes were observed for the three modeled epidermal thicknesses.

The signed uncorrected dual-wavelength signal, calculated according to Equation 9, retained an epidermal-thickness-dependent baseline offset (Figure S10**e**). The individualized baseline-correction procedure defined in Equations 10–12 was subsequently applied using the initial 15 s resting interval. As shown in Figure S10**f**, the corrected responses were aligned near a common baseline, while the event-associated ODA changes remained within a comparable range across the modeled epidermal thicknesses.

Figures S10**g–i** present the corresponding energy-deposition maps at 960 nm for epidermal thicknesses of 40 μm, 60 μm, and 80 μm, respectively. These simulations indicate that epidermal thickness influences the absolute optical reflectance and initial dual-wavelength separation; however, the water-content-dependent response remains detectable across the evaluated range. Individualized baseline correction provides a practical approach for compensating the anatomical baseline offset while preserving the event-associated ODA response.

.

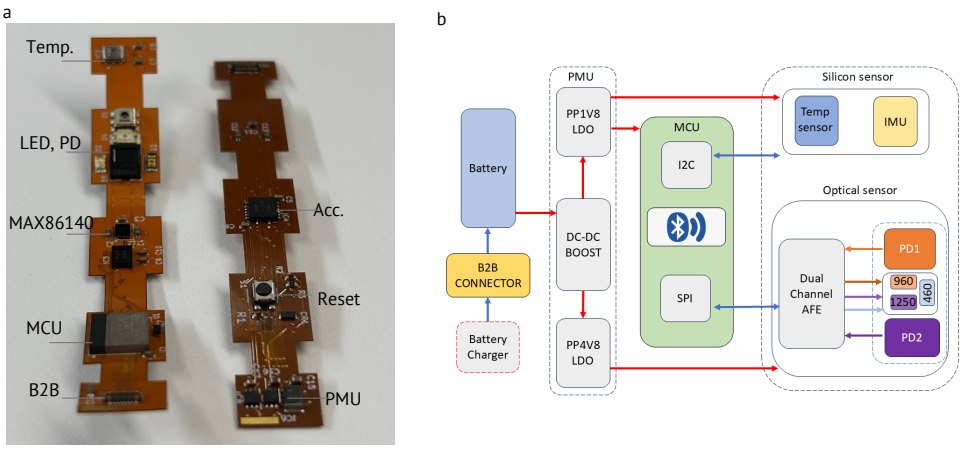


Figure S11. Development and system-level architecture of the ODA ring sensor. (a) Flexible four-layer PCB with key components: status LED (460nm), sensing LEDs (960nm, 1250nm), dual photodiodes, MAX86140 AFE, nRF52832 MCU, B2B connector, and temperature (HS3003) and motion (BMI270) sensors. (b) System block diagram showing power from a flexible arc Li-ion battery via a PMU with LDOs and a DC-DC boost converter. The MCU communicates with sensors via I2C/SPI. The AFE controls LEDs and photodiodes for ODA sensing. Mode-1 transmits raw data; Mode-2 enables on-device ML inference.

.

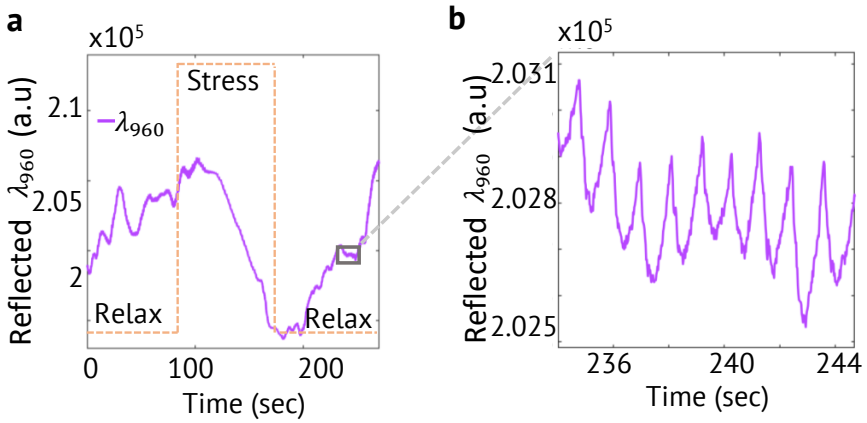


Figure S12. PPG signal captured during the stress-relaxation protocol using the ODA ring sensor. (a) Reflected signal from the 960 nm LED during the experimental protocol, illustrating transitions between relaxation and stress phases. The decline in signal during the stress phase corresponds to increased sympathetic sweating and light absorption by activated sweat glands. The signal returns to baseline during the relaxation phase, effectively capturing physiological transitions. (b) Zoomed-in view of the reflected signal, showing PPG characteristics, including distinct pulsations. This optical signal enables the extraction of additional physiological markers such as pulse amplitude and heart rate and their variabilities, further enhancing the ODA ring's stress detection capability.

.

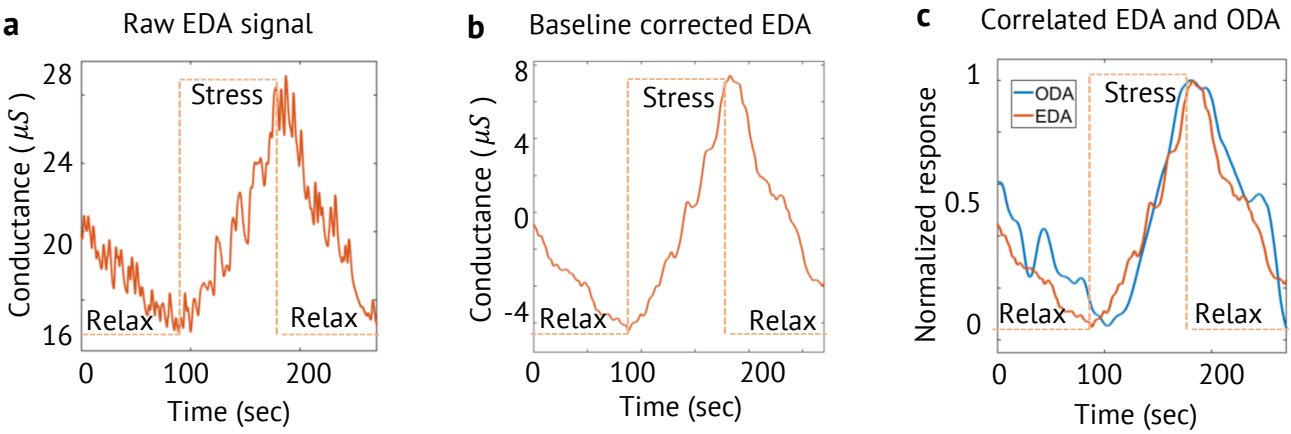


Figure S13. Comparison of EDA and ODA signals during the stress-relaxation protocol. (a) Raw EDA signal recorded from the palm of participants, showing increased skin conductance during the stress phase due to sympathetic nervous system activation. (b) Baseline-corrected and filtered EDA signal, highlighting the distinct changes in conductance during the transition between relaxation and stress phases. (c) Correlation between normalized ODA and EDA signals, showcasing the synchronized response during the stress phase and the return to baseline during relaxation phases. This comparison demonstrates the capability of the ODA ring sensor to effectively monitor stress-related physiological changes.

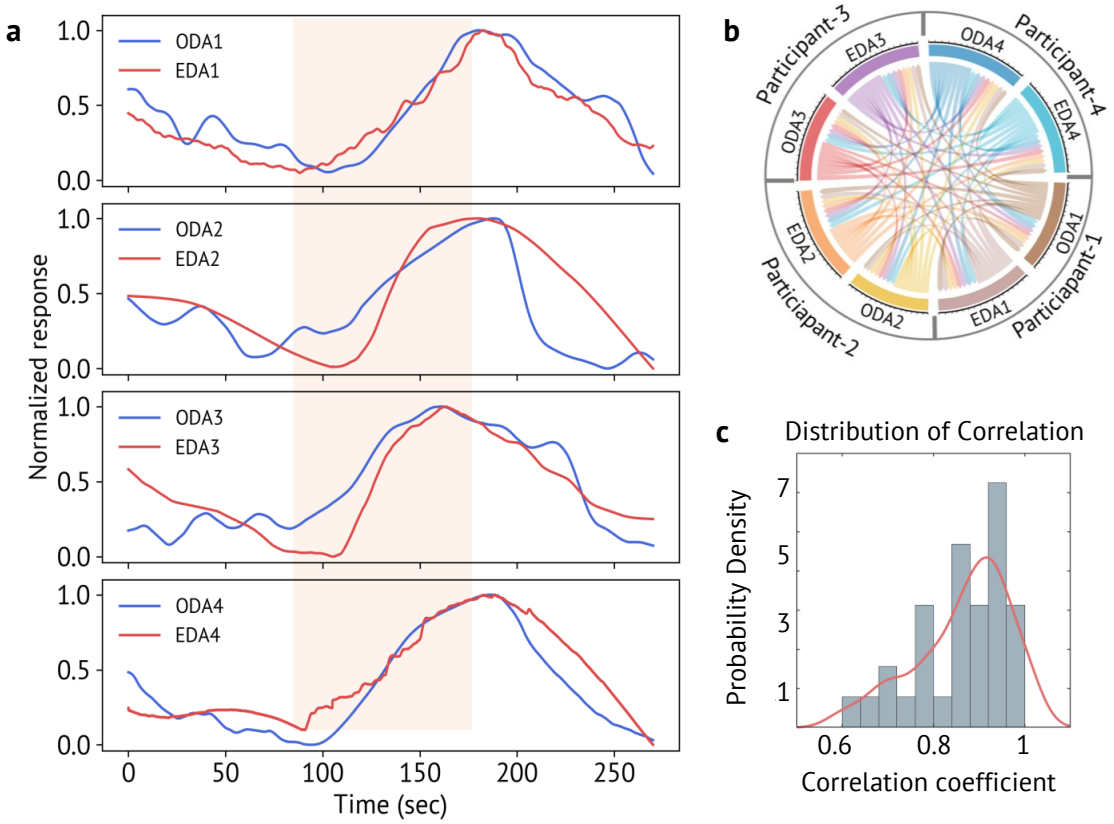


Figure S14. Agreement between ODA and EDA responses across participants. (**a**) Normalized ODA and EDA signals from four participants during the relaxation–stress–recovery protocol, showing consistent temporal responses. (**b**) Chord diagram showing participant-specific ODA–EDA correlations ranging from 72% to 94%, with an average correlation of 86%. (**c**) Distribution of the correlation coefficients, demonstrating strong agreement between ODA and EDA in tracking stress-associated sweat-gland activity.

S6 Cross-Pigmentation Validation of ODA with EDA and Salivary Biomarkers

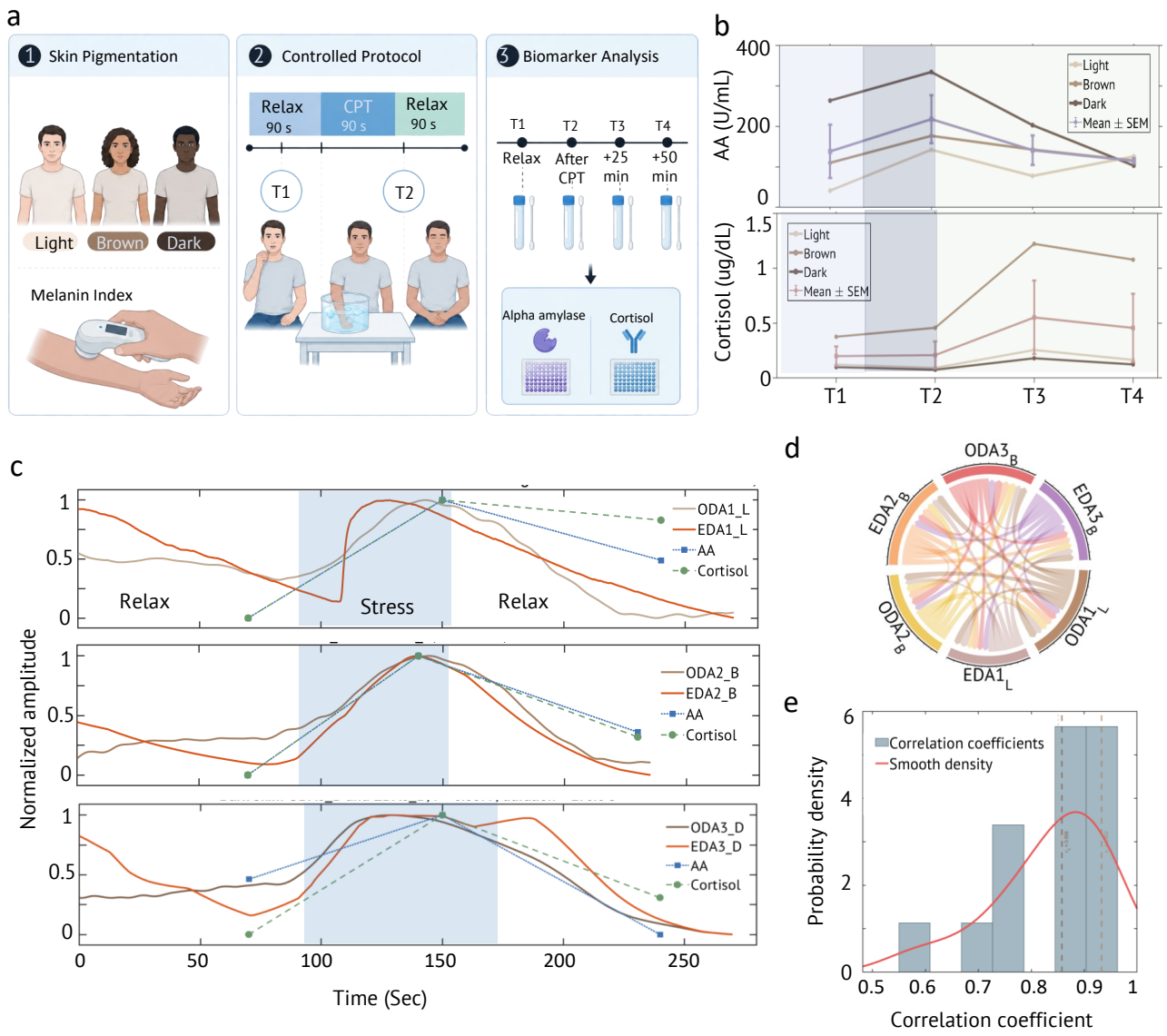


Figure S15. Cross-pigmentation validation of ODA using EDA and salivary stress biomarkers. (**a**) Skin-pigmentation assessment, controlled relaxation–CPT–recovery protocol, saliva-sampling timeline, and biomarker analysis. (**b**) Salivary alpha-amylase and cortisol concentrations at four sampling time points. (**c**) Normalized ODA, EDA, alpha-amylase, and cortisol responses for participants with light, brown, and dark skin pigmentation. (**d**) Pairwise correlations among the ODA and EDA responses. (**e**) Distribution of ODA–EDA correlation coefficients.

Three participants representing light, brown, and dark skin pigmentation were evaluated to experimentally validate the ODA response across different skin optical properties. Skin pigmentation was categorized using the Google Monk Skin Tone scale and independently quantified using a Delfin SkinColorCatch sensor. Device-derived melanin-index values below 600, between 600 and 800, and above 800 were categorized as light, brown, and dark skin pigmentation, respectively.

Each participant completed a controlled protocol consisting of an initial relaxation period, a cold pressor test (CPT), and a subsequent recovery period while ODA and EDA signals were recorded simultaneously. Saliva samples were collected at four time points: T1 during the initial relaxation period, T2 immediately following the CPT, T3 at 25 min after the CPT, and T4 at 50 min after the CPT. The samples were frozen after collection and subsequently analyzed for salivary alpha-amylase and cortisol.

As shown in Figure S15**b**, alpha-amylase exhibited a rapid stress-associated response immediately following the CPT, followed by a reduction during recovery. Cortisol exhibited the expected delayed response, increasing at T3 and subsequently decreasing toward the resting level at T4. Accordingly, T1, T2, and T3 were used to represent the relaxation, stress, and recovery responses for alpha-amylase, whereas T1, T3, and T4 were used for the corresponding cortisol comparison.

Figure S15**c** presents the normalized ODA and EDA time-series responses together with representative alpha-amylase and cortisol measurements. For participants with light, brown, and dark skin pigmentation, the ODA and EDA signals exhibited comparable stress-associated temporal trends. Both signals increased during the CPT-associated response and subsequently decreased during recovery. The salivary biomarkers followed the same overall physiological progression, with alpha-amylase capturing the rapid sympathetic response and cortisol capturing the delayed endocrine response.

Participant matched ODA and EDA correlations were $r = 0.851$, $r = 0.933$, and $r = 0.858$ for the light, brown, and dark skin participants, respectively, corresponding to a mean matched correlation of $r = 0.880$ and a range of 0.851–0.933. The chord diagram in Figure S15**d** summarizes the pairwise relationships among the three ODA and three EDA signals. Across all 15 unique pairwise comparisons, the mean correlation was $r = 0.837$, with values ranging from 0.581 to 0.962, as summarized in Figure S15**e**.

These results demonstrate consistent agreement between ODA, EDA, and salivary stress biomarkers across the evaluated pigmentation categories. The strong participant-matched ODA–EDA correlations further support the simulation results presented in Section 2.4: although skin pigmentation can alter the initial optical baseline, wearer-specific baseline correction preserves the relative stress-associated ODA response across different pigmentation levels.

S7 ECG Validation of PPG Derived Cardiovascular Metrics

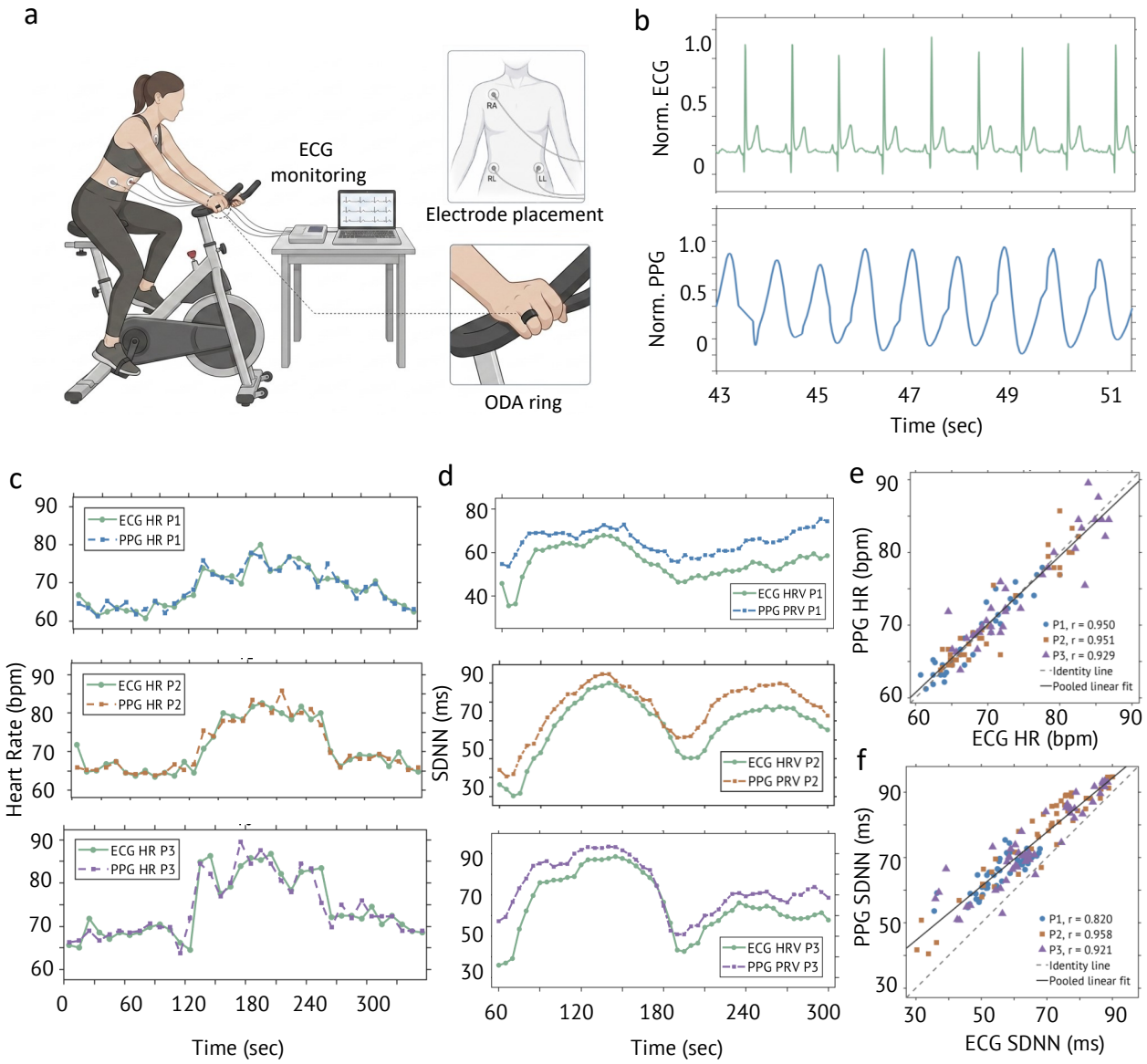


Figure S16. Validation of ODA ring's PPG against ECG derived cardiovascular metrics. (**a**) Experimental setup for simultaneous ECG and ODA-ring PPG recording during a rest–cycling–recovery protocol, with ECG electrodes positioned at the right upper chest (RA), lower right abdomen (RL), and lower left abdomen (LL). (**b**) Representative normalized ECG and PPG waveforms over the same time interval. (**c**) ECG and PPG derived heart rate responses for three participants during the protocol. (**d**) ECG derived heart rate variability and PPG derived pulse rate variability, quantified using SDNN. (**e**) Correlation between ECG and PPG derived heart rate for the three participants. (**f**) Correlation between ECG and PPG derived SDNN values.

To evaluate PPG as a practical alternative to ECG for extracting cardiovascular features, simultaneous ECG and ODA ring's PPG measurements were collected from three participants. ECG signals were acquired using three electrodes positioned on the right upper chest, lower right abdomen, and lower left abdomen, while the optical signal was recorded concurrently from the ring. Each participant completed a 6-min protocol consisting of 2 min of seated rest, 2 min of stationary cycling to induce a heart-rate change, and 2 min of post-exercise recovery.

Figure S16**b** presents representative ECG and PPG waveforms over the same time interval. Distinct ECG R-peaks and corresponding PPG pulse cycles were clearly resolved, enabling independent extraction of beat-to-beat cardiovascular information from both modalities.

The heart-rate responses derived from ECG and PPG are compared in Figure S16**c**. Across all three participants, both modalities captured the increase in heart rate during cycling and the subsequent decrease during recovery, demonstrating close temporal agreement throughout the protocol.

Beat to beat variability was evaluated using the standard deviation of normal to normal intervals (SDNN), a time-domain measure

of variability in consecutive cardiac intervals. For ECG, SDNN was calculated from normal R–R intervals and represents heart-rate variability. For PPG, the corresponding SDNN was calculated from pulse to pulse intervals and represents pulse-rate variability. As shown in Figure S16**d**, ECG and PPG derived SDNN followed similar temporal trends across the rest, cycling, and recovery periods.

The correlation analysis further demonstrated strong agreement between the two modalities. ECG- and PPG-derived heart rate produced correlation coefficients of $r = 0.950$, $r = 0.951$, and $r = 0.929$ for participants P1, P2, and P3, respectively (Figure S16**e**). Similarly, ECG and PPG derived SDNN values showed correlations of $r = 0.820$, $r = 0.958$, and $r = 0.921$, respectively (Figure S16**f**). The measurements also clustered near the identity line, further supporting agreement between the ECG and PPG derived metrics.

These results demonstrate that PPG acquired from the optical channel of the ODA ring provides heart-rate and beat to beat variability information that closely follows the corresponding ECG derived responses. Therefore, the ODA ring can combine dermal activity sensing with PPG derived cardiovascular features as a compact alternative to adding a separate electrode based ECG system, preserving the ring form factor while supporting reliable multimodal physiological monitoring.

S8 Environmental Robustness of the ODA Ring

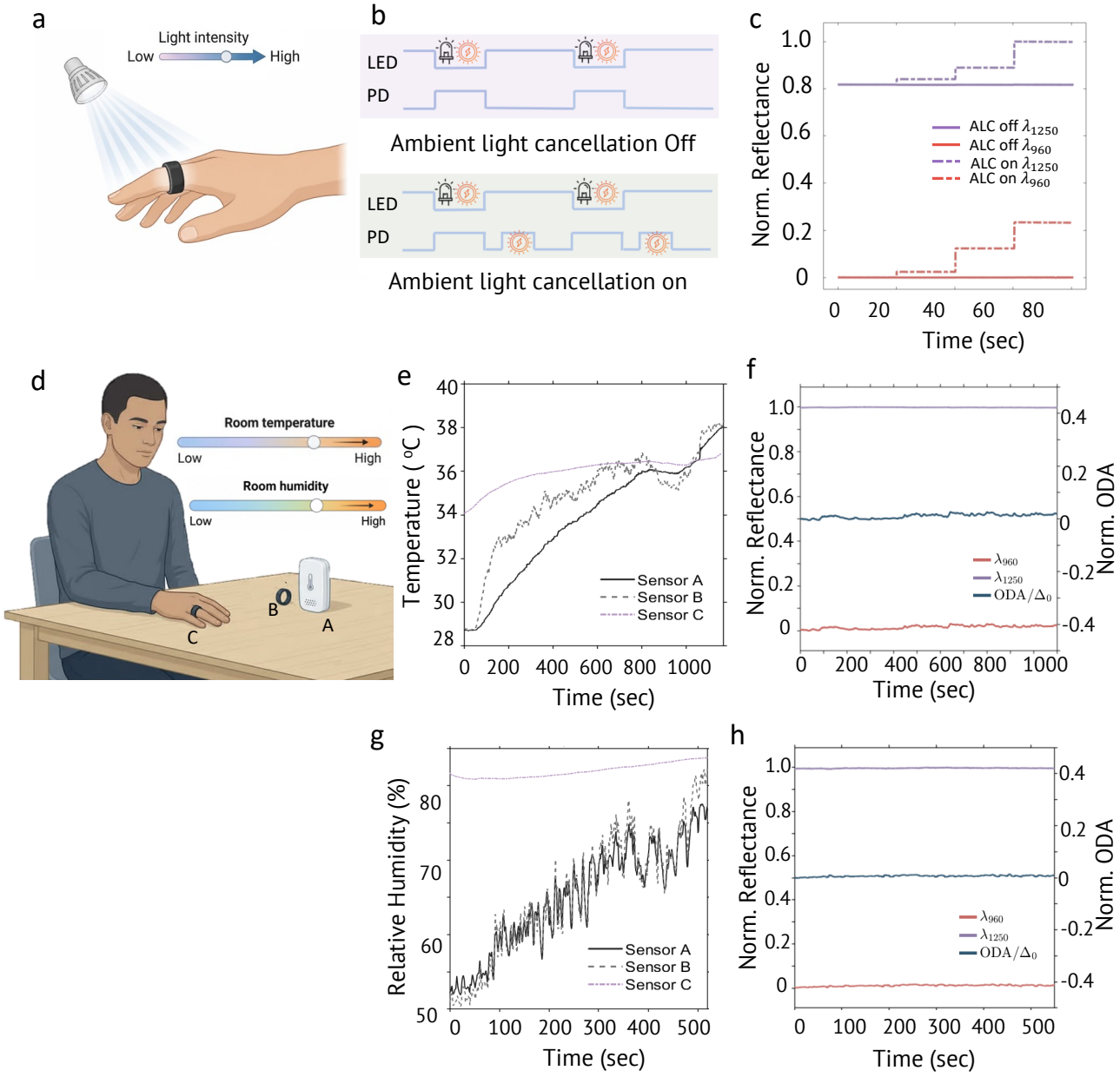


Figure S17. Environmental robustness of the ODA ring under variations in ambient light, temperature, and humidity. (**a**) Experimental setup for varying ambient light intensity around the worn ring. (**b**) Operating principle of ambient light cancellation (ALC) with the function disabled and enabled. (**c**) Normalized 960 and 1250 nm reflectance under varying ambient illumination, showing effective suppression of light interference when ALC is enabled. (**d**) Experimental arrangement for controlled temperature and humidity variation, including a commercial reference sensor (A), a ring placed on the table (B), and a ring worn on the finger (C). (**e**) Temperature recorded by the three sensors during room-temperature variation. (**f**) Corresponding 960 nm, 1250 nm, and baseline corrected ODA responses. (**g**) Relative humidity recorded by the three sensors during room humidity variation. (**h**) Corresponding optical and ODA responses during the humidity experiment.

The environmental robustness of the ODA ring was evaluated under controlled variations in ambient illumination, room temperature, and relative humidity. These experiments examined whether environmental changes produced measurable interference in the reflected optical signals or the baseline corrected ODA response.

For the ambient light experiment, the illumination directed toward the worn ring was varied while the optical sensor was operated with ambient light cancellation (ALC) disabled and enabled (Figure S17**a**). With ALC disabled, the photodetector samples only during LED illumination, and the measured signal contains both reflected LED light and ambient light:

$$I_{\text{measured}} = I_{\text{LED}} + I_{\text{ambient}}. \tag{32}$$

With ALC enabled, an additional LED-off sample is acquired and internally subtracted from the LED-on measurement:

$$I_{\text{ALC}} = I_{\text{on}} - I_{\text{off}} \approx I_{\text{LED}}. \tag{33}$$

As shown in Figure S17**c**, changing the ambient light intensity altered the measured reflectance when ALC was disabled. In contrast, the 960 and 1250 nm signals remained nearly unchanged when ALC was enabled. ALC was therefore enabled during all ODA experiments reported in this work.

Temperature and humidity experiments were performed in a controlled 3 ft × 4 ft × 10 ft room. Sensor A was a commercial environmental reference sensor, Sensor B was an ODA ring placed on the table, and Sensor C was an ODA ring worn on the participant's finger (Figure S17**d**).

For the temperature experiment, two portable heaters increased the room temperature from approximately 28 to 38 °C. Sensors A and B recorded similar temperature increases, whereas Sensor C exhibited a smaller and slower change because it was enclosed within the ring casing and thermally coupled to the finger (Figure S17**e**). During this variation, the 960 nm and 1250 nm reflectance signals and the baseline corrected ODA response remained stable (Figure S17**f**).

The HS300x environmental sensor used for temperature measurement also provides relative-humidity sensing. During the humidity experiment, this capability was used to determine the humidity variation experienced by the ring near the skin as the room humidity changed. For the humidity experiment, two portable humidifiers increased the room relative humidity from approximately 50% to 80%. Sensors A and B followed similar humidity trends, while the change measured by the worn ring was substantially smaller because of the enclosed ring casing and limited direct exposure of the skin–sensor interface (Figure S17**g**). No substantial variation was observed in the corresponding optical signals or ODA response (Figure S17**h**).

Collectively, these results demonstrate that ALC effectively suppresses ambient light interference and that the ODA response remains stable across the evaluated temperature and humidity ranges. These findings support the environmental robustness of the ODA ring under the tested conditions.

S9 Stress Tolerance and Daily Use Stability of the ODA Ring

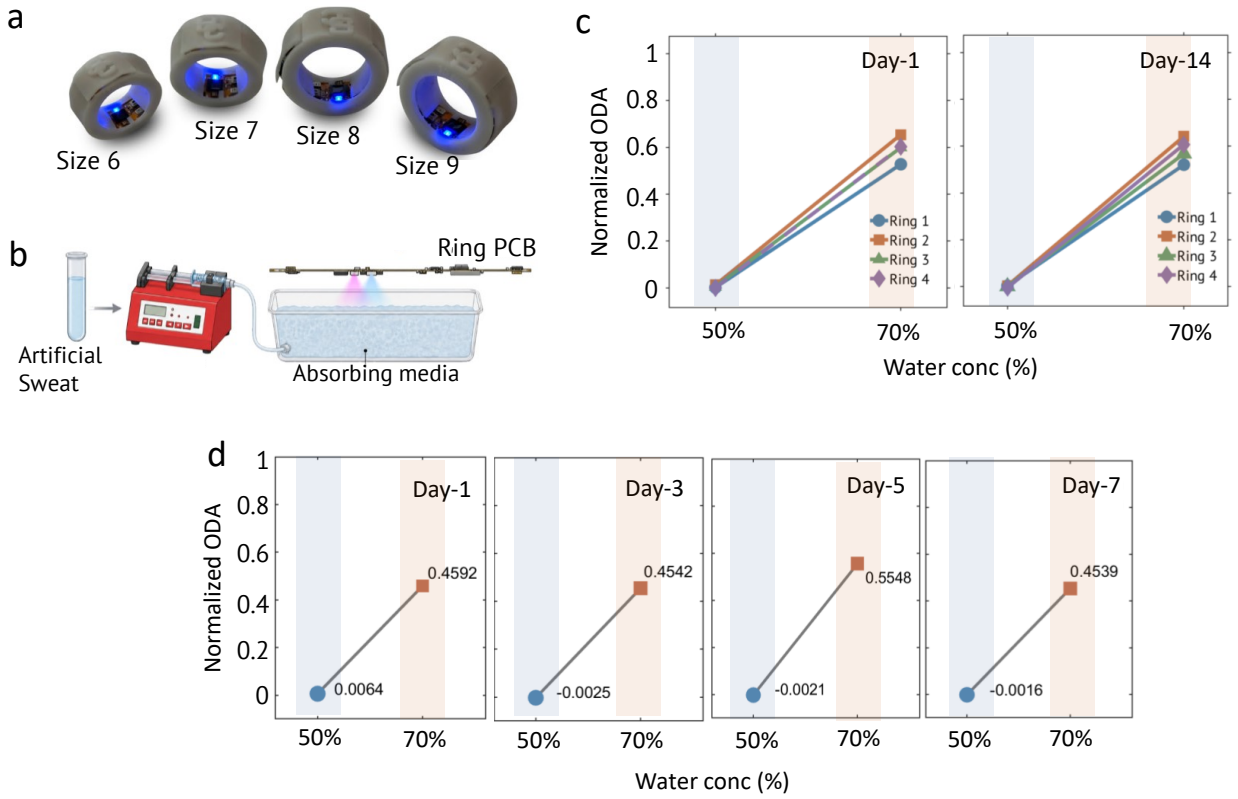


Figure S18. Mechanical and repeated wear robustness of the ODA ring. (**a**) ODA rings assembled in sizes 6, 7, 8, and 9, corresponding to inner diameters of 16.5, 17.3, 18.1, and 18.9 mm, respectively. (**b**) Experimental setup used to evaluate the ODA response of the flexible PCBs using artificial sweat delivered to an absorbing medium. (**c**) Normalized ODA responses of four PCBs at 50% and 70% water concentrations before ring assembly on day 1 and after 14 days in the assembled configuration. (**d**) Normalized ODA responses measured on days 1, 3, 5, and 7 after repeated 6 h daily wear.

The mechanical robustness of the flexible ODA PCB was evaluated by assembling four devices into ring sizes 6, 7, 8, and 9, with inner diameters of 16.5, 17.3, 18.1, and 18.9 mm, respectively (Figure S18**a**). Because the same PCB design was conformed to different ring diameters, the devices experienced different bending radii and levels of assembly induced mechanical deformation.

Before assembly, each PCB was placed flat above the absorbing medium and evaluated using the artificial-sweat setup shown in Figure S18**b**, following the same measurement principle used for the experimental optimization in Figure 2f. The absorbing medium was tested at 50% and 70% water concentrations, and the corresponding ODA response was recorded for each PCB.

The four PCBs were then assembled into their respective ring housings and maintained in the curved configuration for 14 days. After this period, the devices were disassembled and retested under the same experimental conditions. As shown in Figure S18**c**, all four devices produced comparable normalized ODA changes between the 50% and 70% water-concentration conditions on day 1 and day 14. The preserved responses across the four ring diameters indicate that the mechanical deformation associated with assembly did not appreciably affect ODA sensing performance over the evaluated period.

Repeated wear stability was evaluated separately to examine the influence of routine skin contact, including exposure to skin oils and perspiration. A participant wore the ring for 6 h per day, and the device was evaluated using the same artificial sweat setup after wear on days 1, 3, 5, and 7. As shown in Figure S18**d**, the baseline corrected response remained near zero at 50% water concentration, while the response to 70% water concentration remained comparable across the four measurement days.

Together, these results demonstrate that the ODA response is preserved across different ring curvatures and after repeated daily wear. The consistent response following prolonged PCB bending and routine skin exposure supports the mechanical and operational robustness of the ODA ring under the evaluated day-to-day use conditions.

S10 Motion Robustness and Artifact Detection of the ODA Ring

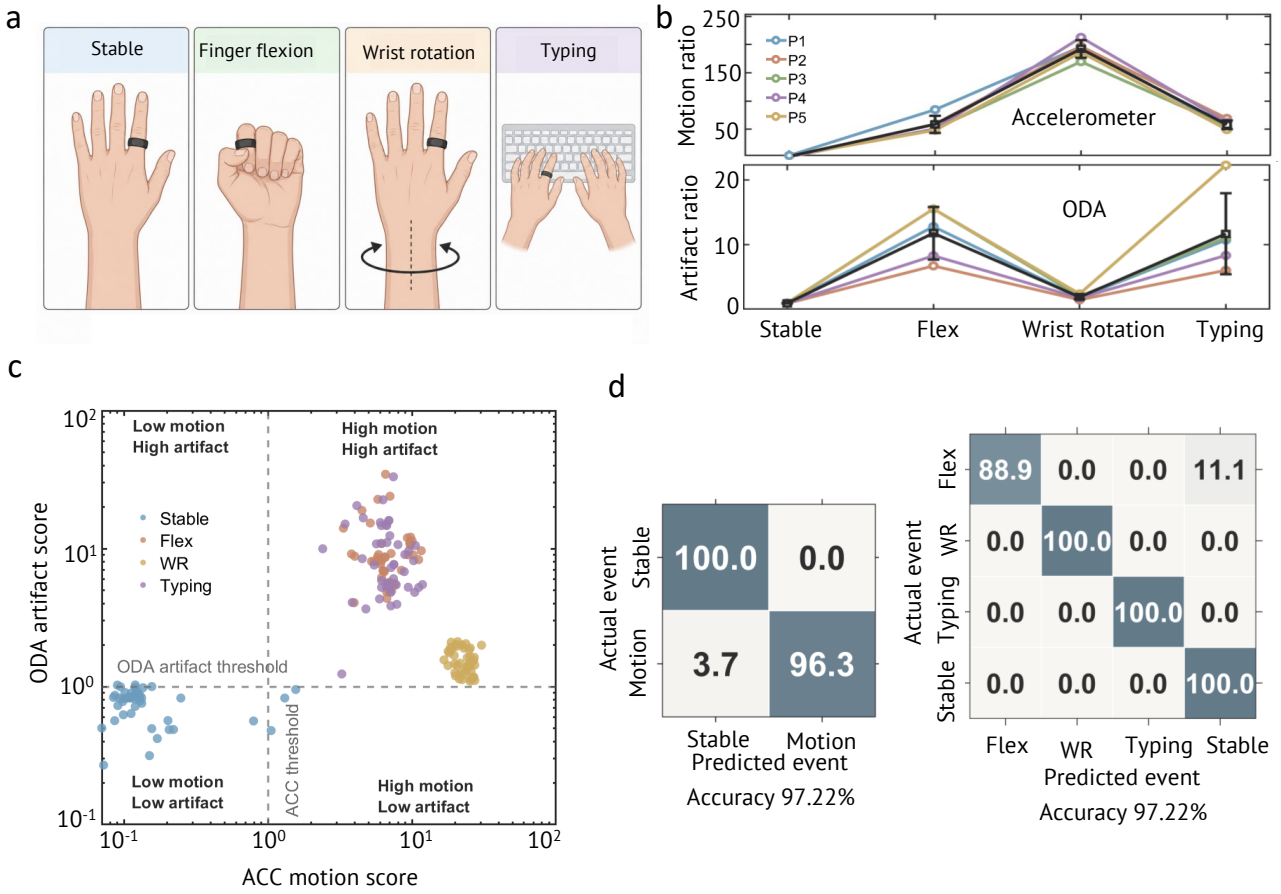


Figure S19. Influence of hand and finger motion on the ODA response. (**a**) Controlled protocol consisting of stable hand positioning, finger flexion, wrist rotation, and keyboard typing. (**b**) Accelerometer motion and ODA artifact ratios for five participants relative to the stable condition. (**c**) Window level relationship between accelerometer motion and ODA artifact scores, with stable-derived thresholds separating low and high-motion and artifact regions. (**d**) Held out participant confusion matrices for binary classification of stable versus motion and four-class classification of stable, finger flexion, wrist rotation, and typing.

The influence of common hand and finger movements on the ODA response was evaluated in five participants. Each participant completed four consecutive 90 s conditions: stable hand positioning, repeated finger flexion, wrist rotation, and keyboard typing, while the ODA and three axis accelerometer signals were recorded simultaneously (Figure S19**a**).

The signals were divided into 10 s windows. Accelerometer activity within each window was quantified using the summed axis wise variability,

$$M_w = \sigma(a_x) + \sigma(a_y) + \sigma(a_z), \tag{34}$$

where $\sigma(a_x)$, $\sigma(a_y)$, and $\sigma(a_z)$ are the standard deviations of the three acceleration axes within window w. ODA disturbance was quantified from the window wise variability of the baseline referenced ODA signal,

$$A_w = \sigma(\mathrm{ODA}_w)\,. \tag{35}$$

For the condition level comparison in Figure S19**b**, the motion and artifact indices were expressed as relative changes from the corresponding participant-specific stable values:

$$R_{\mathrm{motion}} = \frac{M_{\mathrm{task}} - M_{\mathrm{stable}}}{M_{\mathrm{stable}}}, \qquad R_{\mathrm{artifact}} = \frac{A_{\mathrm{task}} - A_{\mathrm{stable}}}{A_{\mathrm{stable}}}. \tag{36}$$

As expected, finger flexion, wrist rotation, and typing produced greater accelerometer activity than the stable condition. Wrist rotation generated the highest overall accelerometer motion, whereas finger flexion and typing produced substantially larger ODA artifacts than wrist rotation. Thus, the movement with the greatest overall acceleration did not necessarily produce the greatest optical disturbance.

This difference reflects the nature of the movement at the ring skin interface. During wrist rotation, the hand, finger, and ring largely move together, producing high accelerometer activity but comparatively limited relative displacement between the ring and skin. In contrast, finger flexion changes finger curvature, contact pressure, and local ring position, producing a stronger disturbance in the reflected optical signal. Typing also introduces repeated local finger movement and participant-dependent ring skin displacement, resulting in appreciable ODA artifacts despite lower overall accelerometer motion than wrist rotation.

To evaluate motion and signal quality at the individual window level, the accelerometer and ODA indices were normalized using thresholds derived from the stable windows:

$$S_{\text{motion}} = \frac{M_w}{\tau_{\text{motion}}}, \qquad S_{\text{artifact}} = \frac{A_w}{\tau_{\text{artifact}}}, \tag{37}$$

where τ_{motion} and τ_{artifact} represent the stable derived motion and ODA artifact thresholds, respectively. A normalized score of 1 therefore represents the corresponding threshold in Figure S19**c**.

The quadrant analysis separates windows into low-motion/low-artifact, high-motion/high-artifact, high-motion/low-artifact, and low-motion/high-artifact regions. Stable windows were concentrated predominantly below both thresholds. Finger-flexion and typing windows were primarily associated with elevated ODA artifacts, whereas wrist-rotation windows exhibited high accelerometer motion but remained largely below the ODA-artifact threshold. These findings demonstrate that motion magnitude alone is insufficient for predicting optical contamination; the movement pattern and the resulting relative displacement at the ring–skin interface are also important.

The accelerometer data were further evaluated for automatic activity recognition using a compact one-dimensional convolutional neural network. The network used two convolutional layers with 16 and 32 filters, followed by global average pooling and a fully connected classification layer. Data from four participants were used for training, while the fifth participant was held out for testing.

As shown in Figure S19**d**, binary classification of stable versus motion windows achieved 97.22% accuracy, with 100% accuracy for stable windows and 96.3% for motion windows. Four-class classification also achieved 97.22% accuracy, with class wise accuracies of 88.9% for finger flexion and 100% for wrist rotation, typing, and stable conditions.

Together, these results establish two complementary approaches for motion aware ODA interpretation. The quadrant analysis provides a threshold based method for identifying windows with elevated motion or ODA variability, while the ML model enables automatic classification of stable and activity specific conditions. Although motion classification was not implemented on device in this study, the demonstrated edge computing capability of the ring provides a clear path toward a hierarchical framework in which the ring first identifies stable windows and performs stress classification only when the stable class is detected. This strategy can further improve the robustness of ODA monitoring during everyday hand activities.

S10.1 Evaluation of ODA During Cognitive Stress

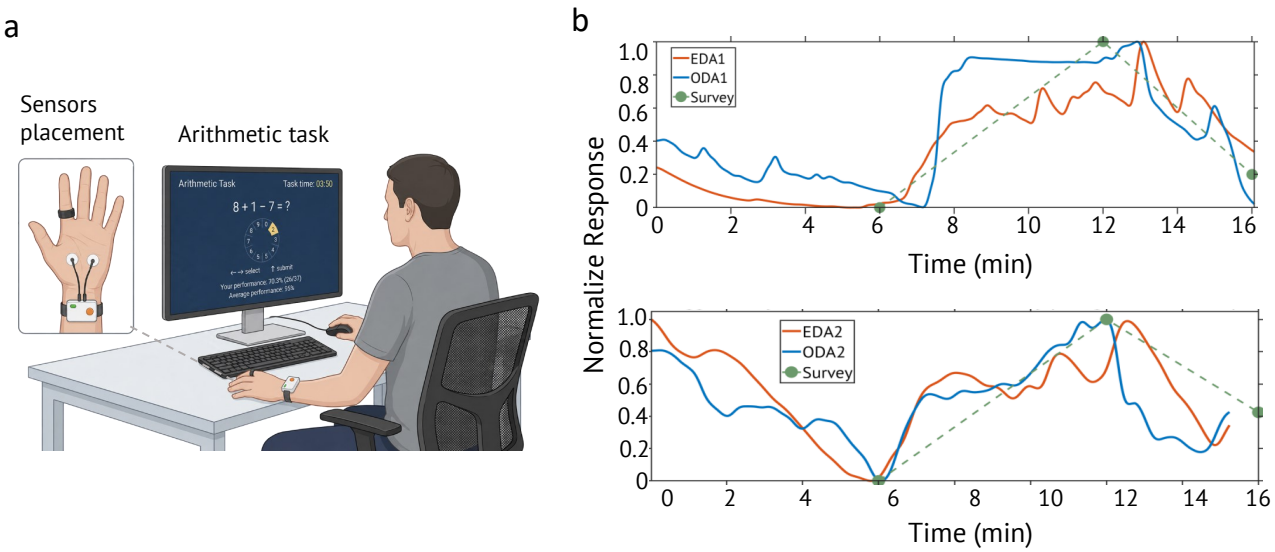


Figure S20. ODA response during a time pressured cognitive arithmetic task. (**a**) Experimental setup for simultaneous ODA and EDA recording during a controlled rest, arithmetic, and recovery protocol. (**b**) Normalized ODA and EDA responses and corresponding self reported stress scores from two participants during the 6 minute resting period, 6 minute arithmetic task, and 4 minute recovery period.

To examine the feasibility of ODA sensing during cognitive stress, the ring was evaluated using a time pressured arithmetic task designed to introduce cognitive load and performance related pressure. Two participants wore the ODA ring together with a commercial EDA sensor while completing a 6 minute resting period, a 6 minute arithmetic task, and a 4 minute recovery period (Figure S20**a**).

At the end of the resting period, participants reported their perceived stress on a scale from 0 to 100, where 0 represented "very definitely not stressed," 50 represented "neutral," and 100 represented "very definitely stressed." The survey was repeated immediately after the arithmetic task and following the recovery period to document changes in perceived stress throughout the protocol.

The arithmetic task was presented as one continuous 6 minute session containing three internally controlled 2 minute stages. Task difficulty progressively increased across the stages, while the permitted response time decreased from 6.0 to 4.5 and 3.0 s per question. The stage transitions were not visible to the participants. To introduce performance pressure, participants were informed that the highest performing participant would receive additional compensation. Their real time performance was displayed together with a simulated average participant score that was intentionally maintained at a comparatively high level.

ODA and EDA signals were recorded continuously throughout the protocol. As shown in Figure S20**b**, both modalities exhibited corresponding temporal changes during the transition from rest to the arithmetic task and the subsequent recovery period. The self reported stress scores also increased following the arithmetic task and decreased during recovery, following the overall physiological response observed in the ODA and EDA signals.

Following signal detrending, normalization, and smoothing, the Pearson correlation coefficients between ODA and EDA were $r = 0.800$ and $r = 0.654$ for participants 1 and 2, respectively. These values indicate moderate to strong temporal agreement between the optical and electrical measurements during the cognitive stress protocol.

Although this preliminary evaluation included only two participants, the observed correspondence between ODA, EDA, and perceived stress demonstrates the potential of the ODA ring to capture dermal responses during cognitive stress in addition to responses induced by the cold pressor test. Future studies with larger participant groups will further evaluate this capability across a broader range of cognitive and psychosocial stressors.

S11 Influence of Surface Sweat Accumulation on the ODA Response

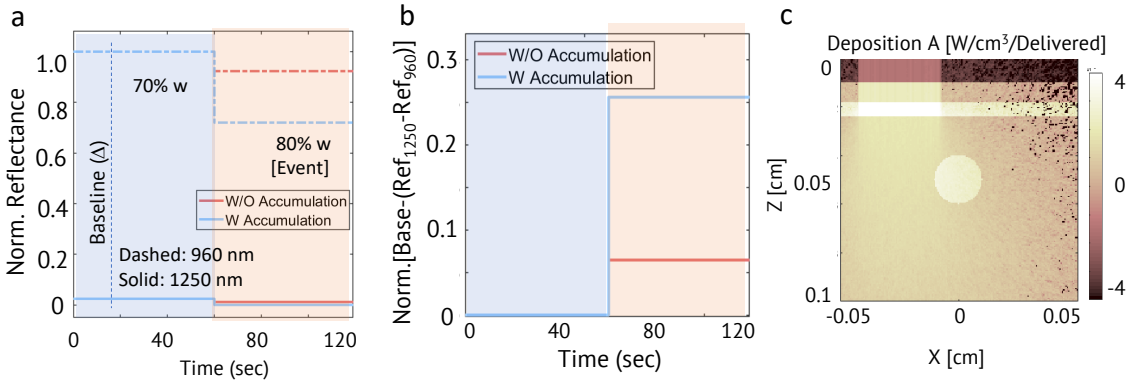


Figure S21. Influence of surface sweat accumulation on the simulated dual-wavelength ODA response. Monte Carlo simulations were performed using the brown skin model with an epidermal thickness of 60 μm and blood oxygen saturation (SpO_2) of 95%. (**a**) Simulated time-dependent reflectance during a baseline–event sequence. Tissue water content was maintained at 70% from 0–60 s and increased to 80% from 60–120 s. In the condition without surface accumulation, no additional liquid layer was introduced. In the surface-accumulation condition, a 150-μm water layer was added above the epidermis during the event period to represent accumulated surface sweat. Dashed and solid lines represent the 960- and 1250-nm reflectance signals, respectively. (**b**) Baseline-corrected ODA response for the conditions without and with surface accumulation, showing amplification of the event-associated response in the presence of the surface water layer. (**c**) Energy-deposition map at 960 nm for the condition with a 150-μm surface water layer, 70% tissue water content, 95% SpO_2, brown skin pigmentation, and an epidermal thickness of 60 μm.

To evaluate the effect of accumulated surface sweat on the ODA measurement, the Monte Carlo tissue model was simulated under two conditions using the brown skin model, an epidermal thickness of 60 μm, and SpO_2 = 95%. In both conditions, tissue water content was maintained at 70% during the initial 60 s baseline period and increased to 80% during the subsequent 60 s event period. In the surface-accumulation condition, a 150 μm water layer was additionally introduced above the epidermis during the event period to represent accumulated sweat on the skin surface.

Figure S21**a** compares the simulated reflectance responses under conditions without and with surface accumulation. In the absence of the additional surface layer, the reflectance change was determined by the modeled increase in tissue water content. When the 150 μm surface water layer was introduced, the 960 nm sensing signal exhibited a larger reflectance change for the same underlying tissue-water condition, whereas the 1250 nm reference signal remained comparatively stable. This amplified wavelength-dependent response indicates that accumulated sweat on the skin surface can alter the ODA signal measured by the ring.

The corresponding baseline-corrected ODA responses are shown in Figure S21**b**. The ODA signal was calculated using the individualized baseline-correction procedure defined in Equations 10–12. The surface water layer produced a substantially larger event-associated ODA response than the condition without accumulation, demonstrating that dynamically accumulated surface sweat can amplify the measured response beyond the contribution arising from subsurface sweat-gland-associated tissue-water changes alone. Because the surface layer was introduced after baseline acquisition, this dynamically developing contribution was not removed by the initial baseline correction.

Figure S21**c** presents the corresponding energy-deposition map at 960 nm for the condition with the 150 μm surface water layer. The additional layer modifies the optical path before the light reaches the epidermis and dermis, thereby influencing the detected reflectance. These simulations identify surface sweat accumulation as a potential confounding factor in optical dermal sensing.

The ODA ring also records complementary physiological signals, including temperature, motion, and PPG derived cardiovascular information such as heart rate, heart-rate variability, pulse amplitude, and pulse-amplitude variability. Surface sweat accumulation and stress-associated dermal activity may produce different combinations and temporal patterns across these sensing modalities. For example, thermoregulatory sweating may be accompanied by changes in skin temperature, physical activity, and cardiovascular dynamics that differ from those associated with an acute stress response. Therefore, integrating the ODA signal with these complementary measurements and analyzing their temporal features using data-driven methods may help distinguish surface-sweat-related optical changes from stress-associated dermal responses.

Nevertheless, multimodal signal interpretation alone may not completely remove the optical interference introduced by a dynamically accumulating liquid layer, and surface sweat accumulation remains a limitation of the present ODA ring design. This interface-related challenge can also affect other skin-contact optical smart-ring platforms that rely on reflected-light measurements. Future ring designs will therefore explore passive wicking materials, microfluidic sweat-transport structures, and other mechanical approaches for removing accumulated liquid from the optical sensing region. Combining improved sweat-management structures with multimodal sensing and data-driven signal analysis may enhance robustness against sweat-accumulation-related interference.

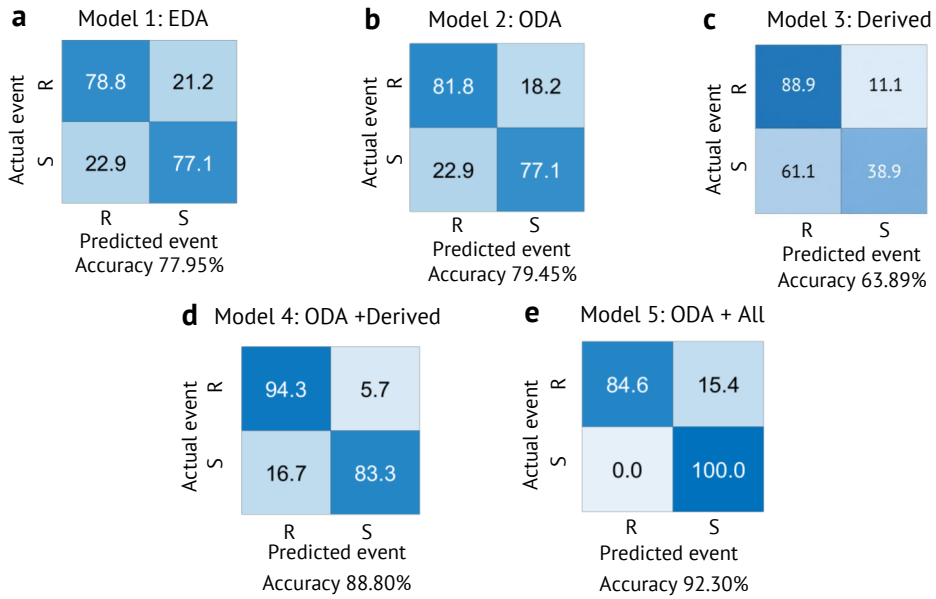


Figure S22. Binary classification performance of the ODA ring sensor on short-period data. Confusion matrices showing classification of stress (S) and relaxation (R): (**a**) Model 1, using EDA only, achieved an accuracy of 77.95%. (**b**) Model 2, using ODA only, achieved an accuracy of 79.45%. (**c**) Model 3, using only the derived physiological features HR, HRV, PA, and PAV, achieved an accuracy of 63.89%. (**d**) Model 4, combining ODA with the derived physiological features, achieved an accuracy of 88.80%. (**e**) Model 5, additionally incorporating temperature and accelerometer data, achieved the highest accuracy of 92.30%.

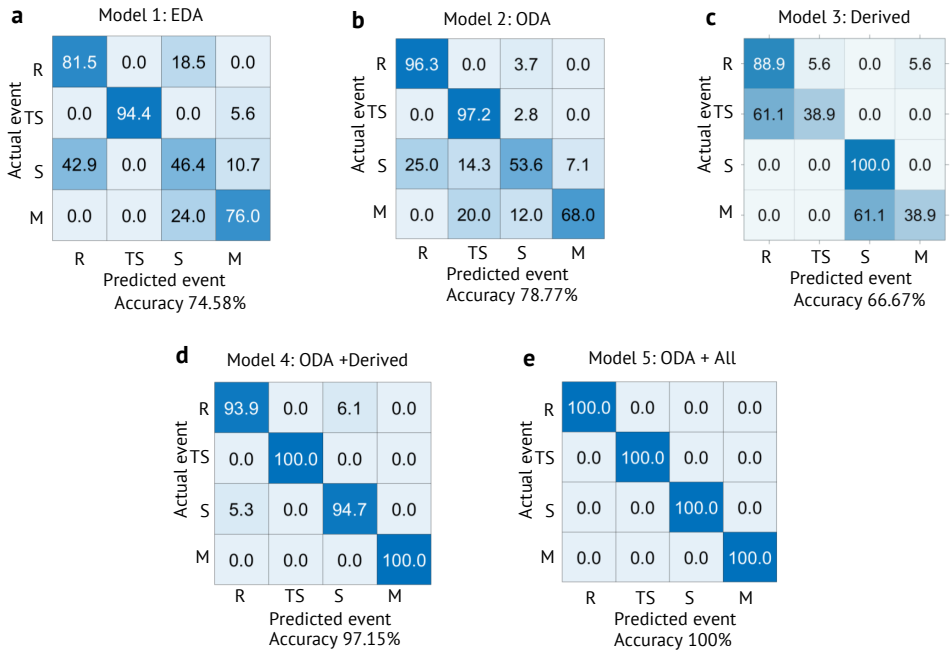


Figure S23. Four-class classification performance of the ODA ring sensor on short-period data. Confusion matrices showing classification of relaxation (R), thermal sweating (TS), stress (S), and motion (M): (**a**) Model 1, using EDA only, achieved an accuracy of 74.58%. (**b**) Model 2, using ODA only, achieved an accuracy of 78.77%. (**c**) Model 3, using only the derived physiological features HR, HRV, PA, and PAV, achieved an accuracy of 66.67%. (**d**) Model 4, combining ODA with the derived physiological features, achieved an accuracy of 97.15%. (**e**) Model 5, additionally incorporating temperature and accelerometer data, achieved 100% classification accuracy.

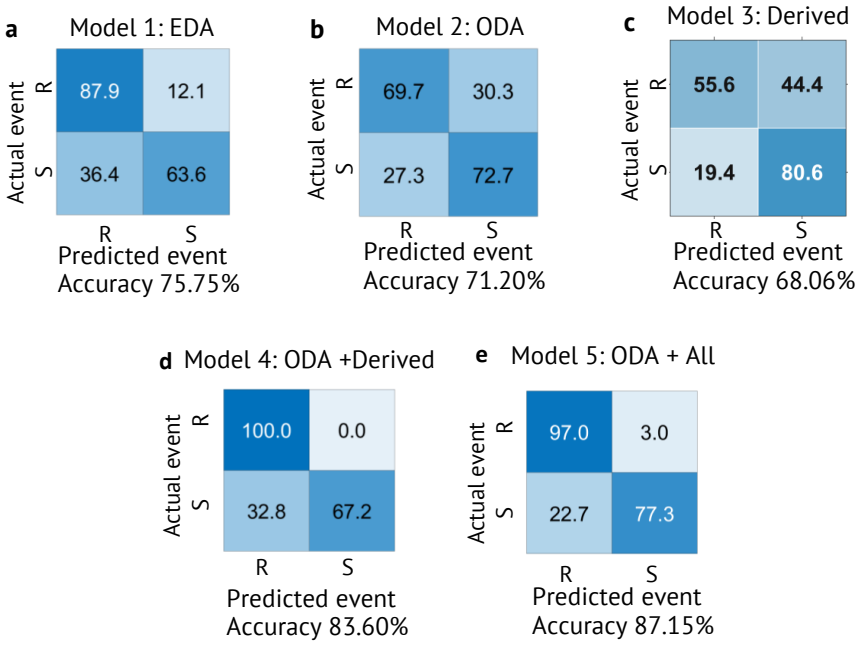


Figure S24. Binary classification performance of the ODA ring sensor on long-period data within 6 hours. Confusion matrices showing classification of stress (S) and relaxation (R): (**a**) Model 1, using EDA only, achieved an accuracy of 75.75%. (**b**) Model 2, using ODA only, achieved an accuracy of 71.20%. (**c**) Model 3, using only the derived physiological features HR, HRV, PA, and PAV, achieved an accuracy of 68.06%. (**d**) Model 4, combining ODA with the derived physiological features, achieved an accuracy of 83.60%. (**e**) Model 5, additionally incorporating temperature and accelerometer data, achieved the highest accuracy of 87.15%.

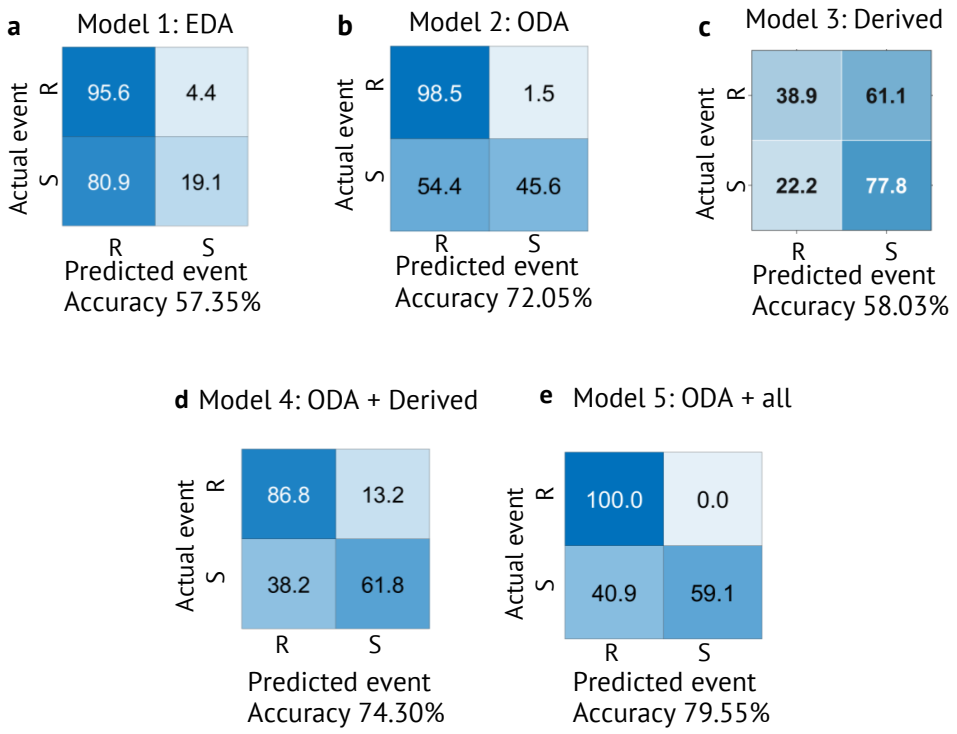


Figure S25. Binary classification performance of the ODA ring sensor on long-period data after 12 hours. Confusion matrices showing classification of stress (S) and relaxation (R): (**a**) Model 1, using EDA only, achieved an accuracy of 57.35%. (**b**) Model 2, using ODA only, achieved an accuracy of 72.05%. (**c**) Model 3, using only the derived physiological features HR, HRV, PA, and PAV, achieved an accuracy of 58.03%. (**d**) Model 4, combining ODA with the derived physiological features, achieved an accuracy of 74.30%. (**e**) Model 5, additionally incorporating temperature and accelerometer data, achieved an accuracy of 79.55%.

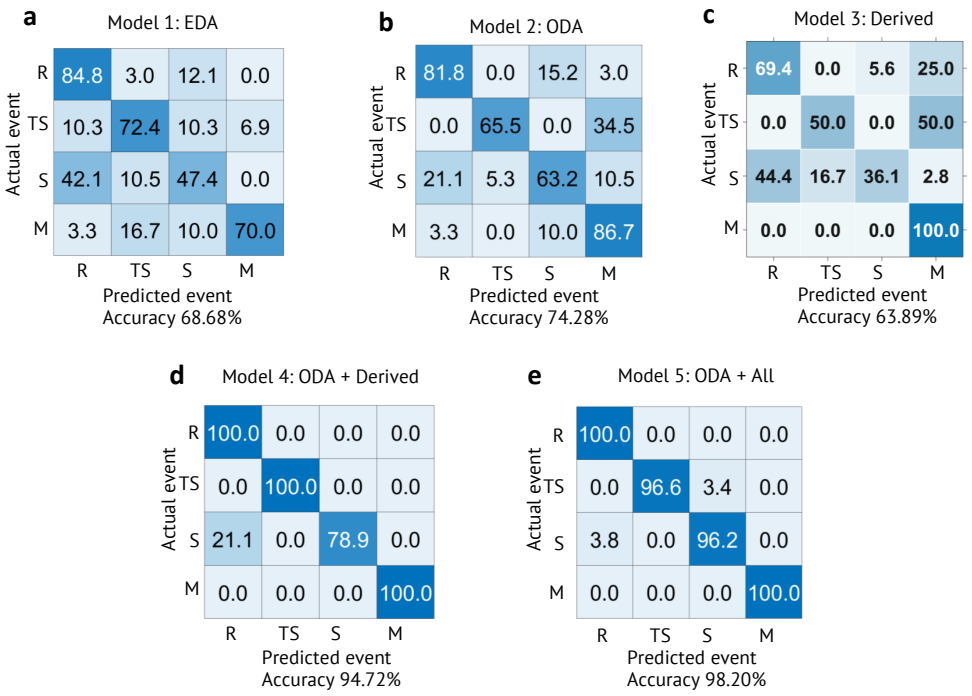


Figure S26. Four-class classification performance of the ODA ring sensor on long-period data within 6 hours. Confusion matrices showing classification of relaxation (R), thermal sweating (TS), stress (S), and motion (M): (**a**) Model 1, using EDA only, achieved an accuracy of 68.68%. (**b**) Model 2, using ODA only, achieved an accuracy of 74.28%. (**c**) Model 3, using only the derived physiological features HR, HRV, PA, and PAV, achieved an accuracy of 63.89%. (**d**) Model 4, combining ODA with the derived physiological features, achieved an accuracy of 94.72%. (**e**) Model 5, additionally incorporating temperature and accelerometer data, achieved the highest accuracy of 98.20%.

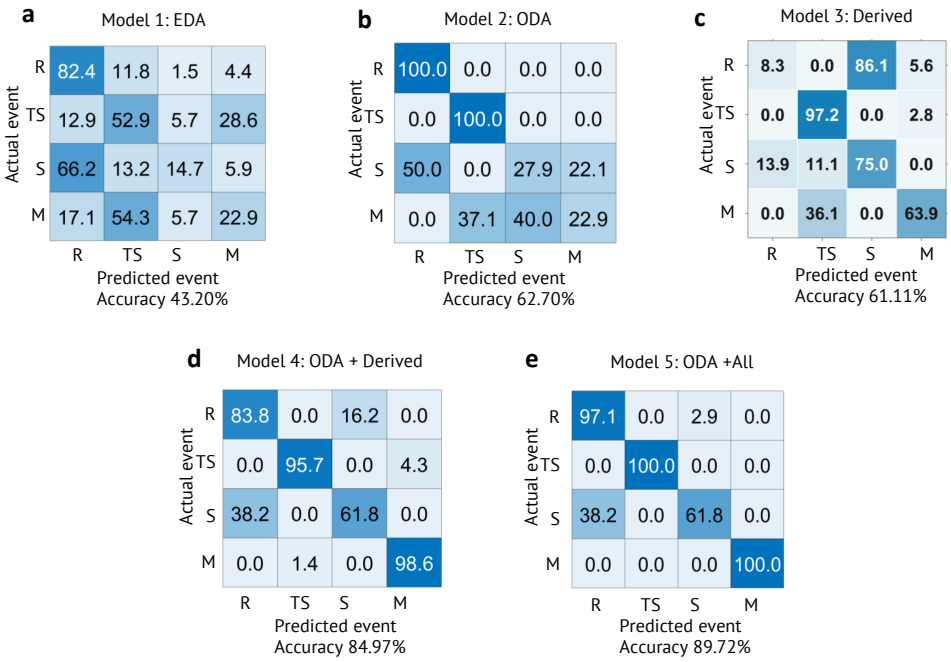


Figure S27. Four-class classification performance of the ODA ring sensor on long-period data after 12 hours. Confusion matrices showing classification of relaxation (R), thermal sweating (TS), stress (S), and motion (M): (**a**) Model 1, using EDA only, achieved an accuracy of 43.20%. (**b**) Model 2, using ODA only, achieved an accuracy of 62.70%. (**c**) Model 3, using only the derived physiological features HR, HRV, PA, and PAV, achieved an accuracy of 61.11%. (**d**) Model 4, combining ODA with the derived physiological features, achieved an accuracy of 84.97%. (**e**) Model 5, additionally incorporating temperature and accelerometer data, achieved the highest accuracy of 89.72%.

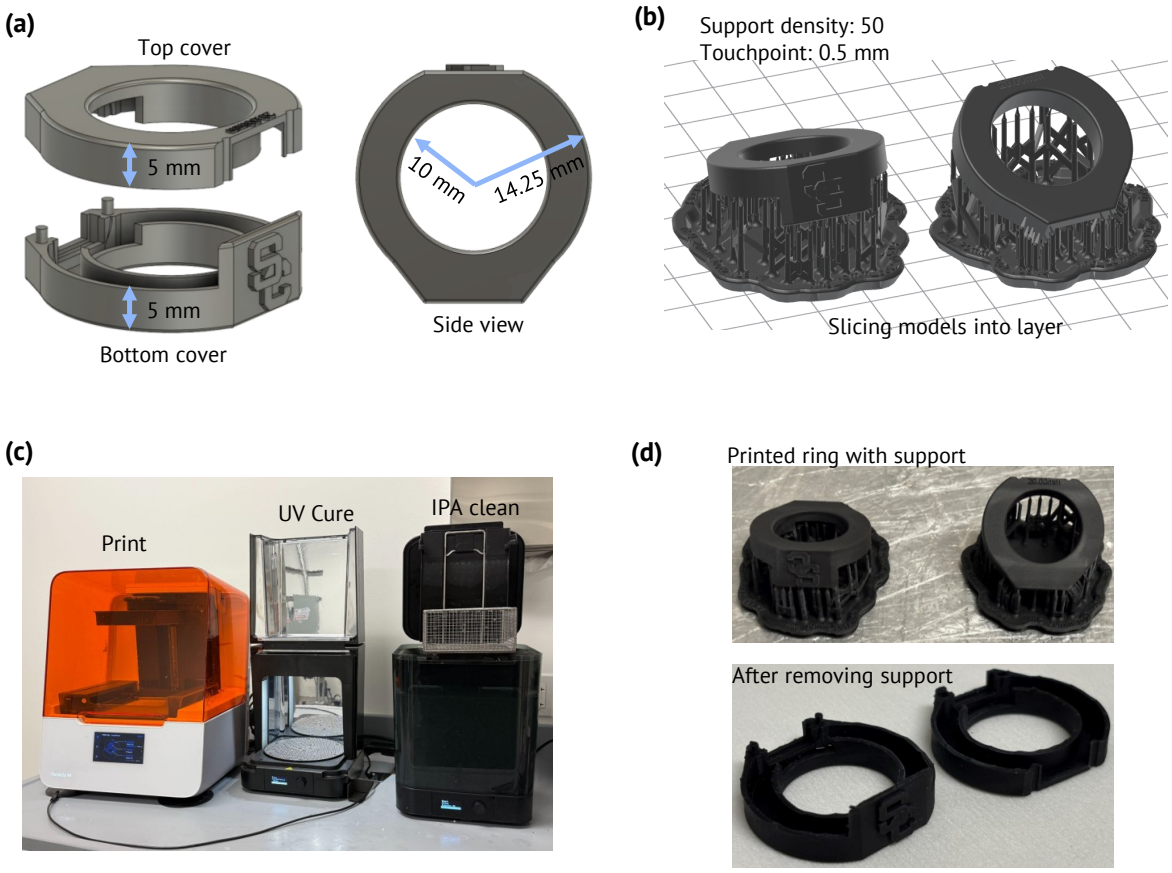


Figure S28. Fabrication process of the ODA ring holder. (a) 3D design created in Fusion 360, highlighting key dimensions: 20 mm inner diameter, 10 mm height, and 28.5 mm outer width. (b) Slicing parameters optimized using Formlabs PreForm software with support density set to 50 and touchpoint size of 0.5 mm for precise printing. (c) Fabrication workflow showcasing printing, washing, and curing processes performed using Formlabs 3D printer and accessories. (d) Final prototypes of the ring holder after removal of support materials, demonstrating successful fabrication and readiness for integration with the ODA sensor system.

Movie S1. Development, integration, and experimental evaluation of the ODA ring.
The movie presents the development workflow of the ODA ring, including flexible PCB design, ring–holder design, firmware development, and system integration of the flexible electronics, ring structure, and switching components. It also shows the experimental setups used to evaluate the integrated ring during relaxation, the cold pressor test (CPT), controlled motion, and thermal sweating conditions.

REFERENCES

1. M. Chesnut, S. Harati, P. Paredes, Y. Khan, A. Foudeh, J. Kim, Z. Bao, L. M. Williams, Stress markers for mental states and biotypes of depression and anxiety: A scoping review and preliminary illustrative analysis. *Chronic Stress* **5**, 24705470211000338 (2021).

2. M. Elgendi, C. Menon, Assessing anxiety disorders using wearable devices: Challenges and future directions. *Brain Sci.* **9**, 50 (2019).

3. C. Xu, Y. Song, J. R. Sempionatto, S. A. Solomon, Y. Yu, H. Y. Y. Nyein, R. Y. Tay, J. Li, W. Heng, J. Min, A. Lao, T. K. Hsiai, J. A. Sumner, W. Gao, A physicochemical-sensing electronic skin for stress response monitoring. *Nat. Electron.* **7**, 168–179 (2024).

4. A. Mishra, M. Agrawal, A. Ali, P. Garg, Uninterrupted real-time cerebral stress level monitoring using wearable biosensors: A review. *Biotechnol. Appl. Biochem.* **70**, 1895–1914 (2023).

5. S. Yoon, J. K. Sim, Y.-H. Cho, A flexible and wearable human stress monitoring patch. *Sci. Rep.* **6**, 23468 (2016).

6. H. D. Critchley, Electrodermal responses: What happens in the brain. *Neuroscientist* **8**, 132–142 (2002).

7. W. Boucsein, *Electrodermal Activity* (Springer, 2012).

8. J. Axelrod, T. D. Reisine, Stress hormones: Their interaction and regulation. *Science* **224**, 452–459 (1984).

9. C. H. Johnson, J. Ivanisevic, G. Siuzdak, Metabolomics: Beyond biomarkers and towards mechanisms. *Nat. Rev. Mol. Cell Biol.* **17**, 451–459 (2016).

10. S. Cohen, T. Kamarck, R. Mermelstein, A global measure of perceived stress. *J. Health Soc. Behav.* **24**, 385–396 (1983).

11. C. D. Spielberger, C. Drew Edwards, R. E. Lushene, J. Montuori, D. Platzek, *STAIC Preliminary Manual for the State-Trait Anxiety Inventory for Children* (Consulting Psychologists Press, 1973).

12. G. J. Fogarty, P. Bramston, R. A. Cummins, Validation of the lifestress inventory for people with a mild intellectual disability. *Res. Dev. Disabil.* **18**, 435–456 (1997).

13. N. K. Singh, S. Chung, A.-Y. Chang, J. Wang, D. A. Hall, A non-invasive wearable stress patch for real-time cortisol monitoring using a pseudoknot-assisted aptamer. *Biosens. Bioelectron.* **227**, 115097 (2023).

14. B. Wang, C. Zhao, Z. Wang, K.-A. Yang, X. Cheng, W. Liu, W. Yu, S. Lin, Y. Zhao, K. M. Cheung, H. Lin, H. Hojaiji, P. S. Weiss, M. N. Stojanović, A. J. Tomiyama, A. M. Andrews, S. Emaminejad, Wearable aptamer-field-effect transistor sensing system for noninvasive cortisol monitoring. *Sci. Adv.* **8**, eabk0967 (2022).

15. S. Sheibani, L. Capua, S. Kamaei, S. S. A. Akbari, J. Zhang, H. Guerin, A. M. Ionescu, Extended gate field-effect-transistor for sensing cortisol stress hormone. *Commun. Mater.* **2**, 10 (2021).

16. A. Nechyporenko, M. Frohme, Y. Strelchuk, V. Omelchenko, V. Gargin, L. Ishchenko, V. Alekseeva, Galvanic skin response and photoplethysmography for stress recognition using machine learning and wearable sensors. *Appl. Sci.* **14**, 11997 (2024).

17. E. T. Attar, V. Balasubramanian, E. Subasi, M. Kaya, Stress analysis based on simultaneous heart rate variability and eeg monitoring. *IEEE J. Transl. Eng. Health Med.* **9**, 1–7 (2021).

18. S. Heo, S. Kwon, J. Lee, Stress detection with single ppg sensor by orchestrating multiple denoising and peak-detecting methods. *IEEE Access* **9**, 47777–47785 (2021).

19. M. Horowitz, N. Wilner, W. Alvarez, Impact of event scale: A measure of subjective stress. *Psychosom. Med.* **41**, 209–218 (1979).

20. S. Xu, J. Kim, J. R. Walter, R. Ghaffari, J. A. Rogers, Translational gaps and opportunities for medical wearables in digital health. *Sci. Transl. Med.* **14**, eabn6036 (2022).

21. S. Pradhan, B. D. Nicholson, S. Albin, R. L. Heise, V. K. Yadavalli, Single-use biomimetic sensors for rapid and sensitive cortisol detection in blood. *Biosens. Bioelectron. X* **12**, 100280 (2022).

22. F. Gao, C. Liu, L. Zhang, T. Liu, Z. Wang, Z. Song, H. Cai, Z. Fang, J. Chen, J. Wang, M. Han, J. Wang, K. Lin, R. Wang, M. Li, Q. Mei, X. Ma, S. Liang, G. Gou, N. Xue, Wearable and flexible electrochemical sensors for sweat analysis: A review. *Microsyst. Nanoeng.* **9**, 1 (2023).

23. Y. Liu, Q. Liu, S. Chen, F. Cheng, H. Wang, W. Peng, Surface plasmon resonance biosensor based on smart phone platforms. *Sci. Rep.* **5**, 12864 (2015).

24. Y. Wang, C. Zhao, J. Wang, X. Luo, L. Xie, S. Zhan, J. Kim, X. Wang, X. Liu, Y. Ying, Wearable plasmonic-metasurface sensor for noninvasive and universal molecular fingerprint detection on biointerfaces. *Sci. Adv.* **7**, eabe4553 (2021).

25. Y. Khan, M. L. Mauriello, P. Nowruzi, A. Motani, G. Hon, N. H. Vitale, J. Li, J. Kim, A. Foudeh, D. Duvio, E. Shols, M. Chesnut, J. A. Landay, J. T. Liphardt, L. M. Williams, K. D. Sudheimer, B. Murmann, Z. Bao, P. E. Paredes, "On stress: Combining human factors and biosignals to inform the placement and design of a skin-like stress sensor," in *Proceedings of the 2024 CHI Conference on Human Factors in Computing Systems* (Association for Computing Machinery, 2024), pp. 1–13.

26. E. Lazarou, T. P. Exarchos, Predicting stress levels using physiological data: Real-time stress prediction models utilizing wearable devices. *AIMS Neurosci.* **11**, 76–102 (2024).

27. X. Peng, D. Li, J. Quan, C. Wu, H. Li, E. Liu, H. Lianting, S. Huang, L. Kong, X. Chen, H. Yang, L. Hu, S. Wang, H. Ma, Q. Geng, A multimodal physiological and psychological dataset for human with mental stress induced myocardial ischemia. *Sci. Data* **11**, 704 (2024).

28. S. Hosseini, R. Gottumukkala, S. Katragadda, R. T. Bhupatiraju, Z. Ashkar, C. W. Borst, K. Cochran, A multimodal sensor dataset for continuous stress detection of nurses in a hospital. *Sci. Data* **9**, 255 (2022).

29. S. A. H. Aqajari, E. K. Naeini, M. A. Mehrabadi, S. Labbaf, A. M. Rahmani, N. Dutt, GSR analysis for stress: Development and validation of an open source tool for noisy naturalistic GSR data. arXiv:2005.01834 [cs.HC] (2020).

30. Y. S. Can, N. Chalabianloo, D. Ekiz, J. Fernandez-Alvarez, G. Riva, C. Ersoy, Personal stress-level clustering and decision-level smoothing to enhance the performance of ambulatory stress detection with smartwatches. *IEEE Access* **8**, 38146–38163 (2020).

31. R. Vahey, R. Becerra, Galvanic skin response in mood disorders: A critical review. *Int. J. Psychol. Psychol. Ther.* **15**, 275–304 (2015).

32. S. Greene, H. Thapliyal, A. Caban-Holt, A survey of affective computing for stress detection: Evaluating technologies in stress detection for better health. *IEEE Consum. Electron. Mag.* **5**, 44–56 (2016).

33. H. J. Han, S. Labbaf, J. L. Borelli, N. Dutt, A. M. Rahmani, Objective stress monitoring based on wearable sensors in everyday settings. *J. Med. Eng. Technol.* **44**, 177–189 (2020).

34. J. A. Miranda Calero, A. Páez-Montoro, C. López-Ongil, S. Paton, Self-adjustable galvanic skin response sensor for physiological monitoring. *IEEE Sensors J.* **23**, 3005–3019 (2023).

35. E. Mejía-Mejía, J. Allen, K. Budidha, C. El-Hajj, P. A. Kyriacou, P. H. Charlton, "Photoplethysmography signal processing and synthesis," in *Photoplethysmography: Technology, Signal Analysis and Applications*, P. A. Kyriacou, J. Allen, Eds. (Elsevier, 2022), chap. 4, pp. 69–146.

36. X. Wang, B. W. Pogue, S. Jiang, H. Dehghani, X. Song, S. Srinivasan, B. A. Brooksby, K. D. Paulsen, C. Kogel, S. P. Poplack, W. A. Wells, Image reconstruction of effective mie scattering parameters of breast tissue in vivo with near-infrared tomography. *J. Biomed. Opt.* **11**, 041106 (2006).

37. S. L. Jacques, Optical properties of biological tissues: A review. *Phys. Med. Biol.* **58**, R37–R61 (2013).

38. H. Suzaki, N. Kobayashi, T. Nagaoka, K. Iwasaki, M. Umezu, S. Takeda, T. Togawa, "Noninvasive measurement of total hemoglobin and hemoglobin derivatives using multiwavelength pulse spectrophotometry—In vitro study with a mock circulatory system," in *2006 International Conference of the IEEE Engineering in Medicine and Biology Society* (IEEE, 2006), pp. 799–802.

39. N. Bosschaart, G. J. Edelman, M. C. G. Aalders, T. G. van Leeuwen, D. J. Faber, A literature review and novel theoretical approach on the optical properties of whole blood. *Lasers Med. Sci.* **29**, 453–479 (2014).

40. Y. Hasanpoor, K. Motaman, B. Tarvirdizadeh, K. Alipour, M. Ghamari, "Stress detection using ppg signal and combined deep CNN-MLP network," in *2022 29th National and 7th International Iranian Conference on Biomedical Engineering (ICBME)* (IEEE, 2022), pp. 223–228.

41. S. L. Jacques, D. J. McAuliffe, The melanosome: Threshold temperature for explosive vaporization and internal absorption coefficient during pulsed laser irradiation. *Photochem. Photobiol.* **53**, 769–775 (1991).

42. G. M. Hale, M. R. Querry, Optical constants of water in the 200-nm to 200-µm wavelength region. *Appl. Optics* **12**, 555–563 (1973).

43. L. G. Henyey, J. L. Greenstein, Diffuse radiation in the galaxy. *Astrophys. J.* **93**, 70–83 (1941).

44. V. G. Kanellis, A review of melanin sensor devices. *Biophys. Rev.* **11**, 843–849 (2019).